Infocommunications Journal

Technically Co-Sponsored by

Selected papers of the CSNDSP 2018 conference – Guest Editorial

Eszter Udvary

The 11th IEEE, IET International Symposium on Communication Systems, Networks, and Digital Signal Processing (CSNDSP) was hosted by The Faculty of Electrical Engineering and Informatics at Budapest University of Technology and Economics, Hungary, 18-20 July 2018. Detailed information can be found on its website (http://csndsp2018.com/).

In CSNDSP 2018 we had four colloquiums on Satellite and Space Communications, Photonic Communications Systems and Networks, Communication Networks Optimization and Optical Wireless Communications as well as some special sessions on the emerging topics organized by the experts working in these research areas to whom CSNDSP is very grateful. During the conference, we had five keynote lectures and 142 technical presentations. The CSNDSP 2018 conference was attended by more than 170 participants from 33 different countries.

From the conference program, six papers were selected for the current special issue of the Infocommunications Journal. All selected papers are related to the physical layer of 5G mobile networks. Two papers present new modulation methods. The third paper introduces an optoelectronic mixer to support photonic-assisted wireless transmission. The next two papers demonstrate the electrical challenges of the system by investigating wideband matching and antenna design. The final paper studies the cost analysis of ultra-reliable low latency 5G communication.

Filter bank multicarrier (FBMC) modulation and spectrally efficient frequency division multiplexing (SEFDM) and are the promising candidate as the physical layer waveform in next-generation broadband networks.

"Practical Evaluations of SEFDM: Timing Offset and Multipath Impairments" presents the non-orthogonal signal waveform SEFDM, which improves spectral efficiency at the cost of self-created inter-carrier interference. The timing offset and the multipath impairments are experimentally demonstrated on the test bed.

„*Overview and Complexity Evaluation of FBMC Transmitter Architectures*" studies the Frequency Spreading (FS) and Poly-Phase Network (PPN) architectures. Based on the complexity calculations, the alternative PPN provides the best results.

"Optoelectronic mixer with a photoconductive switch for 1550 nm wavelengths" experimentally demonstrates an optoelectronic mixer based on an ultrafast photoconductive switch in a heterodyne detection system for RoF transmission. The setup has a relatively flat response curve in a wide frequency range up to 67 GHz. The two presented mixing schemes open the way to the design of new photonic-assisted microwave telecommunications link.

"A Systematic Analysis and Design of a High Gain Microstrip Antenna based on a Single EBG Layer" introduces the design of novel Electromagnetic Band Gap lens based microstrip antenna. The simulation work presents a significant improvement in the antenna parameters.

"Overcoming the Realization Problems of Wideband Matching Circuits" also investigates an important problem of broadband applications. It presents practical design rules for impedance matching. The process can speed up realization issues.

"Reducing operational costs of ultra-reliable low latency services in 5G" focuses on the cost analysis, it examines how the operational expenses dominated by administrative costs can be reduced without impacting the quality of the provided ultra-reliable low latency services in 5G mobile networks.

I hope this careful selection will satisfy our readers' expectations.

Eszter Udvary received Ph.D. degree in electrical engineering from Budapest University of Technology and Economics (BME), Budapest, Hungary, in 2009. She is currently an Associate Professor at BME, Department of Broadband Infocommunications and Electromagnetic Theory, where she leads the Optical and Microwave Telecommunication Lab. Dr. Udvary's research interests are in the broad areas of optical communications, include optical and microwave communication systems, Radio over fibre systems, optical and microwave interactions and applications of special electro-optical devices. She is a member of the Editorial Board of the Infocommunications Journal and a member of HTE and IEEE. She was the chair of the local organizing committee of CSNDSP 2018 conference.

Practical Evaluations of SEFDM: Timing Offset and Multipath Impairments

Tongyang Xu, Hedaia Ghannam and Izzat Darwazeh

Abstract—The non-orthogonal signal waveform spectrally efficient frequency division multiplexing (SEFDM) improves spectral efficiency at the cost of self-created inter carrier interference (ICI). As the orthogonal property, similar to orthogonal frequency division multiplexing (OFDM), no longer exists, the robustness of SEFDM in realistic wireless environments might be weakened. This work aims to evaluate the sensitivity of SEFDM to practical channel distortions using a professional experiment testbed. First, timing offset is studied in a bypass channel to locate the imperfection of the testbed and its impact on SEFDM signals. Then, the joint effect of a multipath frequency selective channel and additive white Gaussian noise (AWGN) is investigated in the testbed. Through practical experiments, we demonstrate the performance of SEFDM in realistic radio frequency (RF) environments and verify two compensation methods for SEFDM. Our results show first frequency-domain compensation works well in frequency non-selective channel conditions while time-domain compensation method is suitable for frequency selective channel conditions. This work paves the way for the application of SEFDM in different channel scenarios.

Index Terms—Multicarrier, software defined radio, channel compensation, spectral efficiency, OFDM, SEFDM, non-orthogonal, timing offset, testbed, experiment.

I. INTRODUCTION

A key direction in future wireless standards is to improve spectral efficiency; a quest that has been at the forefront of designers' minds from the early days of wireless transmission but is acquiring urgency for today's and future systems. A marked contribution of improving spectral efficiency was proposed in 1975 by Mazo [1], where it was proven that, in a single-carrier scenario, a 25% gain in spectral efficiency can be achieved at the same bit error rate (BER) and energy per bit (E_b). In 2003, a multi-carrier system, termed spectrally efficient frequency division multiplexing (SEFDM) [2], [3], which improves spectral efficiency by getting the sub-carriers closer while compromising the orthogonality compared to orthogonal frequency division multiplexing (OFDM) was reported and shown to have advantages in achieving capacity gains [4], [5], choice of signal shapes and power levels [6], [7] and in coexisting with other systems [8]. Other techniques were proposed to improve spectral efficiency by suppressing the out-of-band power level, such as; generalized frequency division multiplexing (GFDM) [9], filterbank based multicarrier (FBMC) [10] and universal-filtered multi-carrier (UFMC) [11].

SEFDM symbols are generated in a similar manner to OFDM with slight modifications of the inverse fast Fourier transform (IFFT) structure [12], yet they require more complex receiver structures [13]. However, with properly designed signal detection and coding schemes [14], [15], SEFDM signal can be recovered with better performance than a typical OFDM signal with the same spectral efficiency (i.e. OFDM might have higher modulation cardinality and/or higher coding rate compared to OFDM). Due to the flexible bandwidth compression benefit of SEFDM, it has been practically used in different areas, such as wireless [16], optical/mm-wave [17], visible light communication (VLC) [18], [19], optical systems [20]–[22] and internet of things (IoT) [23].

In real world wireless communication systems, radio frequency (RF) impairments result in signal loss and further performance degradation. Thus, the optimal performance obtained in an ideal simulation environment would not exist in reaility. RF impairments include nonlinear distortions from high power amplifier (HPA); IQ imbalance; frequency offset; phase noise; timing offset and sampling phase offset. These effects have been studied in detail in [24], [25]. Mitigation of these effects jointly is complex; the compensation for one effect could enhance the impact of others.
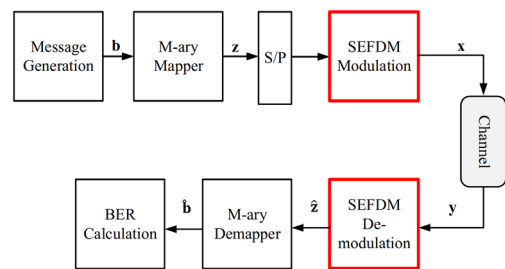
Fig. 1. SEFDM transceiver block diagram.

For OFDM signals, the RF impairments effects can be efficiently ameliorated. Unfortunately, in SEFDM, the self-created inter carrier interference (ICI) challenges the RF effects compensation. Taking into account the equipments used in our experimental testbed, this work investigates the compensation of timing offset and multipath frequency selective impairments in SEFDM.

The rest of the paper is organized as follows: Section II

T. Xu, H. Ghannam and I. Darwazeh are with the Department of Electronic and Electrical Engineering, University College London (UCL), London, WC1E 7JE, UK (e-mail: tongyang.xu.11@ucl.ac.uk, hedaia.ghannam.15@ucl.ac.uk, i.darwazeh@ucl.ac.uk). Corresponding author: Tongyang Xu.
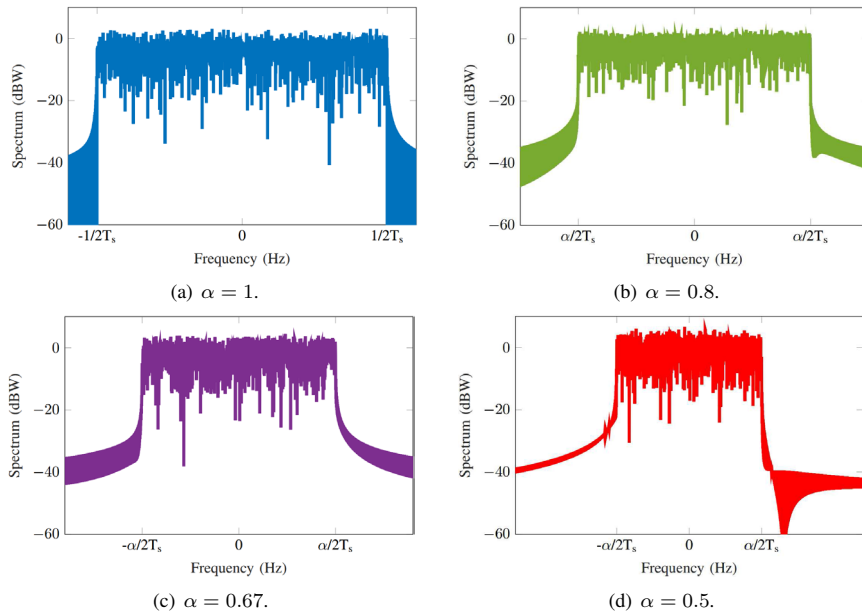
Fig. 2. The frequency spectra of OFDM and SEFDM for $N = 1024$ and different α.

gives an introduction to SEFDM waveform. Section III describes the experimental setup used in the evaluation. Section IV shows the measured results in a bypass channel from the experimental testbed and Section V measures results in a frequency selective channel. Finally, Section VI concludes the paper.

II. SEFDM WAVEFORM

SEFDM is defined as a multi-carrier waveform, where multiple non-orthogonal data streams are transmitted simultaneously, such as each stream only occupies a small part of the available bandwidth. SEFDM offers possibilities of improving spectral efficiency of wired/wireless communication systems by intentionally violating the sub-carrier orthogonality [2].

A general descriptive block diagram of an SEFDM baseband system model is given in Fig. 1. At the transmitter, the message bits **b** are generated and mapped into complex symbols **z**. Then, the mapped symbols are divided into K streams each of size equal to the desired SEFDM symbol size N. The kth stream is converted from a serial stream to a parallel stream using a S/P converter. Afterwards, each element of this stream modulates one sub-carrier of one SEFDM symbol. The modulated signal $x_k(t)$ is sent over a channel, then the received signal $y_k(t)$ is the input to the SEFDM demodulator, which is used to recover the transmitted symbols. Finally, a demapper retrieves the received bits $\hat{\mathbf{b}}$.

Assuming T_s is the symbol interval in a single carrier system, the symbol interval in an SEFDM system of N sub-carriers is $T = N \times T_s$. In SEFDM, the sub-carrier spacing is $\Delta f = \alpha/T$ where $(0 < \alpha \leq 1)$ is the bandwidth compression factor and $\alpha = 1$ is for OFDM. The complex envelope of the

k^{th} baseband SEFDM modulated signal can be presented by

$$x_k(t) = \frac{1}{\sqrt{T}} \sum_{n=0}^{N-1} z_{k,n} \exp\left(j2\pi n\alpha\Delta f g(t - kT)\right). \quad (1)$$

The rectangular pulse in the time-domain is translated into a Sinc-shaped sub-carrier in the frequency-domain, where $\text{Sinc}(x) = \text{Sin}(\pi x)/(\pi x)$. A normalized SEFDM spectrum of $x_k(t)$, for $N = 1024$ sub-carriers and different compression levels is shown in Fig. 2. Clearly, SEFDM in Fig. 2(b-d) saves $(1-\alpha) \times 100\%$ bandwidth in comparison to OFDM in Fig. 2(a) for the same transmission rate, at the expense of orthogonality violation.

SEFDM can be beneficial in another scenario by increasing the overall system throughput while maintaining OFDM bandwidth. The number of SEFDM sub-carriers increases to $\lfloor N/\alpha \rfloor$, where $\lfloor . \rfloor$ denotes the floor operation. Resultantly, the system throughput increases by a factor of $(1-\alpha)/\alpha \times 100\%$.

ICI in SEFDM is evident in Fig. 3. From the figure, the SEFDM signal either occupies 20% less bandwidth for the same number of sub-carriers in OFDM in Fig. 3(a), or has extra two sub-carriers within the same OFDM bandwidth, in Fig. 3(b) and (c), respectively. Another important observation by looking at Fig. 3 is that the dominant interference on a given sub-carrier comes from the main lobes of adjacent sub-carriers. Hence, ICI suppression by pulse shaping is still limited.

If the SEFDM signal in (1) were to be transmitted in additive white Gaussian noise (AWGN) channel $w(t)$, with zero mean and variance $\sigma_n^2 = N_0/2$, where N_0 is the noise power spectral density, the kth SEFDM-received signal is

$$y_k(t) = x_k(t) + w(t). \quad (2)$$

(a) OFDM, $\alpha = 1$ and $N = 8$.

(b) Bandwidth saving scenario, SEFDM $\alpha = 0.8$ and $N = 8$.

(c) Throughput improvement scenario, SEFDM $\alpha = 0.8$ and $N = 10$.
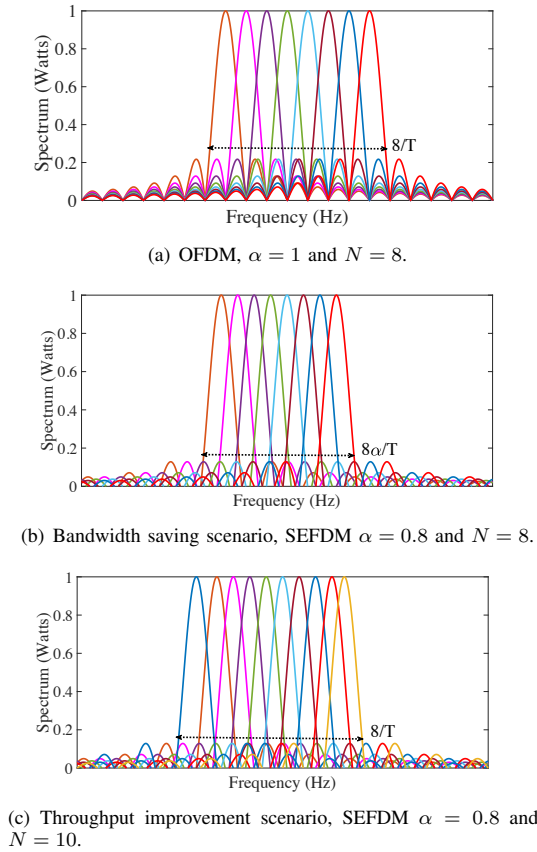
Fig. 3. OFDM and SEFDM Spectra for $\alpha = 0.8, 1$.

At the receiver, a coherent detector with a matched filter is used to demodulate the SEFDM signal, such as

$$\hat{z}_{k,n} = \frac{1}{\sqrt{T}} \int_0^T y_k(t) \exp\left(-j2\pi n\alpha\Delta f g(t - kT)\right) dt, \quad (3)$$

where $\hat{z}_{k,n}$ is the estimated symbol on the nth sub-carrier of the kth SEFDM symbol. The above symbol-by-symbol decision is no longer optimal for SEFDM, due to ICI. Thus, SEFDM detection tends to be complex.

To generate discrete SEFDM symbols, following Nyquist theorem, $Q \geq N$ samples are required to allow the reconstruction of the signal from its samples at the receiver. The sampled version $x_{k,q}$ is

$$x_{k,q} = \frac{1}{\sqrt{Q}} \sum_{n=0}^{N-1} z_{k,n} \exp\left(j2\pi\alpha\frac{qn}{Q}\right), \quad q = 0, 1, ..., Q - 1 \quad (4)$$

where the factor $1/\sqrt{Q}$ in (4) is employed for normalization purposes. Following the same method, the discrete demodulated signal at the receiver side is

$$\hat{z}_{k,n} = \frac{1}{\sqrt{Q}} \sum_{q=0}^{Q-1} y_{k,q} \exp\left(-j2\pi\alpha\frac{qn}{Q}\right), \quad n = 0, 1, ..., N - 1 \quad (5)$$

Taking another look at (4) and (5), they are modified versions of the inverse discrete Fourier transform (IDFT) of

the transmitted symbols **z** and the discrete Fourier transform (DFT) of the received symbols **y**, respectively. In practice, they are implemented in the digital domain by means of inverse fast Fourier transform (IFFT) and fast Fourier transform (FFT), as shown in [12]. For a detailed mathematical treatment of the ICI in SEFDM, readers are referred to [26], [27].

(a) OFDM.

(b) SEFDM ($\alpha = 0.8$).
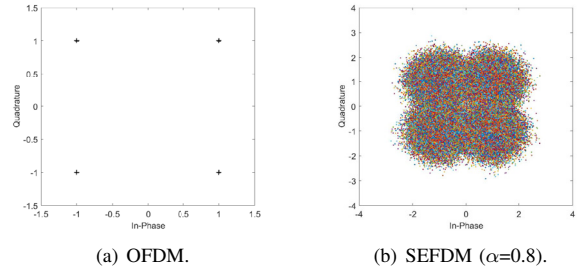
Fig. 4. Constellation patterns for OFDM and SEFDM signals.

Theoretical constellation patterns are studied and compared in Fig. 4 for both OFDM and SEFDM. It is evident that OFDM shows perfect constellation points with no distortion. However, for SEFDM, even without AWGN, the constellation is distorted significantly. The reason for this is the SEFDM self-created ICI.

III. EXPERIMENT TESTBED

Our SEFDM testbed is shown in Fig. 5. The Aeroflex PXI chassis, including a 3026C RF signal generator and a 3035C RF digitizer, plays a key role in connecting the RF environment and the digital signal processors (DSP) environment. The RF signal from the 3026C RF signal generator is transmitted to the input of VR5 channel emulator where its output is connected to the 3035C RF digitizer. The spectrum analyzer, a Tektronix MDO4104-6 Mixed Domain Oscilloscope, is used to evaluate the frequency response of a signal after passing through the VR5 channel emulator.
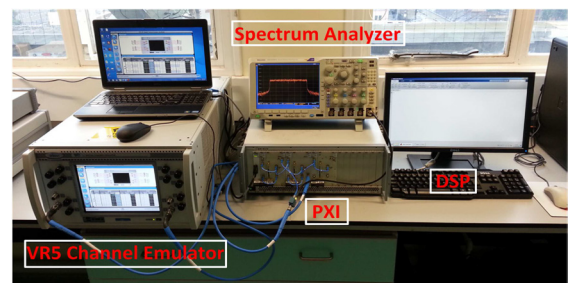
Fig. 5. The SEFDM testbed used for the evaluation.

IV. MEASUREMENT AND DISCUSSIONS IN BYPASS CHANNEL

A bypass channel indicates a channel without AWGN and multipath effects, such that RF effects may be studied more accurately.

(a) Before compensation.

(b) After compensation.

(c) Before compensation on each sub-carrier.

(d) After compensation on each sub-carrier.

Fig. 6. Practical constellation illustrations of OFDM amplitude/phase distortions and their compensation in a bypass channel. Sub-carrier indexes are marked on each constellation sub-diagrams in (c) and (d).

A. OFDM

RF effects are studied initially by examining the OFDM constellation diagrams. Fig. 6 shows OFDM 4QAM constellations before and after RF effects compensation. Fig. 6(a) shows that without applying any compensation algorithms, the resultant constellation looks like a ring. There are multiple reasons accounting for this constellation rotation; the first one is frequency offset, which results from unmatched transmitter/receiver local oscillators. Techniques for frequency offset correction have been elaborately studied in [28]. Other possible impairments are timing offset, phase noise, local oscillator (LO) phase offset and sampling phase errors.

A classic one-tap frequency-domain channel compensation method is employed [29] to correct the constellation rotations. As is shown in Fig. 6(b), the rotations are corrected and four constellation points are clearly illustrated. Thus, it is proven that the testbed has no frequency offset, since frequency offset cannot be straightforwardly compensated by the one-tap frequency-domain method. However, it is difficult to separate timing offset, phase noise, LO phase offset and sampling phase error because they all introduce time independent phase offset.

To have a better understanding of the constellation rotations, a subset of 12 sub-carriers is chosen and the rotations on each may be investigated, as shown in Fig. 6(c). The FFT size in the system is 2048 in which 1200 sub-carriers are used to transmit data, the remaining sub-carriers are reserved for guard bands. In this investigation, 16 non-adjacent sub-carriers are selected with equal sub-carrier index gap, the sub-carrier indices are therefore $N_{index} = 1, 100, 200, ...1100$. Fig. 6(c) clearly shows that the phase offsets of the constellation points are different on each sub-carrier. It seems that the rotation degree is proportional to the sub-carrier index, or in other words the sub-carrier frequency. In addition, the rotation degree of the first sub-carrier is not zero, which indicates a fixed LO phase offset. It should be noted that for each sub-carrier, constellations are time independent, which further confirms that the testbed has no frequency offset. However, sampling phase offset could exist.

To correct for LO phase offset and sampling phase offset in the testbed, accurate symbol stream starting points are obtained by sample shifting of received signals. When four constellation points are clearly and properly obtained, this indicates that there neither LO phase offset nor sampling phase offset are present. If this status can not be achieved, compensation algorithms have to be employed. In the practical testbed, the estimated starting point was found to be slightly earlier than the exact starting point. Therefore, the estimated starting point was shifted to the right, achieving the required compensation. Experimenting with he number of sample shifts and their effects on the constellations is described in the sections below.

1) One Sample Shift Constellation: First, one sample is shifted and the constellation for all sub-carriers and the constellation for a subset of sub-carriers are illustrated in Fig. 7(a) and Fig. 7(d), respectively. We see that the rotation is mitigated slightly, but the constellation of the full signal (all sub-carriers) still resembles circle. This implies that one sample shift is not

Practical Evaluations of SEFDM: Timing Offset and
Multipath Impairments

(a) One sample shift.

(b) Two samples shift.

(c) Three samples shift.

(d) One sample shift on each sub-carrier.

(e) Two samples shift on each sub-carrier.

(f) Three samples shift on each sub-carrier.
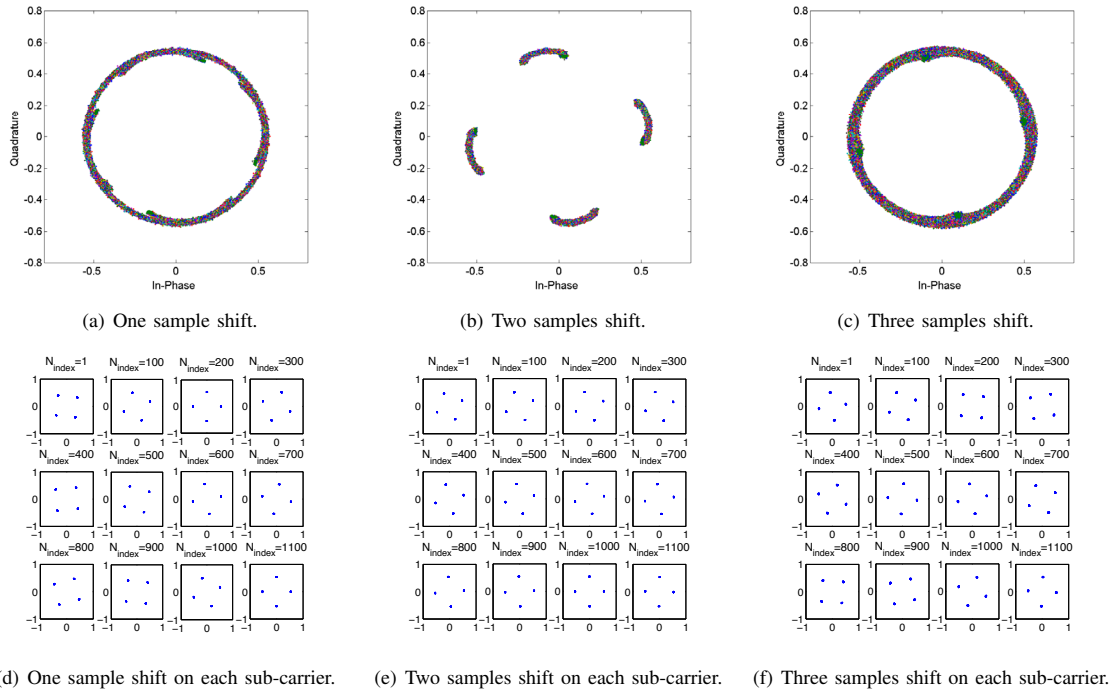
Fig. 7. Constellation illustrations of sample shift for OFDM.

sufficient to remove the effect of timing offset. In addition, it should be noted that the rotation direction in Fig. 7(d) is clockwise due to the fact that the estimated starting point of the data stream is earlier than the exact starting point of the data stream.

2) Two Samples Shift Constellation: In this part, two samples are shifted to get constellation results in Fig. 7. Four points are clearly recognized with small deviations in Fig. 7(b). This indicates that the timing offset is mitigated to some degree. The deviation is caused by a fractional sample shift, in other words, sampling phase offset exists. Furthermore, checking the constellation performance on each sub-carrier, it is apparent that the rotation angle is fixed and rotation degrees for each sub-carrier are almost the same. This fixed rotation is caused by LO phase offset. Therefore, it is inferred that the experimental testbed has no frequency offset (no rotation circle on each sub-carrier); with timing offset (two samples shift or maybe random); with phase offset from local oscillators; with sampling phase offset.

3) Three Samples Shift Constellation: In order to make sure that two samples shift is optimal, Fig. 7 presents three samples shift as well. However, the constellation becomes worse again indicating that an additional timing offset is introduced by shifting three samples. furthermore, constellations of each sub-carrier are investigated showing different rotation degrees for each. It should be noted that the rotation direction in Fig. 7(f) is anti-clockwise, due to the fact that the manually shifted starting point of the data stream is one sample later than the exact starting point of the data stream.

B. SEFDM

SEFDM constellation performance is evaluated in Fig. 8, for a bandwidth compression factor of $\alpha=0.8$. Both constellation results before and after compensation are illustrated. In Fig. 8(a), the scattered constellation points result in a 'ball', which is totally different compared to the constellation ring shown in Fig. 6(a). By using the one-tap frequency-domain compensation method, the rotated constellation points are corrected as shown in Fig. 8(b). It is noted that the recovered constellation is very similar to the theoretical SEFDM constellation pattern in Fig. 4. This indicates that the frequency-domain compensation practically works for timing offset recovery. After compensation, the 4QAM constellation points are not easy to recognize since they are severely affected by ICI. The interference introduced by non-orthogonal packed sub-carriers can be mitigated using the iterative interference cancellation scheme of [14].

V. MEASUREMENT AND DISCUSSIONS IN A FREQUENCY SELECTIVE CHANNEL

In this section, joint effects from both the RF parts and the frequency selective channel are investigated. Thus, the bypass channel is replaced by the frequency selective channel, which is defined in [16]. The frequency selective channel introduces both amplitude and phase distortions. The effects are illustrated in the spectra in Fig. 9. It is clearly illustrated that 20% of bandwidth is saved in SEFDM in Fig. 9(b). The remaining 80% spectrum is distorted in a similar way to that of OFDM in Fig. 9(a). We note that although SEFDM compresses signal bandwidth, the same multipath channel distortions will be applied unaffected.

(a) Before compensation.

(b) After compensation.

(c) Before compensation on each sub-carrier.

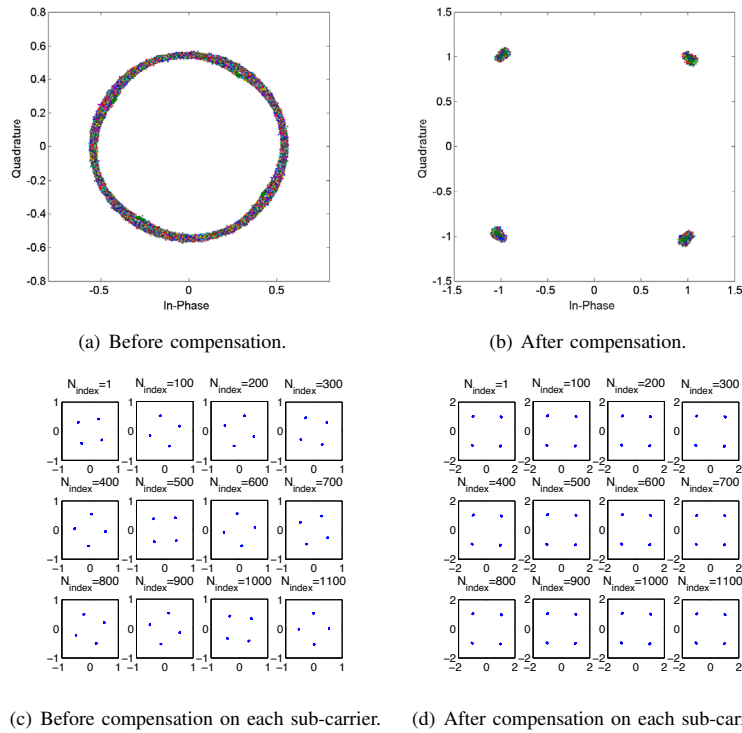(d) After compensation on each sub-carrier.
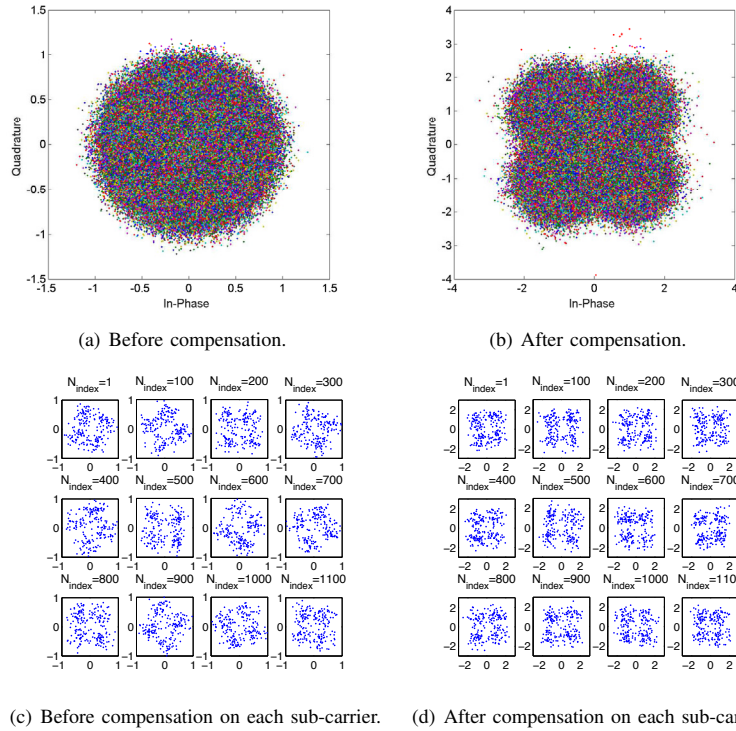
Fig. 8. Practical constellation illustrations of SEFDM (α=0.8) amplitude/phase distortions and their compensation in a bypass channel. Sub-carrier indexes are marked on each constellation sub-diagram in (c) and (d).

(a) OFDM.
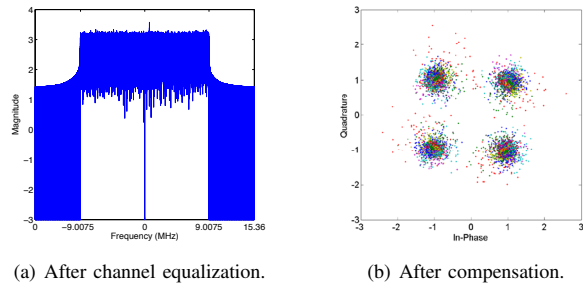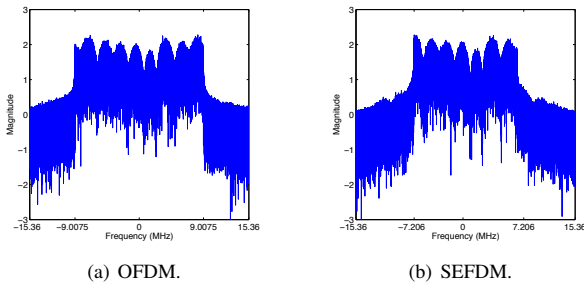
(b) SEFDM.

Fig. 9. Spectrum of 4QAM OFDM and 4QAM SEFDM ($\alpha = 0.8$) in the condition of the frequency selective channel and AWGN at SNR=36 dB.

(a) After channel equalization.

(b) After compensation.

Fig. 10. Spectrum and constellation of 4QAM OFDM after channel equalization in the condition of the frequency selective channel and AWGN at SNR=36 dB.

A. OFDM Frequency-Domain Compensation

After the typical one-tap frequency-domain channel equalization, the frequency selective distortion is compensated and the spectrum flatness is recovered. Signals can be recovered with clear constellation points shown in Fig. 10. It should be noted that the frequency-domain and time-domain [30] channel equalization schemes results in the same performance of OFDM. It is known that in typical OFDM systems, sub-carriers are orthogonally packed with no interference. However, this is not the case in SEFDM since sub-carriers are non-orthogonally packed. In the following sections, both frequency-domain and time-domain equalizers for SEFDM are evaluated and compared.

B. SEFDM Frequency-Domain Compensation

In Fig. 11(a), frequency-domain channel equalization aims to compensate the amplitude distorted spectrum in Fig. 9(b). However, this frequency-domain technique doesn't work properly since the equalized spectrum is not amplitude flat. This is because the one-tap equalizer only makes use of fractional channel information to compensate for channel distortions without considering the sub-carriers overlapping. The effects of the frequency-domain channel equalization can also be observed in Fig. 11(b) where the recovered constellations are no longer in four distinguishable regions but rather appear as a 'mixed ball'.

It is inferred that for small level of interference such as
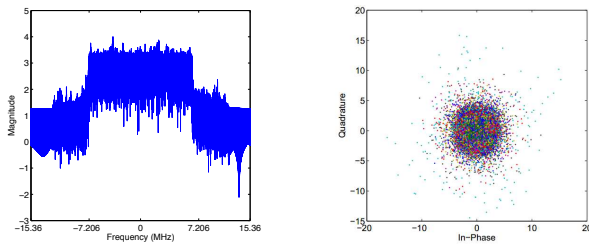
(a) Spectrum after channel equaliza-
tion.

(b) Constellation after channel
equalization.

Fig. 11. Spectrum and constellation of 4QAM SEFDM ($\alpha = 0.8$) after frequency-domain channel equalization in the condition of the frequency selective channel and AWGN at SNR=36 dB.

timing offset, one-tap frequency-domain channel compensation method works well. However, due to the amplitude and phase variations introduced by multipath channel, the one-tap equalizer cannot efficiently mitigate the channel effect.

C. SEFDM Time-Domain Compensation

Based on the previous results and analysis, the multi-tap equalizer is considered to be an adequate solution to deal with channel distortions in SEFDM. The work in [30] proposed a time-domain channel compensation method, which can efficiently recover SEFDM signals in distortion-prone environment. Fig. 12 presents results after the time-domain equalization. The equalized spectrum is amplitude flat and the recovered constellation points are distinguishable.
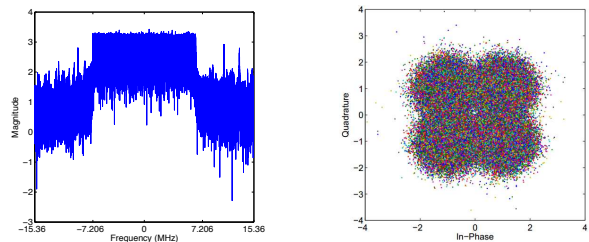
(a) Spectrum after channel equaliza-
tion.

(b) Constellation after channel
equalization.

Fig. 12. Spectrum and constellation of 4QAM SEFDM ($\alpha = 0.8$) after time-domain channel equalization in the condition of the frequency selective channel and AWGN at SNR=36 dB.

However, even with proper channel compensation, constellation points are still scattered due to the waveform ICI. This scattering can only be mitigated by using specially designed signal detection algorithms such as those in [14], [15].

VI. CONCLUSIONS

Practical evaluations of RF impairments on SEFDM signals are demonstrated in the reported experimental testbed. Timing offset is first evaluated with practical results illustrated. Constellation results show that timing offset and additional phase mismatch would have limited effect on SEFDM performance, although self-created ICI is introduced. Then, a

multipath channel is included jointly with the timing offset. Constellation results show that the frequency selective channel has significant negative impact on system performance. It is concluded that the joint effects greatly affect the system performance and their effect is higher than those of timing offset alone. In addition, this work verifies that the typical one-tap frequency-domain channel compensation method works well for SEFDM signals with timing offset and other phase mismatch scenarios. However, with the introduction of frequency selective channels, its performance greatly drops resulting in difficult signal recovery. In this case either time-domain channel compensation or specially designed solutions have to be considered, perhaps at the expense of system complexity.

REFERENCES

[1] J. Mazo, "Faster-than-Nyquist signaling," *Bell Syst. Tech. J*, vol. 54, no. 8, pp. 1451–1462, 1975.

[2] M. Rodrigues and I. Darwazeh, "A spectrally efficient frequency division multiplexing based communications system," in *Proc. 8th Int. OFDM Workshop*, Hamburg, 2003, pp. 48–49.

[3] I. Darwazeh, H. Ghannam, and T. Xu, "The first 15 years of SEFDM: a brief survey," in *2018 11th International Symposium on Communication Systems, Networks & Digital Signal Processing (CSNDSP18)*, Budapest, Hungary, Jul. 2018.

[4] J. Zhou, Y. Qiao, Z. Yang, Q. Cheng, Q. Wang, M. Guo, and X. Tang, "Capacity limit for faster-than-Nyquist non-orthogonal frequency-division multiplexing signaling," *Scientific Reports*, vol. 7, 2017.

[5] D. Rainnie, Y. Feng, and J. Bajcsy, "On capacity merits of spectrally efficient FDM," in *Military Communications Conference, MILCOM 2015 - 2015 IEEE*, Oct 2015, pp. 581–586.

[6] D. K. Fadeev and A. V. Rashich, "Optimal input power backoff of a nonlinear power amplifier for SEFDM system," in *Internet of Things, Smart Spaces, and Next Generation Networks and Systems - 15th International Conference, NEW2AN 2015, and 8th Conference, ruSMART 2015, St. Petersburg, Russia, August 26-28, 2015, Proceedings*, 2015, pp. 669–678.

[7] S. V. Zavjalov, D. K. Fadeev, and S. V. Volvenko, "Influence of input power backoff of nonlinear power amplifier on BER performance of optimal SEFDM signals," in *2016 8th International Congress on Ultra Modern Telecommunications and Control Systems and Workshops (ICUMT)*, Oct 2016, pp. 447–450.

[8] T. Xu and I. Darwazeh, "Experiment for Non-Interfering coexistence of Non-Orthogonal SEFDM signals and LTE," in *2018 11th International Symposium on Communication Systems, Networks & Digital Signal Processing (CSNDSP) (CSNDSP18)*, Budapest, Hungary, Jul. 2018.

[9] N. Michailow, M. Matthe, I. Gaspar, A. Caldevilla, L. Mendes, A. Festag, and G. Fettweis, "Generalized frequency division multiplexing for 5th generation cellular networks," *IEEE Transactions on Communications*, vol. 62, no. 9, pp. 3045–3061, Sept 2014.

[10] B. Farhang-Boroujeny, "OFDM versus filter bank multicarrier," *IEEE Signal Processing Magazine*, vol. 28, no. 3, pp. 92–112, May 2011.

[11] V. Vakilian, T. Wild, F. Schaich, S. Ten Brink, and J.-F. Frigon, "Universal-filtered multi-carrier technique for wireless systems beyond LTE," in *Globecom Workshops (GC Wkshps), 2013 IEEE*, Dec 2013, pp. 223–228.

[12] P. N. Whatmough, M. R. Perrett, S. Isam, and I. Darwazeh, "VLSI architecture for a reconfigurable spectrally efficient FDM baseband transmitter," *IEEE Transactions on Circuits and Systems I: Regular Papers*, vol. 59, no. 5, pp. 1107–1118, May 2012.

[13] I. Kanaras, A. Chorti, M. Rodrigues, and I. Darwazeh, "Spectrally efficient FDM signals: bandwidth gain at the expense of receiver complexity," in *Communications, 2009. ICC '09. IEEE International Conference on*, June 2009, pp. 1–6.

[14] T. Xu and I. Darwazeh, "A soft detector for spectrally efficient systems with non-orthogonal overlapped sub-carriers," *IEEE Communications Letters*, vol. 18, no. 10, pp. 1847–1850, Oct 2014.

[15] H. Ghannam and I. Darwazeh, "SEFDM over satellite systems with advanced interference cancellation," *IET Communications*, vol. 12, no. 1, pp. 59–66, 2018.

[16] T. Xu and I. Darwazeh, "Transmission experiment of bandwidth compressed carrier aggregation in a realistic fading channel," *IEEE Transactions on Vehicular Technology*, vol. 66, no. 5, pp. 4087–4097, May 2017.

[17] T. Xu, S. Mikroulis, J. E. Mitchell, and I. Darwazeh, "Bandwidth compressed waveform for 60-GHz millimeter-wave radio over fiber experiment," *Journal of Lightwave Technology*, vol. 34, no. 14, pp. 3458–3465, July 2016.

[18] Y. Wang, Y. Zhou, T. Gui, K. Zhong, X. Zhou, L. Wang, A. P. T. Lau, C. Lu, and N. Chi, "SEFDM based spectrum compressed VLC system using RLS time-domain channel estimation and ID-FSD hybrid decoder," in *ECOC 2016; 42nd European Conference on Optical Communication*, Sept 2016, pp. 1–3.

[19] ——, "Efficient MMSE-SQRD-based MIMO decoder for SEFDM-based 2.4-Gb/s-spectrum-compressed WDM VLC system," *IEEE Photonics Journal*, vol. 8, no. 4, pp. 1–9, Aug 2016.

[20] I. Darwazeh, T. Xu, T. Gui, Y. Bao, and Z. Li, "Optical SEFDM system; bandwidth saving using non-orthogonal sub-carriers," *IEEE Photonics Technology Letters*, vol. 26, no. 4, pp. 352–355, Feb 2014.

[21] J. Huang, Q. Sui, Z. Li, and F. Ji, "Experimental demonstration of 16-QAM DD-SEFDM with cascaded BPSK iterative detection," *IEEE Photonics Journal*, vol. 8, no. 3, pp. 1–9, June 2016.

[22] D. Nopchinda, T. Xu, R. Maher, B. Thomsen, and I. Darwazeh, "Dual polarization coherent optical spectrally efficient frequency division multiplexing," *Photonics Technology Letters, IEEE*, vol. 28, no. 1, pp. 83–86, Jan 2016.

[23] T. Xu and I. Darwazeh, "Non-orthogonal narrowband Internet of Things: A design for saving bandwidth and doubling the number of connected devices," *IEEE Internet of Things Journal*, vol. 5, no. 3, pp. 2120–2129, June 2018.

[24] G. Fettweis, M. Lohning, D. Petrovic, M. Windisch, P. Zillmann, and W. Rave, "Dirty RF: a new paradigm," in *Personal, Indoor and Mobile Radio Communications, 2005. PIMRC 2005. IEEE 16th International Symposium on*, vol. 4, Sept 2005, pp. 2347–2355 Vol. 4.

[25] T. Schenk, P. Smulders, and E. Fledderus, "Multiple carriers in wireless communications - curse or blessing?" in *NERG: Tijdschrift Ned. Elektron & Radiogenoot*, 2005, pp. 112–123.

[26] S. Isam and I. Darwazeh, "Characterizing the intercarrier interference of non-orthogonal spectrally efficient FDM system," in *Communication Systems, Networks Digital Signal Processing (CSNDSP), 2012 8th International Symposium on*, July 2012, pp. 1–5.

[27] H. Ghannam and I. Darwazeh, "SEFDM: Spectral efficiency upper bound and interference distribution," in *2018 11th International Symposium on Communication Systems, Networks & Digital Signal Processing (CSNDSP) (CSNDSP18)*, Budapest, Hungary, Jul. 2018.

[28] Y. S. Cho, J. Kim, W. Y. Yang, and C.-G. Kang, *MIMO-OFDM Wireless Communications with MATLAB*. John Wiley & Sons (Asia) Pte Ltd, 2010.

[29] T. Hwang, C. Yang, G. Wu, S. Li, and G. Y. Li, "OFDM and its wireless applications: A survey," *IEEE Transactions on Vehicular Technology*, vol. 58, no. 4, pp. 1673–1694, May 2009.

[30] S. Isam and I. Darwazeh, "Robust channel estimation for spectrally efficient FDM system," in *Telecommunications (ICT), 2012 19th International Conference on*, April 2012, pp. 1–6.
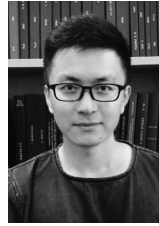
Tongyang Xu (M'17) received the B.Eng. degree in Electronic Information Engineering from Xidian University, Xi'an, China, in 2011 and the M.Sc. degree (Distinction) in Telecommunications and the Ph.D. degree (Best PhD thesis Lombardi prize runner up) in Electronic and Electrical Engineering from University College London (UCL), London, U.K., in 2012 and 2017, respectively.

His research interests include 5G/B5G communications, waveform design, Internet of Things, software defined radio, real-time testbed prototyping, machine learning, neural networks design and data analysis. He has authored and co-authored more than 30 papers in the areas of wireless and optical communications. He contributed two books entitled Signal Processing for 5G: Algorithms and Implementations (Wiley, 2016) and Key Enabling Technolo- gies for 5G Mobile Communications (Springer, 2016).

Dr. Xu was a recipient of the UCL Faculty of Engineering Sciences Scholarship in 2013. He was the nominated investigator of the two successful "Impact Acceleration Discovery to Use" Awards at UCL in 2016 and 2018 and was the co-recipient of Smart Agriculture Entrepreneurship Grant at Rothamsted Research in 2017. He received the Chinese Government Award for Outstanding Self-Financed Students Abroad in 2017, the Lombardi Prize runner up for the best PhD thesis in 2018 and the National Instruments Academic Research Grant Award in 2018.

Hedaia Ghannam (S'14) is currently working toward her Ph.D. degree in the communication and information system research group, electronic and electrical engineering department at UCL. She obtained her MSc. in telecommunication and information systems from University of Essex in 2014. Her research interests are in the physical layer of future communication systems, such as the 5th generation cellular network, where she looks at the system from different aspects including spectrally efficient modulation formats, channel coding and the design of practical channel estimators and detectors for the aforementioned systems.

Izzat Darwazeh (SM'03) holds the University of London Chair of Communications Engineering and leads the 70-strong Communications and Information Systems Group of the Department of Elec- tronic and Electrical Engineering, University College London (UCL). He is also the Director of ICCS; UCL Institute of Communications and Connected Systems. Professor Darwazeh is a graduate of the University of Jordan (Electrical Engineering-1984) and has obtained an MSc (1986) and a PhD (1991) degrees from the University of Manchester in the UK.

He has authored/coauthored more than 250 papers and book chapters in the areas of optical and wireless communications and monolithic microwave integrated circuits (MMICs) and high-speed/frequency circuits. He coedited Analogue Optical Fibre Communications (IEE, 1995) and was a co-editor of the 2008 Elsevier-Newness book on Electrical Engineering. He is also the co- author of two books; the 2005 book on Linear Circuit Analysis and Modelling (Elsevier) and of the 2015 book on Microwave Active Circuit Analysis and Design (Academic Press). He currently teaches mobile and wireless communications and circuit design and his current research activities are in ultra high-speed microwave circuits and in wireless and optical communication systems. In 2002 he proposed (with Miguel Rodrigues) the Fast OFDM concept and in 2003 the SEFDM concept and has been working on these topics since. Professor Darwazeh is a Chartered Engineer, Fellow of the IET and a Fellow of the Institute of Telecommunications Professionals FITP.

Overview and Complexity Evaluation of FBMC Transmitter Architectures

Husam Al-amaireh and Zsolt Kollár

Abstract—**Computational complexity is one of the key factors considered for evaluating transmitter performance of future 5G applications. In this contribution we have chosen Filter Bank MultiCarrier (FBMC) as it is the most possible candidate to replace/coexist with the Orthogonal Frequency Division Multiplexing (OFDM) modulation. In the literature two main design approaches can be found for FBMC: Frequency Spreading (FS) and PolyPhase Network (PPN). From these two structures numerous schemes were derived. These schemes are studied and the complexity (real multiplications and additions) for each scheme is compared. Based on the complexity calculations, the simulation results show that PPN has a better complexity performance compared with FS. Also, the alternative PPN schemes have significant improvement in complexity compared to the standard PPN.**

Index Terms—**FBMC, complexity, polyphase, frequency spreading .**

I. INTRODUCTION

Orthogonal Frequency Division Multiplexing (OFDM) is considered as one of the most prevailing technologies that dominate the broadband wireless digital communication so far. The fundamental principle of OFDM is based on dividing the spectrum into orthogonal sub-bands in an efficient manner while keeping the transmitter and receiver design simple. Despite several advantages, OFDM suffers from many shortcomings that render it unsatisfactory for the 5th Generation (5G) requirements. Also it is expected that 5G will heavily implement Machine-Type Communications (MTC) which is further classified (according to FP7 project METIS) into two classes; massive (mMTC) and ultra-reliable (uMTC). While the first class suggests that tens of billions of low complexity machine-type devices will be implemented, the second puts emphasis on the availability, latency and reliability [1]. In order to satisfy the future requirements, several contenders for the physical layer modulation are competing to prove the best promising performance for the next generation of communication interfaces. These candidates are Filter Bank MultiCarrier (FBMC), Universal Filtered MultiCarrier (UFMC), Generalized Frequency Division Multiplexing (GFDM) and OFDM [2]. The process for deciding which is the best candidate is non trivial, many key features have to be considered and each feature has to be taken into account with different weighting factors which help in the overall evaluation and decision. Some of these features are peak-to-average power ratio, power spectral density, spectral efficiency, multiple access interference and also the design complexity of the transceiver chain.

In this paper the FBMC modulation is investigated, as it is considered the most favored candidate for 5G physical layer. This technique is also known as Offset Quadrature Amplitude (OQAM) OFDM or Staggered MultiTone (SMT) modulation. This paper focuses mainly on the computational complexity of the various FBMC transmitter implementations. In general, the structure of the transmitter is composed of several blocks where each block performs certain signal processing tasks with different complexity; for example the encoder block which encodes input information bits, the encoded bits are divided into groups of size $\log_2 S_i$ and mapped into symbols from S_iQAM, where S_i is the number of QAM constellations, and then the data are modulated by the multicarrier modulator. For the purpose of the comparisons among different implementations, the common parts are not included in complexity calculations where only the multicarrier part is considered, it is also assumed that all input subcarriers are utilized, i.e no guard bands are used at the sides. The complexity requirement of OFDM is also included in the comparison as a reference so that the additional requirements of the FBMC implementations can be better evaluated. Furthermore, the computations are performed in terms of the required real valued multiplications and additions.

Two different design structures for FBMC transmitters can be found in the literature, the first one is the FS which is based on applying the sub band filtering in frequency domain with increased size of Inverse Fast Fourier Transform (IFFT) as shown in [3], and the second type is where PPN is applied in conjunction with an IFFT of a regular symbols size [4]. Several design structures were proposed to reduce complexity, in [5] and [6], a complexity reduction of almost half size is achieved with the aid of some additional signal processing steps. Another alternative structure was introduced in [7] where similarly, a complexity reduction of almost half size can be achieved by the modifications to the butterflies structure of the applied IFFT.

The paper is organized as follows. Section II presents the baseband FBMC signal model. In Section III the investigated FBMC transmitter schemes [3]–[7] are briefly presented and their complexity requirements are derived. Section IV presents results of the complexity comparison between the introduced transmitter schemes. Finally, Section V draws the conclusion.

Husam Al-amaireh and Zsolt Kollár are with Department of Broadband Infocommunications and Electromagnetic Theory, Budapest University of Technology and Economics, Budapest, Hungary
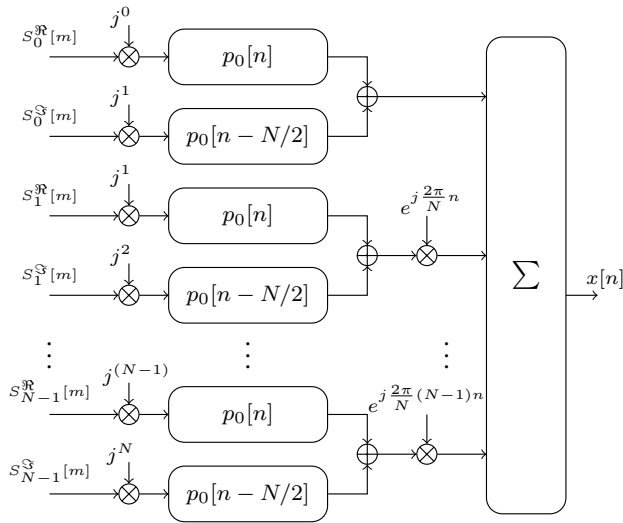{al-amaireh, kollar}@hvt.bme.hu

Fig. 1. FBMC signal model using direct implementation

II. FBMC SIGNAL MODEL

In this section we briefly introduce the baseband signal model for the FBMC modulation.

First, the binary data is modulated using QAM. The complex symbols generated by the QAM mapper are divided into consecutive symbols with length of N. The mth symbol is split into a real part $s^{\Re}[m]$ and an imaginary part $s^{\Im}[m]$. The real and imaginary parts are multiplied by the phase rotation factor j^k and j^{k+1}, respectively, where k corresponds to the kth subcarrier. Then, the two signals are filtered by a prototype filter p_0 with a length of $L = KN$ – where K is an integer number – and summed. The real and imaginary parts of the QAM symbols are transmitted with an $N/2$ delay. The filtered real and imaginary signals are summed and modulated with the corresponding k^{th} complex subcarrier with the frequency of $e^{j\frac{2\pi}{N}k}$. Finally, the N paralell streams are added to form the discrete basedband FBMC signal $x[n]$, which can be also mathematically expressed as

$$x[n] = \sum_{m=-\infty}^{\infty} \sum_{k=0}^{N-1} \left(j^k s_k^{\Re}[m] p_0[n - mN] + \right.$$
$$\left. j^{k+1} s_k^{\Im}[m] p_0 \left[n - mN - \frac{N}{2} \right] \right) e^{j\frac{2\pi}{N}kn}, \quad (1)$$

where $j = \sqrt{-1}$. The corresponding FBMC transmitter model is shown in Fig. 1.

III. COMPLEXITY ANALYIS OF FBMC TRANSMITTER SCHEMES

In this section the complexity requirements are detailed for various FBMC transmitter structures, also for the purpose of complexity calculations we have classified the structures into two main categories: standard structures, and improved PPN structures. Furthermore, as all of the discussed FBMC implementations include the IFFT, a brief description for its complexity is given prior to the discussion.
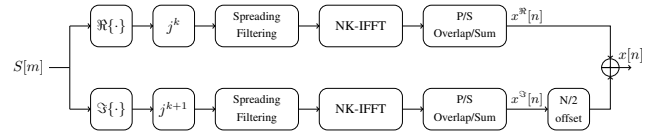
Fig. 2. FS implementation

A. IFFT complexity

During the calculations, split-radix implementation of the IFFT is considered as it significantly improves the number of operations compared to other solutions [8]. Another important factor which plays a major rule in complexity calculations is the multiplication of two complex numbers. A complex multiplication can be achieved through 3 real multiplications and 3 real additions or 4 real multiplications and 2 real additions. As multiplication is more costly than additions in hardware implementations the 3 real additions and 3 real multiplications will be considered thourghout this paper. As a result the complexity requirement for the IFFT of an input size N can be given as:

$$\mathcal{M}_{\text{IFFT}} = N(\log_2 N - 3) + 4, \quad (2)$$
$$\mathcal{A}_{\text{IFFT}} = 3N(\log_2 N - 1) + 4, \quad (3)$$

where $\mathcal{M}, \mathcal{A}$ are the number of real multiplications and additions, respectively.

B. Standard Structures

First, the straightforward implementations of the FBMC signal model are discussed which are commonly presented in the literature.

1) Direct implementation: The complexity of the direct implementation – presented in Fig. 1 – is based on two parallel filtering operations (requiring $2NK$ real multiplications and $2(NK-1)$ real additions per subcarrier), the modulation with complex subcarrier frequencies (requiring 3 real multiplications and 3 real additions per subcarrier) and finally summing the N complex streams (requiring $N-1$ real additions). The multiplication with the phase rotation factor and the addition of the two filter outputs are considered negligible. As a result, the required complexity calculations for the direct implementation can be expressed in the function of N and K as

$$\mathcal{M}_{\text{direct}} = 2N^2K + 3N, \quad (4)$$
$$\mathcal{A}_{\text{direct}} = 2N(NK-1) + 3N + N - 1. \quad (5)$$

2) Frequency spreading: The block diagram of the FBMC transmitter based on FS [3] can be seen in Fig. 2. As a first step, the real and imaginary symbols are extracted and the phase rotation factor is applied. Then, each signal is multiplied by $2K-1$ frequency domain coefficients P_k of the prototype filter p_0, were the multiplication with coefficient $P_{k=0}=1$ can be excluded. As a result, the total number of operations before applying NK-IFFT stage is the following:

$$\mathcal{M}_{\text{spreading}} = N(2K-2), \quad (6)$$

Overview and Complexity Evaluation of FBMC
Transmitter Architectures

Fig. 3. Polyphase implementation with Standard PPN using 2 IFFTs

Fig. 4. Polyphase implementation with Reduced PPN I using 1 IFFT

Fig. 5. Polyphase implementation with Reduced PPN II using 2 pruned IFFTs

As neighboring subchannels are either purely real or purely imagainary, no additions are required.

As the FBMC symbols are constructed in the frequency domain, an IFFT with size NK is required. As a result the calculations requirements can be calculated according to Eq. (2) and Eq. (3) for an NK-IFFT.

As a last step, the overlappig of the time domain FBMC symbols require only NK complex additions resulting in a complexity requirement of

$$\mathcal{A}_{\text{overlap}} = 2NK. \qquad (7)$$
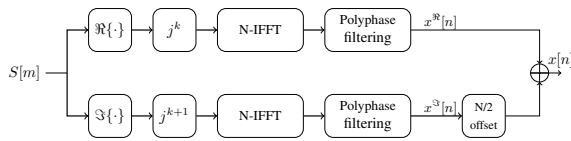
Finally, the resulting calculation complexity of the FS implementation for the two branches – considering the final adder, which can be realized by 2 real valued additions – can be expressed as:

$$\mathcal{M}_{\text{FS}} = 2\left(2N(K-1)+(NK(\log_2 NK-3)+4)\right), \qquad (8)$$

$$\mathcal{A}_{\text{FS}} = 2\left((3NK(\log_2 NK-1)+4)+2NK\right)+2. \qquad (9)$$

3) Standard PPN implementation: Another approach is presented in [4] where the frequency domain filtering is moved from the frequency domain to time domain using PPN decomposition of the prototype filter. This way the FBMC signal generation can be achieved by an N-IFFT and a PPN. The block diagram of the proposed FBMC transmitter can be seen in Fig. 3.

As mentioned in the previous section the multiplication with the phase rotation factor is negligible. The size of the IFFT will be equal to N, the cost of applying IFFT on purely real or purely imaginary inputs will be the same as complex input signals [9], so the number of multiplications and additions can be expressed as in Eq. (2) and Eq. (3), respectively. Furthermore, due to the PPN implementation the N samples of the time domain signal will be filtered by K coefficients where the cost of filtering operations can be expressed as

$$\mathcal{M}_{\text{filt}} = 2NK, \qquad (10)$$

$$\mathcal{A}_{\text{filt}} = 2N(K-1). \qquad (11)$$

As a result, the total complexity requirement for the real and imaginary paths – and taking the final adder into consideration – can be derived as

$$\mathcal{M}_{\text{PPN}} = 2(N(\log_2 N-3)+4+2NK), \qquad (12)$$

$$\mathcal{A}_{\text{PPN}} = 2(3N(\log_2 N-1)+4+2N(K-1))+2. \qquad (13)$$

C. Improved PPN Structures

In this section methods for improving the computational complexity of the Standard PPN structure are discussed.
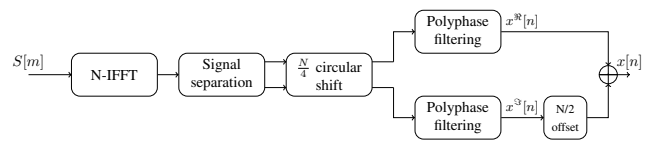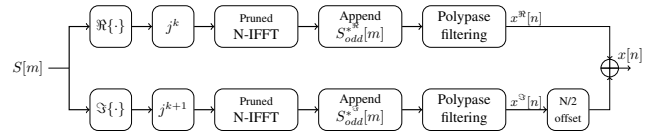
1) Reduced PPN I.: The implementation cost of the standard PPN solution can be further reduced. In [5], the two purely real input symbols are combined together as single complex input symbols which reduces the number of required IFFTs by half and some additional signal processing. For signals separation after the IFFT, as shown in [6], [10], there are no extra multiplications needed except a multiplication with 1/2 which can be achieved by simple binary bit shift. On the other hand, extra additions are required for the separation of the real and imaginary signal parts:

$$\mathcal{A}_{\text{sepration}} = 4N. \qquad (14)$$

As a result the complexity requirement for the reduced PPN solution – with the final adder – can be calculated as:

$$\mathcal{M}_{\text{reduced,I}} = N(\log_2 N-3)+4+4NK, \qquad (15)$$

$$\mathcal{A}_{\text{reduced,I}} = 3N(\log_2 N-1)+4+4N(K-1)+4N+2. \qquad (16)$$

2) Reduced PPN II.: Another solution for complexity reduction of standard PPN implementation was proposed in [7]. The solution takes advantage of the complex conjugate symmetry between odd and even indices of the IFFT. Concerning the computational complexity, it has reduced the cost by only calculating the even indices and design a pruned IFFT structure which cancels the unneeded calculations of the IFFT butterflies, then the samples of the odd indices will be calculated from the results of the even indices. The design structure shown in Fig. 5 is similar to standard PPN solution with a difference of implementing a pruned IFFT instead of using a standard IFFT. As a result the total complexity requirement can be expressed using Eq. (12) and Eq. (13) by substituting the calculation requirements of an IFFT with the requirements of a pruned IFFT as

$$\mathcal{M}_{\text{reduced,II}} = 2\left(\frac{N}{2}\left(\log_2\frac{N}{2}-3\right)+4+2NK\right), \qquad (17)$$

$$\mathcal{A}_{\text{reduced,II}} = 2\left(3\frac{N}{2}\left(\log_2\frac{N}{2}-1\right)+4+2N(K-1)\right)+2. \qquad (18)$$

3) Reduced PPN III.: The third introduced solution for reducing complexity can be considered as a hybrid solution,
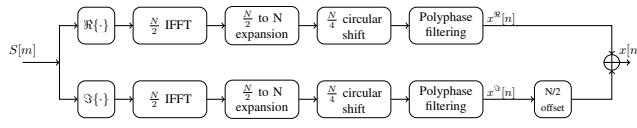
Fig. 6. Polyphase implementation with Reduced PPN III using two half size IFFTs

which means that it combines some properties of both Standard PPN and Reduced PPN I at the same time. In [6] the solution suggests that each of the two real input streams (real part and imaginary part) is processed separately (just as standard solution), however, each symbol of size N of each stream is split into two $N/2$ size symbols, the two halves are combined as one $N/2$ complex symbol and an IFFT of size $N/2$ will be applied, then at the output of IFFT - after some signal processing - each symbol will be spread again into N size as shown in Fig. 6. The total complexity can be considered as a standard PPN with $N/2$-IFFT in additon to some signal processing to spread the symbols. The complexity for signal separation as in [6], [10], can be calculated as the following,

$$\mathcal{M}_{\text{separation}} = 2(2N+1), \tag{19}$$

$$\mathcal{A}_{\text{separation}} = 2(7N-1), \tag{20}$$

So the total complexity of Reduced PPN III becomes:

$$\mathcal{M}_{\text{reduced,III}} = 2\left(\frac{N}{2}\left(\log_2 \frac{N}{2} - 3\right) + 5 + 2NK + 2N\right), \tag{21}$$

$$\mathcal{A}_{\text{reduced,III}} = 2\left(3\frac{N}{2}\left(\log_2 \frac{N}{2} - 1\right) + 3 + \\ + 2N(K-1) + 7N\right) + 2. \tag{22}$$

IV. COMPARISON OF THE FBMC TRANSMITTER STRUCTURES

In the previous section, a brief descriptions of the various FBMC transmitter structures and their complexity in terms of additions and multiplications were derived. In this section these methods are compared in terms of complexity requirements and further their advantages and implementation aspects, the complexity requirement of OFDM – using a single N-IFFT – is added to all figures as a reference in order to show the added complexity requirements of the different FBMC transmitter structures. A summary of the complexity requirement can be seen in Table I in function of N and K. For comparison, the presented equation are evaluated for $K = 4$, which is a commonly used value in practical FBMC implementations.

1) Complexity requirements for standard structures: The required number of real additions and multiplications for different methods of the standard FBMC transmitter can be observed in Fig. 7 and Fig. 8 respectively, as functions of the number of subcarriers N. It can be seen that the direct implementation is extremely inefficient. The FS implementation can significantly reduce the complexity requirements. Further reduction can be achieved using the Standard PPN solutions.
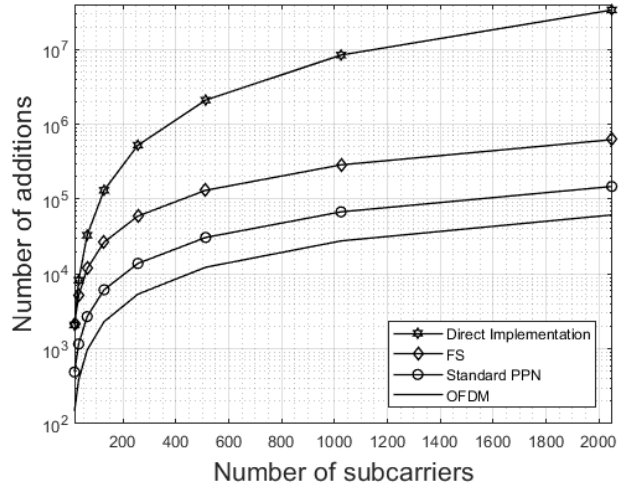
Fig. 7. Number of additions for the standard FBMC transmitters as a function of the number of subcarriers N
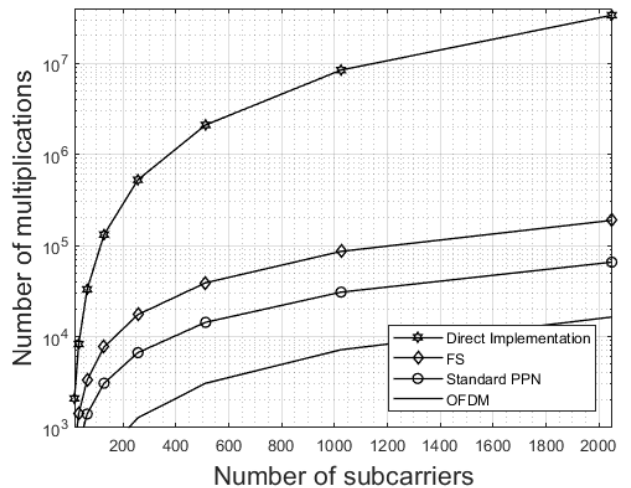
Fig. 8. Number of multiplications for the standard FBMC transmitters as a function of the number of subcarriers N

2) Complexity requirements for improved PPN structures: Fig. 9 and Fig. 10 show the required number of real additions and multiplications respectively for improved PPN methods of FBMC transmitter as function of the number of subcarriers N. Based on the results shown in the figures it can be stated that the three introduced methods for reducing complexity have a relatively similar complexity. The Reduced PPN II has the lowest complexity requirements. The Reduced PPN I performs slightly worse. The Reduced PPN III has the worst performance among the presented methods. It can also be stated that the complexity requirement for all Reduced PPN methods is almost half of the Standard PPN implementation, however the complexity requirement of OFDM is significantly lower compared with all FBMC structures.

TABLE I
COMPARISON OF THE NUMBER OF OPERATIONS FOR THE VARIOUS FBMC TRANSMITTERS SCHEMES

Method	Number of Multiplication	Number of Additions
Direct Implementation	$2N^2K + 3N$	$2N(NK-1) + 3N + N - 1$
FS	$2\left(2N(K-1) + (NK(\log_2 NK - 3) + 4)\right)$	$2\left((3NK(\log_2 NK - 1) + 4) + 2NK\right) + 2$
Standard PPN	$2(N(\log_2 N - 3) + 4 + 2NK)$	$2(3N(\log_2 N - 1) + 4 + 2N(K-1)) + 2$
Reduced PPN I	$N(\log_2 N - 3) + 4 + 4NK$	$3N(\log_2 N - 1) + 4 + 4N(K-1) + 4N + 2$
Reduced PPN II	$2(N/2(\log_2 N/2 - 3) + 4 + 2NK)$	$2(3N/2(\log_2 N/2 - 1) + 4 + 2N(K-1)) + 2$
Reduced PPN III	$2(N/2(\log_2 N/2 - 3) + 5 + 2N + 2NK)$	$2(3N/2(\log_2 N/2 - 1) + 3 + 7N + 2N(K-1)) + 2$
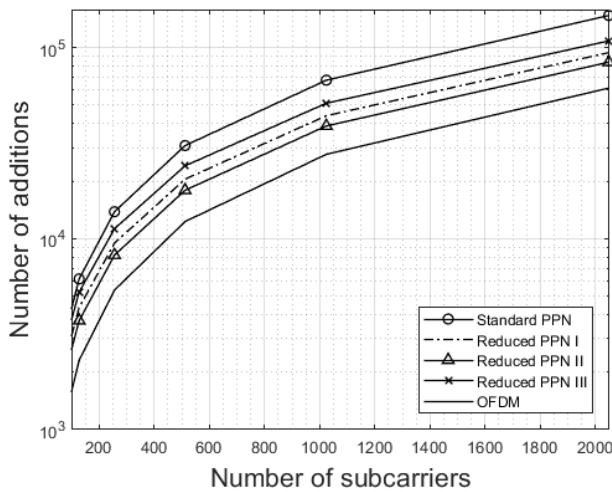
Fig. 9. Number of additions for the improved FBMC transmitters as a function of the number of subcarriers N

3) Design aspects: In this section a brief discussion of the further advantages of each FBMC design structure is presented. The direct implementation is extremely inefficient to be implemented, it can be viewed as the "ancestor" which led to the derivation of other structures. When comparing FS and PPN, although the PPN structure has a smaller complexity, for the receiver implementation subchannel equalization is carried out in time domain which introduces additional memory and delay [3], on the other hand the channel equalization in FS structure is much simpler.

When comparing the three improved PPN methods, Reduced PPN II provides best performance in terms of complexity. On the other hand, the Reduced PPN I – as it uses a single IFFT – can be a flexible solution if an existing OFDM transmitter has to be extended/reconfigured for FMBC transmission [5]. Furthermore, the Reduced PPN III is beneficial in hardware implementations with reduced arithmetic precision, due to the fact that it has the lowest quantization error, as shown in [6].

V. CONCLUSION

FBMC is considered as one of the most favored candidates for future 5G physical layer modulation. There are different design approaches for FBMC where each structure has different complexity requirements. In this paper a brief description for standard and suggested improved FBMC structures was given. The complexity requirement for each modulator architecture was derived. Beside design structure, the complexity is affected by the FFT algorithm and calculations of complex numbers multiplications. The complexity requirements were calculated in terms of number of real addition and multiplications. The simulation results show that PPN is more efficient than FS. The improved PPN structures can achieve a complexity reudction of almost half compared to the Standard PPN.

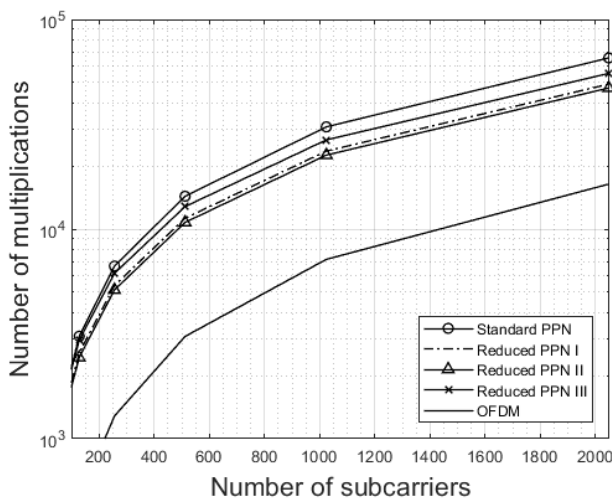Fig. 10. Number of multiplications for the improved FBMC transmitters as a function of the number of subcarriers N

REFERENCES

[1] C. Bockelmann, N. Pratas, H. Nikopour, K. Au, T. Svensson, C. Ste-fanovic, P. Popovski, and A. Dekorsy, "Massive machine-type communi-cations in 5G: Physical and mac-layer solutions," *IEEE Communications Magazine*, vol. 54, no. 9, pp. 59–65, 2016.

[2] R. Gerzaguet, N. Bartzoudis, L. G. Baltar, V. Berg, J.-B. Doré, D. Kténas, O. Font-Bach, X. Mestre, M. Payaró, M. Färber, and K. Roth, "The 5G candidate waveform race: a comparison of complexity and performance," *EURASIP Journal on Wireless Communications and Networking*, vol. 2017, no. 1, p. 13, Jan 2017. [Online]. Available: https://doi.org/10.1186/s13638-016-0792-0

[3] D. Mattera, M. Tanda, and M. Bellanger, "Frequency-spreading imple-mentation of OFDM/OQAM systems," in *2012 International Symposium on Wireless Communication Systems (ISWCS)*, Aug 2012, pp. 176–180.

[4] P. Siohan, C. Siclet, and N. Lacaille, "Analysis and design of OFDM/O-QAM systems based on filterbank theory," *IEEE Transactions on Signal Processing*, vol. 50, no. 5, pp. 1170–1183, May 2002.

[5] L. Varga and Zs. Kollár, "Low complexity FBMC transceiver for FPGA implementation," in *Radioelektronika, 2013 23rd International Conference*, Apr. 2013, pp. 219–223.

[6] Zs. Kollár and H. Al-amaireh, "FBMC transmitters with reduced com-plexity," *Radioengineering*, vol. 27, no. 4, pp. 1147–1154, Dec. 2018.

[7] Y. Dandach and P. Siohan, "FBMC/OQAM modulators with half complexity," in *2011 IEEE Global Telecommunications Conference - GLOBECOM 2011*, Dec 2011, pp. 1–5.

[8] P. Duhamel and H. Hollmann, "'split radix' FFT algorithm," *Electronics letters*, vol. 20, no. 1, pp. 14–16, 1984.

[9] H. V. Sorensen, D. Jones, M. Heideman, and C. Burrus, "Real-valued fast fourier transform algorithms," *IEEE Transactions on acoustics, speech, and signal processing*, vol. 35, no. 6, pp. 849–863, 1987.

[10] E. O. Brigham, *The Fast Fourier Transform*. Prentice-Hall Inc., 1974.

Husam AL-AMAIREH was born in 1973. He received his M.Sc. degree in computer science from Yarmouk University in Jordan in 2004. He is pursu-ing a Ph.D. degree at the Department of Broadband Infocommunication and Electromagnetic Theory at the Budapest University of Technology and Eco-nomics. He is currently a member of the MATLAB Laboratory. His research interests are digital signal processing and wireless communications.

Zsolt KOLLÁR was born in 1983. He received his Ph.D. degree in electric engineering from the Bu-dapest University of Technology and Economics in 2013. He is currently an assistant professor at the Department of Broadband Infocommunication and Electromagnetic Theory. Since 2016, he is the head of the MATLAB Laboratory. His research interests include digital signal processing, quantization ef-fects and wireless communication.

Optoelectronic mixer with photoconductive switch for 1550 nm wavelengths

Róbert Horváth, Jean-François Roux, Julien Poëtte and Béatrice Cabon

Abstract—We demonstrate an optoelectronic mixer based on an ultrafast InGaAs photoconductive switch and its use in an innovative heterodyne detection system for Radio over Fibre transmission. The advantage of the proposed switch is its relatively flat response curve in a wide frequency range up to 67 GHz. Two mixing schemes are presented through I-Q modulated data-stream down-conversion. The data can modulate either the electrical signal or the optical signal. In case the electrical signal is modulated, a mode-locked semiconductor laser diode is used as an optical local oscillator at the self-oscillating frequency of 24.5 GHz. The InP based quantum-dash mode-locked laser emitting in the 1570 nm wavelength range is stabilized by a feedback loop and shows a low phase noise in order to increase the mixing performances of the detection apparatus. In a second experiment, the photoconductive switch is combined with a continuous wave laser to demonstrate the feasibility of down converting an optically provided data-stream with an electrical local oscillator.

Index Terms— *heterodyne mixing, millimetre-wave receiver, mode-locked laser, optoelectronic mixer, photoconductive switch, radio over fibre.*

I. Introduction

Telecommunication systems nowadays are increasingly moving towards photonic solutions due to the advantage of high bandwidth and low losses, along with the easy integration with fibre-based networks. Microwave Photonics (MWP) is the interdisciplinary field giving the technology for the most advanced systems. Radio over fibre (RoF) networks are one of the beneficiaries of MWP. In the wireless link of a RoF network, millimetre-wave (mmW) generation with photonic solutions is already proved to be suitable for systems operating in the millimetre-wave range [1]. Optoelectronic mixers can also take advantage of the photonic MMW generation and can be used at the receiver side of the RoF networks. Usually, the downconversion of received signals is performed with an electronic mixer with electronic radio frequency (RF) local oscillators. In this paper, we propose an original optoelectronic system utilizing a wide bandwidth photoconductive switch (PSW) as an optoelectronic mixer. The system is working in the 1550-1570 nm wavelength range, making it compatible with telecommunication networks. Even if photomixers are frequently used for THz generation and detection [2], few demonstrations of their use at RF frequencies for telecommunications experiment have been published. In a

previous research, an InGaAs PSW based optoelectronic mixer was already investigated [3]. Because of the rather large photocarrier-lifetime of the simple InGaAs semiconductor the results showed only 20 GHz electrical bandwidth, and 300 MHz optical bandwidth. Here, the ultra-fast response time of the used photoswitch in our system results in a much larger optical and RF bandwidth, potentially above 100 GHz. The system is also taking advantage of the high-stability of an InP based semiconductor mode-locked laser (MLL) with optical feedback. Together these components give a simple and robust optoelectronic mixer for mmW applications. In a first setup, the local oscillator is optically provided using a semiconductor MLL or an externally modulated continuous wave (CW) distributed feedback (DFB) laser. The RF signal at the input of the mixer is carrying the data. This first scheme, named as Setup-I, is illustrated in Fig.1. A second setup, named Setup-II, is using an electrical local oscillator provided by an RF synthesizer. The optical signal is coming from a laser source which output is modulated by a RoF signal (carrying the data) thanks to an external electro-optic modulator. Fig. 1. is also illustrating this second setup.

In the next Section we are introducing the photoconductive switch, the MLL stabilization setup and the CW DFB laser. Section III and IV are explaining the two optoelectronic mixer schemes through data-stream downconversion and demodulation experiment. A conclusion is given in Section V.

II. Mixer components

A. Photoconductive switch

The proposed system uses a PSW as the optoelectronic mixer element. The switch schematic view is illustrated in
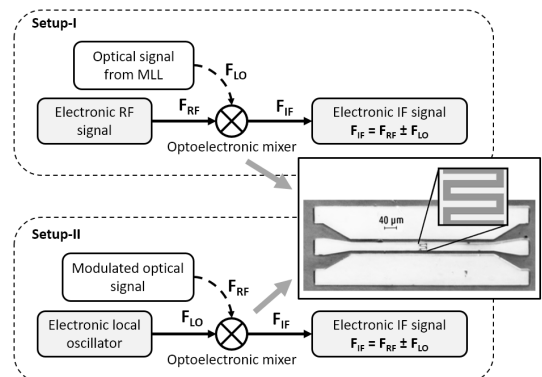

Fig. 1. The two optoelectronic mixing schemes with a photoconductive switch as a hybrid mixing device. Inset: schematics of the switch
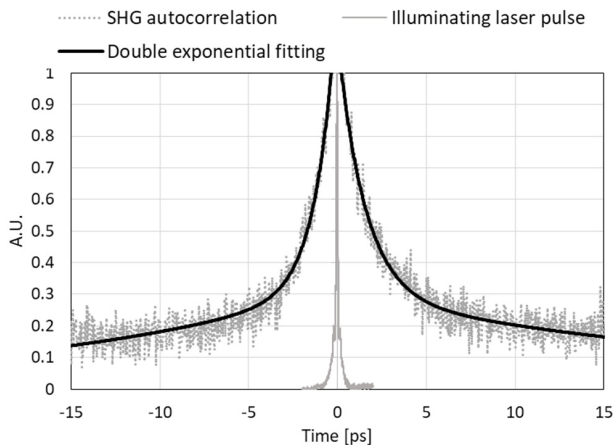
Fig. 2. Optical pulse response of the photoconductive switch (dotted grey) with the double exponential fitting (black). Continuous grey illustrates the incident ultrashort laser pulse for the measurement

the inset of Fig.1. The device samples are provided by the Ultrafast Photonics Group at University College London (UCL). Characterization of the samples has been performed previously at UCL in [4] and also by our group in [5].

The device consists of a coplanar waveguide (CPW) based on InP substrate. Both ends of the CPW are designed for coplanar RF-probe connection for easy manipulation. The centre conductor of the waveguide is interrupted with an etched InGaAs mesa in the middle. On top of this mesa an interdigitated electrode structure is deposited (magnified view in the inset of Fig.1.). The device is nitrogen-ion implanted in order to create a large number of defects in the InGaAs semiconductor material. These defects are ensuring the ultra-fast recombination time of generated photocarriers under 1550-1570 nm wavelength laser illumination.

The characterization in [5] showed an ultrafast response time of 1.2 ps for the switch, using an optoelectronic autocorrelation experiment [6]. The measurement was performed with short 90 fs long optical pulses centred at the wavelength of 1550 nm. The photoswitch response curve is illustrated on Fig. 2 including the optical pulse (in continuous grey) and the dual exponential fitting (in black) with the equation of $A*e^{-t/T1}+B*e^{-t/T2}$. The best fit was obtained for T1 = 1.2 ps and T2 = 20 ps and A= 0.6 and B= 0.2. We note that the contribution of the long 20 ps is low and that the main response of the device is ruled by the fastest constant time. We also measured that the device has a good dark resistance of 6 kΩ and a low equivalent capacitance of 5.7 fF. This picosecond response time is due to the large number of defects and it is insuring an optoelectronic cut-off frequency of the photoconductive device above 100 GHz. In [5], we also demonstrated its ultrawide electrical bandwidth with a relatively flat response curve over the 10-67 GHz range when the device is used as a mixer in between an RF signal and an optical local oscillator produced by a self-oscillating MLL. This wide bandwidth is a significant advantage for optoelectronic mixing applications, it allows the use of a wide range of frequencies and large signal bandwidths for high-speed communication.
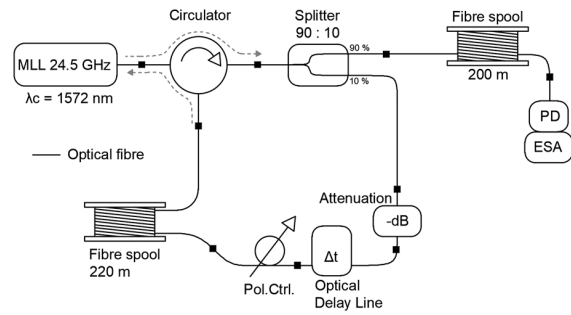
Fig. 3. Setup of the all-optical feedback loop for the MLL stabilization. PD: Photodiode; ESA: Electrical Spectrum Analyzer; MLL: Mode-locked laser.

B. Mode-locked Laser

In optoelectronic mixers, the local oscillator frequency is usually provided by an optical source modulated by an external device such as an electro-optic Mach Zehnder modulator (EO-MZM). In our system (setup- I) we are using a semiconductor InP based quantum-dash mode-locked laser as a source of the optical signal which allows to get rid of the external modulator, the chip-on-a-carrier is bonded to a microstrip line for the biasing electrical probe connection. The laser is provided by III-V Lab, Palaiseau, France. At a room temperature of 25°C and with 140 mA bias current the emitted central wavelength is around 1572 nm. The output optical signal contains 40 equally spaced modes in 8 nm bandwidth. The mode separation ~0.2 nm and corresponds to a self-oscillation frequency of 24.5 GHz. The output of the laser was couple into a single-mode standard SMF-28 fibre thanks to a coupler lens. To prevent disrupting back-reflections to the laser we used a fibre circulator after the pigtailed lens, the measured optical power at the circulator output is 8 dBm. In order to compensate for the intrinsic dispersion of the laser diode, 200 meters of SMF-28 fibre is used at output of the setup.

MLLs are known to provide a stable, low jitter pulse train with a linewidth in the 10-100 kHz range. We measured a free-running linewidth of 36 kHz. As the linewidth of the local oscillator in mixers is a crucial property regarding its performance, large linewidths can drastically corrupt the mixed signal quality. It is possible to improve the MLL stability with external manipulations: here we used a simple
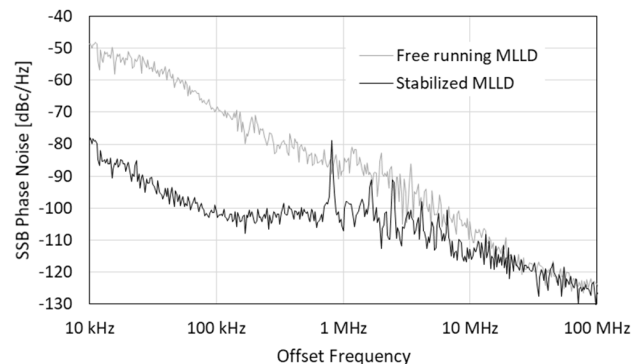
Fig. 4. SSB Phase noise curves for the free running and the stabilized MLL

optical feedback loop, as proposed in [7]. The long optical fibre based feedback adds a long delay time and acts as a high-Q external cavity added to the laser. The setup of the stabilization feedback can be seen on Fig. 3. A part of the laser signal is injected back into the MLL cavity thanks to a fibre based circulator. The loop also contains a polarization controller to adjust the polarization of the injected signal to correspond to the laser signal polarization. An attenuator was used to adjust the feedback signal power. A variable optical delay line was used to control with picosecond precision the feedback delay. We found that feedback attenuation of around 28 dB is sufficient for optimal stabilization. Higher feedback power results in a "chaotic" behaviour of the MLL, while lower feedback power gives a lower level of stabilization. The optical signal's average power at the output of the setup was measured to be 7 dBm.

We measured the single side-band phase noise of the fundamental beating signal for the free running and stabilized MLL with an Electrical Spectrum Analyser (ESA), the results are showed in Fig. 4. The stabilization resulted in a linewidth reduction of the beating signal below 1 kHz while the phase noise curve also showed a decrease of 30 dB, down to -100 dBc/Hz at 100 kHz offset frequency. The observed spurious peaks at 820 kHz and at its harmonics on the curve of the stabilized laser are corresponding to the free-spectral range (FSR) of the feedback loop, which has 220 meters of fibre in our case. Their power level in the RF spectrum are more than 20 dB below the main peak, which means their contribution is not too significant. It is important to note that mode-locked lasers are generating beating signals also at the harmonics of the fundamental tone, in this case at 49 GHz, 73.5 GHz and so on. The power level is similar for the first harmonics and the fundamental signal. In our experiments, only the fundamental beating signal will be involved in the mixing process.

In conclusion, such a feedback loop greatly enhances the

phase noise of the laser and this stabilized laser source with a 24.5 GHz beating fundamental frequency will provide a high quality local oscillator for down-conversion experiment.

C. Distributed feedback laser

In the first proposed scheme (Setup-I) and in the second proposed experiment (Setup-II) we also used a DFB laser that emits a continuous wave signal at 1551 nm. The optical power is maximum 10 dBm. The laser signal is intensity modulated by a Mach-Zehnder modulator (MZM) biased at its quadrature point. Due to the losses introduced by the modulator, at its output we measured an average power equal to 3 dBm. This modulated signal is used as the local oscillator or the data modulated signal in the following setups.

III. OPTOELECTRONIC MIXING – SETUP I

In the previous sections we introduced the two elements of the proposed optoelectronic mixer used in Setup-I: an ultrafast PSW with wide bandwidth, and an MLL with an external feedback loop providing a stable signal at 24.5 GHz with 7 dBm optical power. In a simple mixing experiment the system showed 72 dB mixing conversion loss in the 10-67 GHz range [5]. Despite this high level of losses, we note that this level is 8 dB better performance than the conversion loss of an unbiased Uni-Traveling Carrier photodiodes (UTC-PD) used as optoelectronic mixers [8].

In this section, the capabilities of our system used as a heterodyne detection stage is demonstrated with a data-stream downconversion and demodulation experiment. This detection apparatus can be used in the wireless receiver of a Radio over Fibre network. Where the received high frequency wireless signal containing the data, can be downconverted for signal processing. We first compare the performance obtained using the free running and the stabilized MLL. In a second step, we performed the experiment where the local oscillator frequency is provided by a different mmW generation solution: an intensity modulated CW laser source, a DFB laser modulated by an
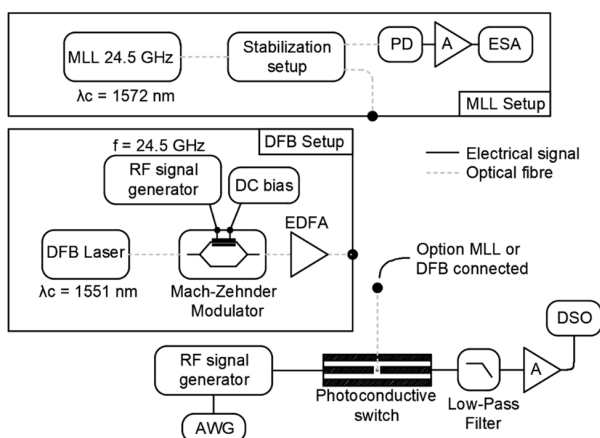
Fig. 5. Setup-I: Schematics of the heterodyne mixing experiment with data-stream modulated RF input signal and two cases of optical local oscillator. MLL: Mode-Locked Laser; DFB: Distributed Feedback Laser; EDFA: Erbium Doped Fibre Amplifier; PD: Photodiode; ESA: Electrical Spectrum Analyser; AWG: Arbitrary Waveform Generator; DSO: Digital Sampling Oscilloscope
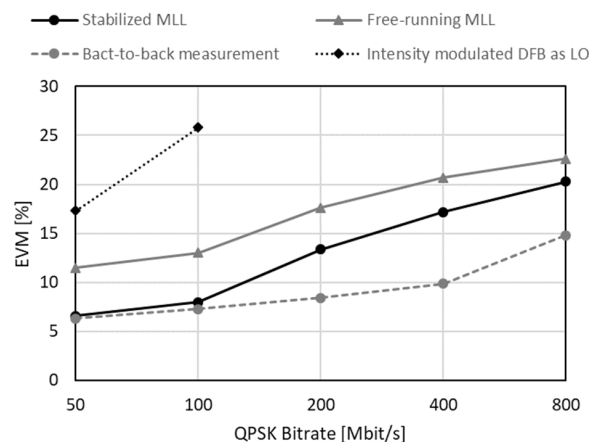
Fig. 6. Setup-I results. Measured Error Vector magnitude values versus the applied bitrate of the data-stream.

external MZM modulator with the same frequency of 24.5 GHz. The two configurations of the heterodyne stage are illustrated in Fig. 5. As the input of the PSW we used a signal from an RF signal generator having a 20 GHz carrier signal modulated by quadrature phase shift keying (QPSK) modulated data with different data-rates (50-100-200-400-800 Mbit/s). The I and Q of the modulated signal were generated by an Arbitrary Waveform generator (AWG) which outputs are directly connected to the wideband I-Q modulation inputs of a signal generator. The electrical carrier signal was added by this signal generator.

At the output of the photoconductive switch and after 38 dB amplifier, we analysed the mixed signal at the intermediate frequency (IF) of 4.55 GHz with a Digital Sampling Oscilloscope (DSO). The laser signals are guided to the photoswitch through standard single mode optical fibres to illuminate the InGaAs mesa with a bare-end pigtailed fibre. As mentioned above, the MLL had an output optical power of 7 dBm. Due to the modulator losses the DFB laser requires an Erbium Doped Fibre Amplifier (EDFA) to reach the same optical power as in case of the MLL. However, using this power level for the DFB setup (7 dBm), the DSO was unable to demodulate the IF signal, so we further amplified the DFB setup's output optical power up to 17 dBm, in order to increase the IF power level.

The DSO's built-in software was capable of online demodulating the received signal. The systems and their mixing performances are compared through the analysis of the Error Vector Magnitude (EVM). The results are illustrated in Fig. 6. The dashed line shows a reference back-to-back measurement, where we directly connected the signal generator to the DSO with a carrier frequency of 4.55 GHz. The continuous grey line shows the results obtained with the free-running MLL source used as the local oscillator while the continuous black curve corresponds to the results obtained with the stabilized MLL source. We can observe a reduction of 3 points on average of the EVM values for the stabilized source compared to the free running case, which shows the higher performances of the stabilized MLL. However, the difference is decreasing for higher bitrates, indicating that the setup is limited not only by the phase noise of the local oscillator, but possibly by the impedance matching of the equipment and the photoswitch. The dotted black curve shows the performance obtained with the amplified DFB laser. We can observe an increase of

17 points of the EVM, up to 25.8 %, for the case of 100 Mbit/s data-rate compared to the stabilized MLL. Above 100 Mbit/s the signal to noise ratio (SNR) of the IF signal was too low for the demodulation using the DFB setup as local oscillator. These results show the advantage of the stabilized MLL used as the local oscillator over the intensity modulated continuous wave laser source.

In the case of using the DFB, the modulation depth of the laser is very low compared to the MLL case, due to the sinusoidal shape of the modulator transfer function, compared to the ultrashort pulses of the MLL. This induces higher level of continuous emission because of the limited MZM modulating power in order to stay in the linear regime. These CW contributions in the system are unused power, which results in a lower RF power and consequently a lower IF power at the mixer output. Other degradations of the signal results from the added noise level due to the use of the EDFA.

This optoelectronic mixer scheme has the advantage of a simple setup, the mixer device is a passive component, active elements are only the optical and electrical sources generating the signal to be mixed, and the electrical amplifier of the IF signal.

IV. OPTOELECTRONIC MIXING – SETUP II

In the previous section we saw the downconverting capabilities of the photoswitch and its application in a system. The local oscillator was provided by an optical source and the processed data-stream was an electrical RF signal. In the optical section of a RoF system the optically provided data-stream is converted to the electrical domain with a photoconductor and then is transmitted wirelessly. The optical signal is modulated with the data on a carrier signal at a frequency f_c, thus after detection the electrical signal has the same f_c carrier signal. In the following, we are demonstrating our proposed system for downconverting the optically received data signal for signal processing. The scheme can demodulate the data stream to the baseband or to directly convert the data-stream to a different frequency with the help of an electrical local oscillator. The setup is
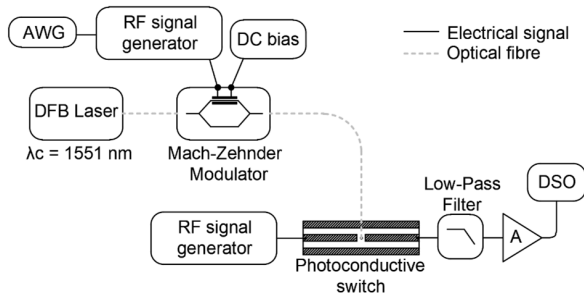

Fig. 7. Setup-II: schematics with intensity modulated DFB laser by a data-stream with electrical local oscillator.
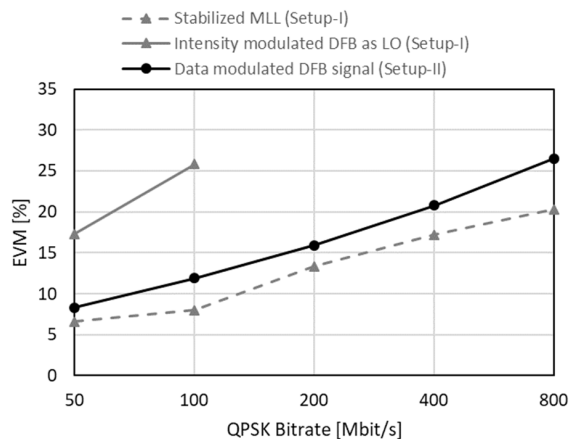

Fig. 8. Setup-II results. Measured Error Vector magnitude values versus the applied bitrate of the data-stream. Setup-II results are compared to Setup-I.

illustrated on Fig. 7. The same DFB laser as in the previous setup is used here without the EDFA. The generated data-stream is from the AWG and the signal generator is modulating the optical signal through the Mach-Zehnder modulator. Utilizing a MZM we can achieve higher bandwidths compared to directly modulating the DFB laser cavity. The average optical power after the MZM is 3 dBm (2 mW). In the experiment we used the same LO frequency as in the case of Setup-I, but now we have an electrical LO at the input of the photoswitch. This local oscillator generates a sinusoidal signal with 19 dBm power and 24.55 GHz frequency provided by an Agilent signal generator. This LO signal has a superior frequency stability and quality compared to the ones provided by the lasers for Setup-I. The carrier frequency of the data-stream is also the same as in the previous setup at 20 GHz.

These settings resulted again in a downconverted signal at 4.55 GHz at the output of the photoswitch. A low-pass filter was filtering out the feedthrough signals through the photoswitch and prevented the overload of the following low-noise amplifier (38 dB). A DSO was performing the data demodulation after the amplifier. The data-stream in this case was also QPSK modulated with 50-100-200-400-800 Mbit/s data rates. As in the previous setup, we were measuring the demodulated signal's Error Vector Magnitude (EVM) value. The results are shown in Fig. 8 along with the results from the stabilized MLL case and DFB case from Setup-I as an indication. We measured an EVM of 8.3 % for 50 Mbit/s, which increases to 26.5 % for 800 Mbit/s. The results are close to the one obtained with an optical LO from the stabilized MLL.

V. Conclusions

We demonstrated two optoelectronic mixer schemes utilizing a photoconductive switch. In the first scheme, the local oscillator is an optical signal from an MLL at a frequency of 24.5 GHz, with a reduced linewidth thanks to a stabilizing all-optical feedback loop. The wide bandwidth of the PSW, estimated to be higher than 100 GHz, gives a wide possible frequency range for the system design. The mixing conversion loss is rivalling with the unbiased UTC-PDs and shows good stability over a wide frequency range. In order to investigate the benefit of such an optoelectronic system, as a proof of concept we performed QPSK data demodulation in a RoF data transmission link. The higher performance of the stabilized MLL over the free-running MLL and modulated DFB signal was shown. We measured an EVM of 6.6 % for 50 Mbit/s QPSK modulated signal which increased to 21.6 % with a higher data-rate of 800 Mbit/s.

In the second optoelectronic mixing scheme, the local oscillator signal is electrical. The data-stream is intensity modulating a continuous wave DFB laser. The mixing showed a good performance with 16 % EVM for 200 Mbit/s data rate. A possible application of the photoconductive switch is in an RoF network, where the data-stream modulated optical signal is received then can be directly down or up converted for electrical transmission to a different carrier frequency depending on the application demands.

The two experiments demonstrate the capability of using either the optical or the electrical signal as local oscillator. The measured EVM values are compatible with wireless communication requirements in case of Forward Error Correction (FEC) coding of the data-stream, where part of the transmitted data is used for error correction. The results can be improved by utilizing higher power lasers and low-noise amplifiers and also by improving the switch structures as in [9] for higher efficiency of the optical detection. These results are showing the flexibility of the photoswitch, operating over a large bandwidth, both in the electrical and optical domain. The schemes are giving a feasible photonic solution for a heterodyne receiver in a RoF wireless link or for the optical link and opens the way to the design of new photonic assisted mmW telecommunication links.

References

[1] Nagatsuma, T., Ducournau, G., & Renaud, C. C. (2016). "Advances in terahertz communications accelerated by photonics," Nat Photon, 10(6), 371–379. DOI: 10.1038/nphoton.2016.65

[2] R. Dietz, B. Globisch, H. Roehle, D. Stanze, T. Göbel, and M. Schell, "Influence and adjustment of carrier lifetimes in InGaAs/InAlAs photoconductive pulsed terahertz detectors: 6 THz bandwidth and 90dB dynamic range," Opt. Express 22, 19411-19422 (2014). DOI: 10.1364/OE.22.019411

[3] H.-J. Song, T.-W. Kim, S. J. Jo, C.-H. Lim, K.-H. Oh, S.-G. Ihn, and J.-I. Song, "Microwave Photonic Mixer Utilizing an InGaAs Photoconductor for Radio over Fiber Applications," IEICE Trans. Electron., vol. E90, p. 457, 2007. DOI: 10.1093/ietele/se90-c.2.457

[4] C. Graham, R. Gwilliam, and A. Seeds, "Nitrogen ion implanted InP based photo-switch," Opt. Express 20, 26696-26703 (2012). DOI: 10.1364/OE.20.026696

[5] R. Horvath, J. F. Roux, J. L. Coutaz, J. Poëtte, B. Cabon and C. Graham, "Ultrafast InGaAs photoswitch for RF signal processing," 2017 International Conference on Optical Network Design and Modeling (ONDM), Budapest, 2017, pp. 1-5. DOI: 10.23919/ONDM.2017.7958541

[6] K. Grigoras, A. Krotkus, and A. Deringas, "Picosecond lifetime measurement in semiconductor by optoelectronic autocorrelation," Electronics Letters, 27, 1024-1025, (1991).

[7] A. Akrout, F. van Dijk, G. H. Duan, A. Shen, F. Lelarge and A. Ramdane, "Low phase noise optical oscillator at 30Ghz using a quantum dash mode-locked laser associated with an optical self injection loop," 2009 International Topical Meeting on Microwave Photonics, Valencia, 2009, pp. 1-3.

[8] E. Rouvalis, M. Fice, C. Renaud, and A. Seeds, "Optoelectronic detection of millimetre-wave signals with travelling-wave unitravelling carrier photodiodes," Opt. Express vol. 19, 2079-2084, 2011. DOI: 10.1364/OE.19.002079

[9] E. Peytavit, S. Formont, J.-F. Lampin, "GaAs Fabry-Perot cavity photoconductors: switching with picojoule optical pulses," Electron. Lett., 49 (3), pp. 207-208 (2013). DOI: 10.1049/el.2012.3993

Róbert Horváth has received B.Sc. and M.Sc. degrees in electrical engineering from Budapest University of Technology and Economics, Budapest, Hungary in 2013 and 2015 respectively. Since October, 2015 he is pursuing his Ph.D. degree at IMEP-LAHC laboratory (Grenoble-INP, CNRS) in Grenoble, France as an Early Stage Researcher in the FiWin5G Marie-Curie ITN project. His interests are in Microwave photonics, photoconductive switches, photonic assisted Analog-to-digital conversion and semiconductor mode-locked laser.

Jean-François Roux Engineer and M. Sc from the University of Strasbourg, France, in 1990, PhD from Institut Polytechnique Grenoble (Grenoble-INP) in 1995 for a thesis in non-linear integrated optics. He joined the Université Savoie Mont-Blanc in 1996 where he is now an associate Professor at IMEP-LAHC Laboratory. His research activities concern the generation, detection and processing of RF to THz signals using ultrafast optoelectronics. He is also involved in THz time domain spectroscopy and generation of THz signals using high power femtosecond laser.

Julien Poëtte Engineer and B.Sc in 2002, PhD in physics in 2005 from RENNES 1 University (France), is associate professor at Grenoble-INP since 2008 (National Polytechnics Institute of Grenoble, France). His research activities concern next generation communication systems involving microwave-photonics techniques, optical noise, and optical solution for carrier generation at millimeter wave frequencies and beyond.

Béatrice Cabon, Ph.D. from the Institut Polytechnique Grenoble (Grenoble-INP), France, in 1986, and professor from 1989. She is Head since 1993 of a research group on microwave-photonics techniques at IMEP-LAHC, Institute for Microelectronics, Electromagnetism and Photonics laboratory, Grenoble France. From 1998 to 2008, she has been also coordinator of the club "optics and microwaves" of the French Optical Society. She also coordinated two European projects Networks of Excellence funded by the European commission, FP6-IST- 2001-32786 « NEFERTITI » (2002-2005) and FP6-IST-26592 « ISIS » (2006-2009). Her research interests include microwave-photonics, photonic- microwave signal processing, and optical links for high bit rate signals. She has authored or co-authored more than 300 technical publications and is the Editor of five books in these areas.

A Systematic Analysis and Design of a High Gain Microstrip Antenna based on a Single EBG Layer

Yahiea Alnaiemy, Taha A. Elwi, Lajos Nagy and Thomas Zwick, *Senior Member, IEEE*

Abstract— In this paper, an Electromagnetic Band Gap (EBG) lens of a single layer is invented to improve the gain of a truncated slotted square patch antenna for the Wi-Fi applications. The proposed EBG lens is structured from 5×5 planar array. The individual unit cell is basically shaped as a couple of a split concave conductive patch. The proposed EBG structure performance is tested numerically using Finite Integration Technique (FIT) formulations of CSTMWS and analytically using circuit theory. Then, the antenna performance in terms of |S11|, the boresight gain, and radiation patterns are reported and compared to the performance before introducing the EBG lens to identify the significant enhancements. The proposed EBG antenna is simulated numerically inside FIT formulations of CSTMWS time domain (TD) solver. A significant gain enhancement of 11.1 dBi at 2.45 GHz and a front to back ratio (F/B) about 22 dB are achieved after introducing the EBG lens. The antenna performance is validated using a frequency domain (FD) solver based CSTMWS formulations to obtain excellent agreements between the two invoked methods.

Index Terms—EBG; microstrip antenna; CST MWS

I. INTRODUCTION

Since the last century, Yablonovitch [1] and John [2] investigated the EBG structures conceptions. After that significant efforts have been established to realize the perfect lenses concepts. Therefore, the theoretical notions were founded from Bloch wave principles, reciprocal space, Brillion zones, and dispersion relations [3], [4]. The EBG structures were realized and engineered in a similar method of defecting traditional electronic semiconductor crystals to be classified according to 1D, 2D, and 3D crystals. For instance, in [5], a 2D EBG structure was investigated from a dielectric substrate at the microwave regime. An etched 2D metallic aperture array on a dielectric slab to create a periodical variation in the dielectric constant of the medium was investigated for the antenna performance enhancement in [6]. EBG structures were applied to miniaturize the antenna size and increasing the bandwidth [7]. Usually, the EBG

structures could be patterned either on the metal patches or etched from ground planes as proposed in [8], [9]. The EBG possess several untraditional features such as zero effective refractive index and distinctive stopbands [10]. However, EBG structures are unresonant structures and may suffer from two fundamental limitations: narrow bandwidth and high losses due to the conducting inclusions [11]. In [12], an EBG structure was folded on a folded ground plane of an antenna for breast cancer detection. Another antenna structure based miniaturized EBG ground plane defect for Multiple-Input and Multiple-Output (MIMO) application was proposed in [13]. The proposed antenna in [14] was constructed on EBG ground plane defects for Ultra-WideBand (UWB) application. Nevertheless, the work in [15] was conducted for optical application based EBG flat lenses. Printed dipoles based EBG arrays of a geometry were proposed in [16] for Wi-Fi applications. Nevertheless, a high impedance structure based EBG structure attached to a dipole antenna was reported in [17] for sensor applications. A folded MIMO antenna array was investigated in [18] to reduce the mutual coupling effects. The proposed structure in [19] was consistent of periodical grounded dielectric substrate deposited with square conductive patches connected through vias to the ground. It has been demonstrated that EBG structures exhibits zero refractive indices to achieve highly directive antennas with enhanced bandwidth and excellent gain of miniaturized size [20] with low mutual coupling for MIMO applications [21].

In this paper, a new EBG design of a single finite layer with improved properties is proposed as a uniform 2D array of periodic metallic structure on top of a microstrip antenna for gain enhancements. The combination of the proposed EBG structure with the microstrip antenna may suit different wireless applications over the frequency range from 2.45 GHz to 2.55 GHz band to fit the fixed and mobile communication systems, point-to-point microwave links, and telemetry devices such as Unmanned Aerial vehicles (UAV). The numerical simulations are performed by conducting the FIT analysis based on TD and FD solvers to examine the proposed EBG properties [22]. The rest of this paper is organized as follows: In Section II, the description for the proposed EBG lens is presented; Section III discusses the radiation characteristics and performances of the microstrip antenna with and without EBG layer; and finally, the paper is concluded in Section IV.

Yahiea Alnaiemy and Lajos Nagy are with Budapest University of Technology and Economics, Budapest, Hungary (e-mail: {yahiea, nagy}@hvt.bme.hu)

Taha A. Elwi is with Al-Mammon University College, Baghdad, Iraq (e-mail: taelwi82@gmail.com)

Thomas Zwick is with Institute of Radio Frequency Engineering and Electronics (IHE), Karlsruhe Institute of Technology (KIT), Germany, *Senior Member, IEEE* (e-mail: thomas.zwick@kit.edu)

II. EBG GEOMETRICAL DETAILS

To test the proposed EBG performance, a unit cell of EBG is positioned at the center of a fictitious waveguide as shown in Fig.1 to retrieve the transmission and reflection characteristics of the EBG-structure model given by S-parameters. The two waveguide ports of TEM-like modes are shown in Fig.1. The top and bottom sides of the y-axis are assigned as Perfect Magnetic Conductors (PMC) and the left and right hand side of the z-axis are assigned as Perfect Electric Conductors (PECs) in order to create internal environment of waveguide as depicted in Fig. 1.
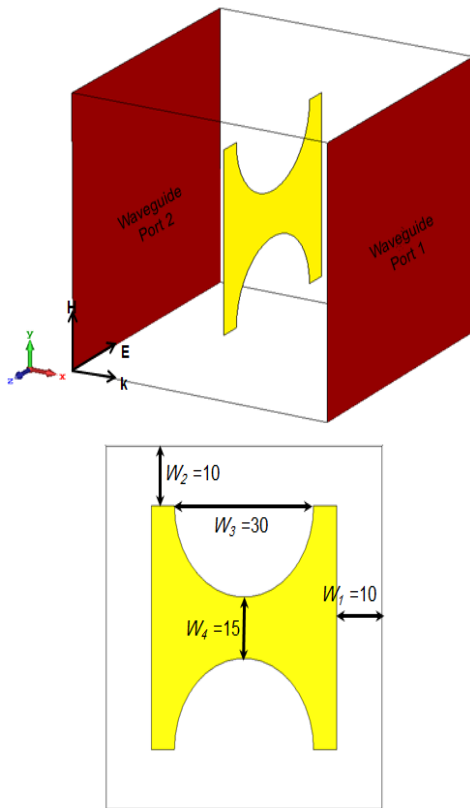
Fig. 1: CSTMWS numerical setup and unit cell dimensions in mm.

The proposed EBG layer dimensions are 240×240mm² as shown in Fig. 2(a). Such layer is constructed from 5×5 unit cells; each one comes with four design variables given by: W_1, W_2, W_3 and W_4 to optimize the EBG performance at the desired frequency band. These variables are adjusted to resonate at 2.45 GHz. The maximum proposed EBG unit cell dimensions are 0.32λ×0.32λ where λ is wavelength at 2.45 GHz repeated and aligned on the x- y plane, where EBG is based on copper layer of conductivity 5.8×10⁷S/m and the EBG lens thickness is 0.1 mm. The design variables are fixed at 30mm and 15mm for W_3 and W_4, respectively. While, the other two variables W_1 and W_2 are changed together from 2mm up to 10mm with step of 2mm to reach the resonance in the transmission ($|S_{12}|$) around 2.45 GHz. As

seen in Fig. 2(b), the proposed unit cell shows a very sensitive response to W_3 and W_4 change. This change is due to the capacitive coupling effects between the unit cells edges.
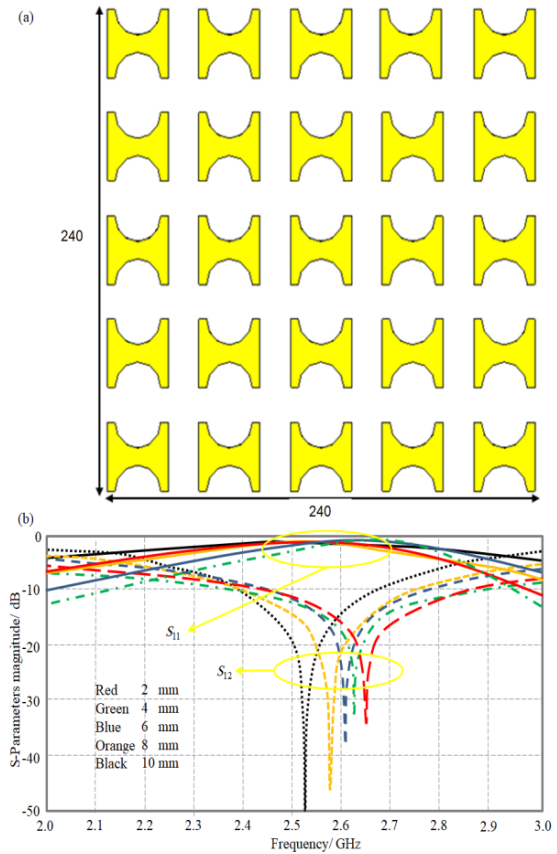
Fig. 2: The proposed EBG details; (a) EBG layer dimensions in mm and (b) S-parameters spectra based the parametric study.

Fig. 3 shows the transmission and reflection evaluation of the EBG-structure model with respect to the analytical circuit analysis. From the obtained results, it is found that the maximum ($|S_{12}|$) is around at 2.55GHz. Unsymmetrical unit cell is chosen to achieve a gain enhancement on both x- and y- axes that would be very useful for the circular gain enhancement.
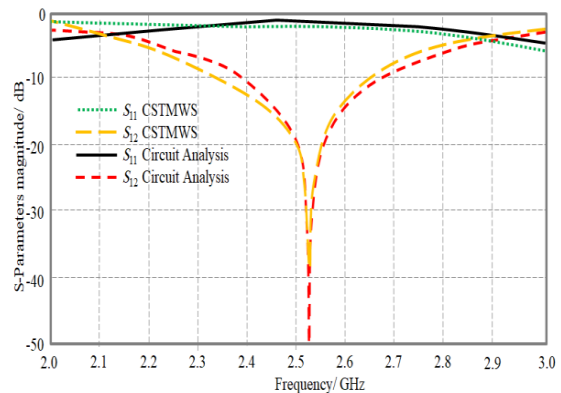
Fig. 3: Obtained S-parameters spectra.

The proposed EBG unit cell equivalent circuit is present-
ed in Fig. 4. Basically, the separation distance the concave
patches can be presented by a capacitor (C_1). However, the
separation distance between the concave sides is presented by
the capacitor (C_2). The concave part is given by an inductor
(L). The load resistance is given by the free space impedance
that is given by (377Ω). The values of the proposed equiva-
lent circuit are listed in Table 1.
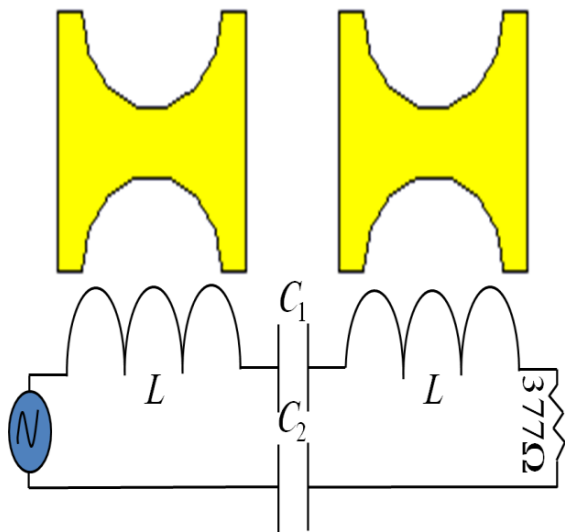
Fig. 4: Equivalent circuit.

TABLE I EBG EFFECTIVE CIRCUIT PARAMETERS

Parameter	Value
L	0.9 nH
C_1	1.1nF
C_2	2.3nF

Next, to obtain the maximum gain enhancement, the pro-
posed EBG layer is located to cover the microstrip antenna at
130 mm above the patch antenna. The material between the
patch antenna and EGB layer is rigid foam of ε_r=1.039 and
loss tangent $tan\delta$=0.0097. The distance between the patch
and EBG layer is optimized by using the same procedure that
was described in [9]. All related EBG lens and the microstrip
antenna dimensions are depicted in Fig 5.

The microstrip patch is designed as a square geometry of
40×25mm2 mounted on a dielectric substrate made of Rogers
RO3203 with εr=3.02 and tanδ=0.0016 of 1mm thickness.
The ground plane is installed on the backend of the substrate
as a square copper layer with 240×240 mm2. The patch struc-
ture is considered as a truncated square patch to achieve a
circular polarization pattern. The 50 Ω SubMiniature version
(SMA) connector was used with a discrete wave port to excite
the patch antenna.
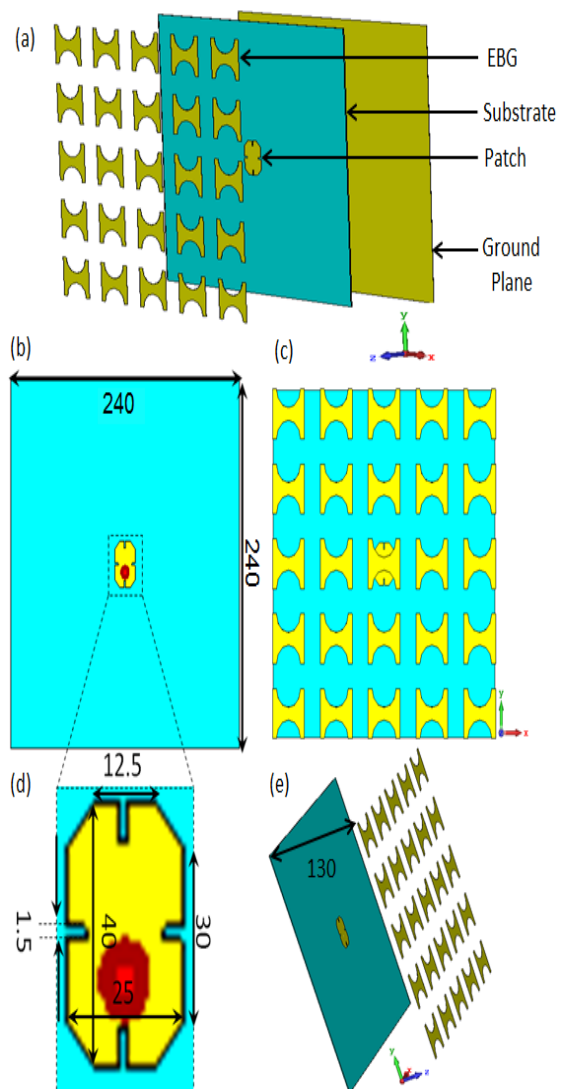
Fig. 5: The antenna geometrical details; (a) 3D view of the microstrip
antenna with the EBG lens, (b) and (c) front view of the microstrip antenna
and the array of EBG lens, (d) magnified picture for the microstrip antenna
patch, (e) side view of the EBG lens positioned over the microstrip antenna.
All dimensions are in mm.

III. RESULTS AND DISCUSSION

The effects on the antenna performance after introducing
the EBG lens to the antenna structure is investigated using
the TD and FD solvers based on CST MWS formulations
[20]. The TD solver is realized by conducting the use of
perfect boundary approximations and thin sheet techniques.
Nevertheless, a hexahedral volumetric mesh, see Fig. 6(a),
is applied to calculate the S-parameters and the electro-
magnetic fields simultaneously. However, the FD solver
conducts the tetrahedral meshing, as presented in Fig. 6(b),
of mixed order field computation calculating the phase de-
embedding of the S-parameters.
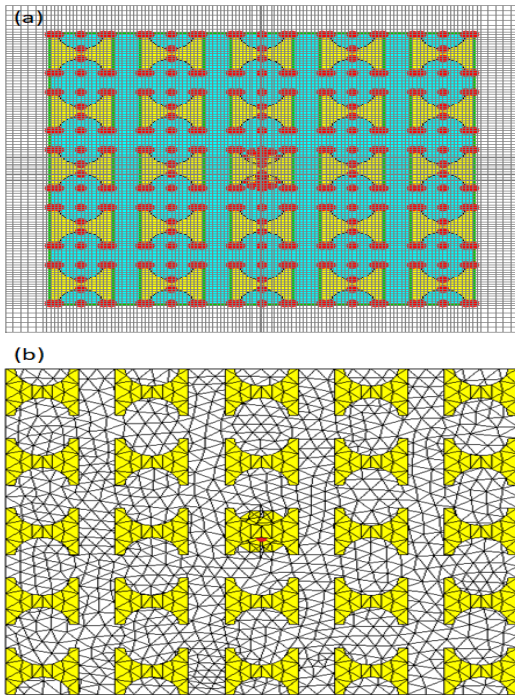
Fig. 6: Mesh view; (a) hexahedral mesh and (b) tetrahedral mesh.

Next, the focus on the effects of adding the EBG lens on antenna performance including the bandwidth, matching impedance, and frequency resonance is evaluated by monitoring the $|S_{11}|$ spectrum. Moreover, the gain, radiation efficiency, and the beamwidth are compared before and after introducing the proposed EBG structure. The $|S_{11}|$ spectra are presented in Fig. 7(a) from both cases: before and after adding the EBG lens. In the obtained $|S_{11}|$ spectrum, the change is found due to introducing the EBG lens that adds a capacitive coupling with the microstrip antenna [12]. It is concluded that the antenna shows a frequency resonance at 2.45 GHz, however, the resonance is shifted to 2.43 GHz after adding the EBG lens. The antenna gain is enhanced from 5.6 dBi up to 11.1 dBi after adding the EBG lens due to focusing the emerged beams from 99° to 26.7° as seen in Fig. 7(b), therefore by minimizing the beam in both θ- and ϕ- cut planes we will reach the maximum gain according to relation (1) [23].

$$G_O \cong \frac{30,000}{\varphi\theta} \qquad (1)$$

Insignificant decay is observed in the radiation efficiency of the microstrip antenna from 90% to 88.4% due to the effects of the conductor losses from the EBG structure. Such degradation is found to be much less than published degradation values; this because of the use of a single layer in the proposed design. From Fig. 7(b), the F/B ration is calculated using equation (2) [23].

$$\text{F/B} = G_f - G_b \qquad (2)$$

Where, G_f and G_b are the magnitude of the front lobe in dB value and the magnitude of the back lobe in dB, respectively. Therefore, from the radiation pattern presented in Fig. 7(b), the F/B = 11-(-11) =22 dB.
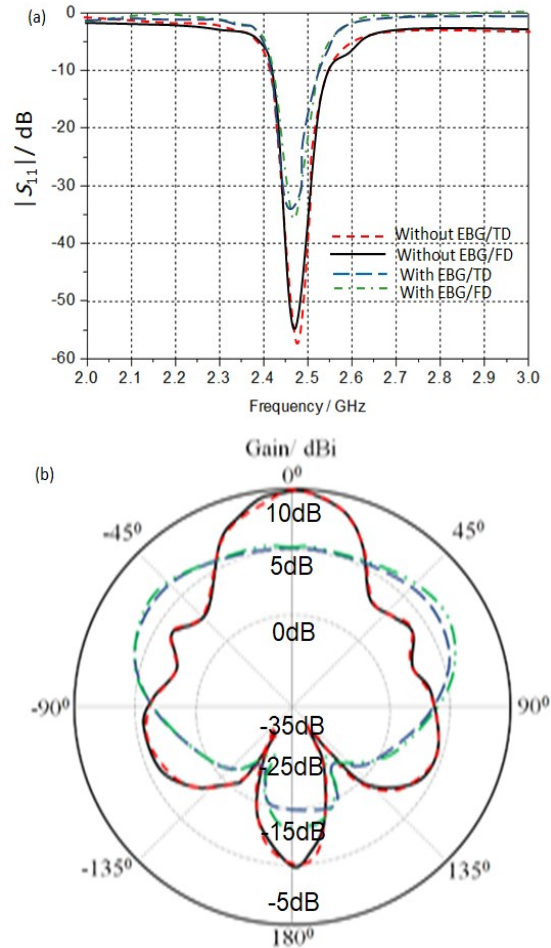
Fig. 7: Antenna performances with and without EBG lens; (a) |S11| spectrum and (b) Gain radiation pattern.

Next, to obtain the maximum gain enhancement, the proposed EBG layer is located to cover the microstrip antenna above the patch antenna this location of the EBG layer from the top of the patch is studied by running a parametric study. Therefore, the study starts with located the EBG layer above the patch from 10 mm to 190 mm with steps of 20 mm. It is found that the antenna perform the best gain at the boresight at 130 mm as can be seen in Fig. 8.
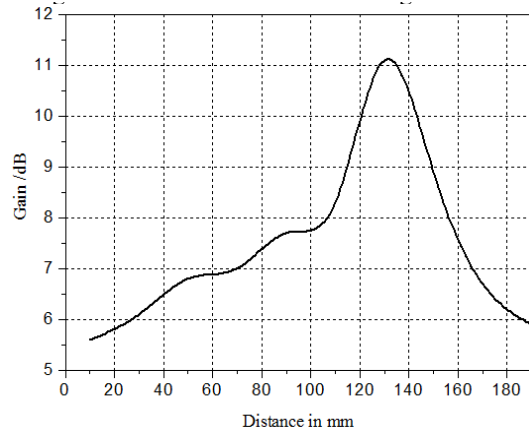
Fig. 8: Parametric-study of the proposed EBG Structure from the antenna structure: boresight gain.

In this section, we investigate the effect of varying the distance between the EBG layer and the patch on resonant frequencies behavior. It is observed from Fig. 9, that insignificant change in the $|S_{11}|$ spectrum with respect to the distance between the EBG layer and the patch.
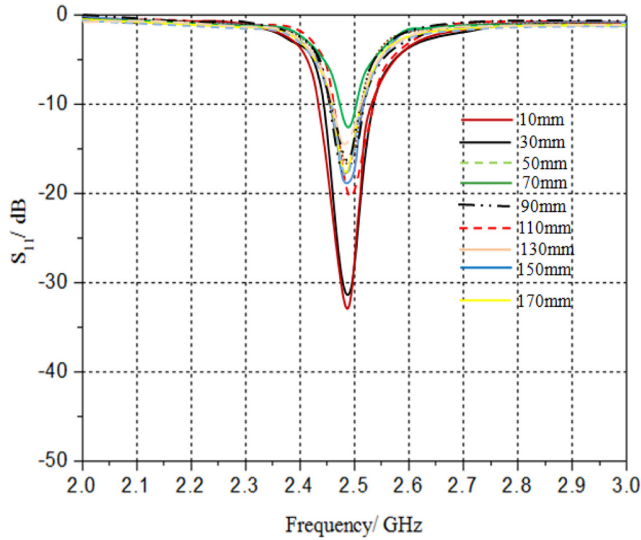
Fig. 9: Parametric-study based on the proposed EBG height in terms of $|S_{11}|$.

A further investigation included the effect of varying the EBG planner array on resonant frequencies behavior. It is observed from Fig. 10, that insignificant change in the $|S_{11}|$ spectrum with respect to the EBG planner array except when the EBG array has one unit cell above the patch antenna.
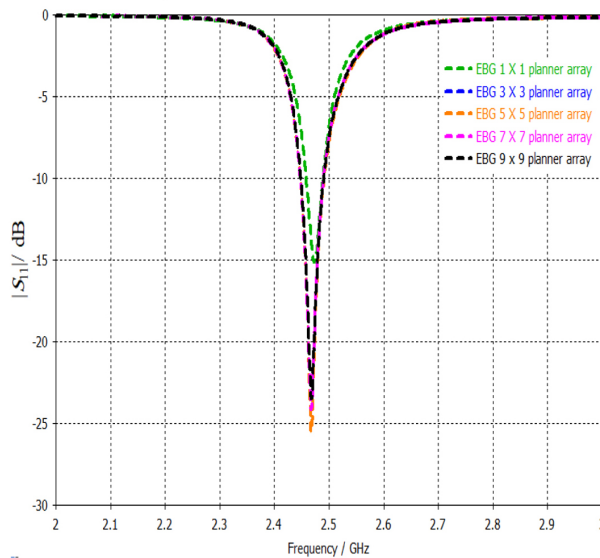
Fig. 10: Parametric-study based on the proposed EBG planner array in terms of $|S_{11}|$.

The boresight gain spectrum is evaluated using the two solvers in a frequency range from 2 GHz to 3 GHz as depicted in Fig. 11. From the obtained results in Fig. 11, the microstrip antenna without EBG layer exhibits an insignificant change in the antenna gain with respect to the gain spectrum that is presented by the antenna based EBG lens. Such difference is due to the high selectivity of the EBG structures for a particular frequency band as any frequency selective surface. Nevertheless, varying the distance between the patch antenna and the EBG lens shows a significant change in the antenna gain. This is due to the fact of focusing the electromagnetic radiation at the numerical aperture of the lens relative to the electromagnetic aperture of the antenna as presented in [8]. Therefore, a numerical optimization process is invoked to validate the obtained results from the proposed algorithm in [8].
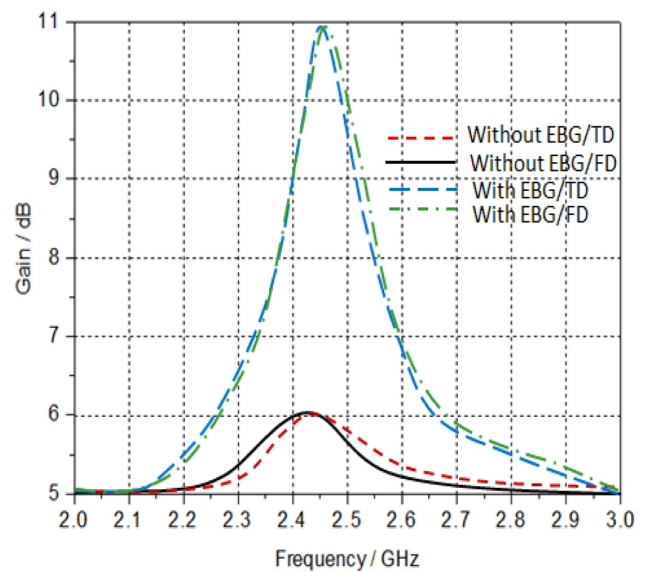
Fig. 11: Antenna boresight gain with and without EBG lens versus frequency.

The resonant frequency, $|S_{11}|$ spectra, gain, and bandwidth are given in Table II. It is found that the number of the EBG has a significant effect on the $|S_{11}|$ spectra, bandwidth and the gain.

TABLE II ANTENNA GAIN VERSUS THE NUMBER OF EBG PLANNER ARRAY

Number of EBG planner array	Resonant Frequency (GHz)	S_{11} Magnitude (dB)	B.W (MHz)	Gain (dBi)
1 X 1	2.47	-15.2	31	6.4
3 X 3	2.467	-16.8	33	10.4
5 X 5	2.465	-29.6	43.2	11.1
7 X 7	2.462	-24.1	42.1	11.9
9 X 9	2.468	-23.5	42	12

Next, the antenna 3D radiation patterns are evaluated with changing the EBG planner array as 1×1, 3×3, 5×5, 7×7, and 9×9 respectively. As seen in Fig. 12, the evaluated 3D radiation patterns are presented.
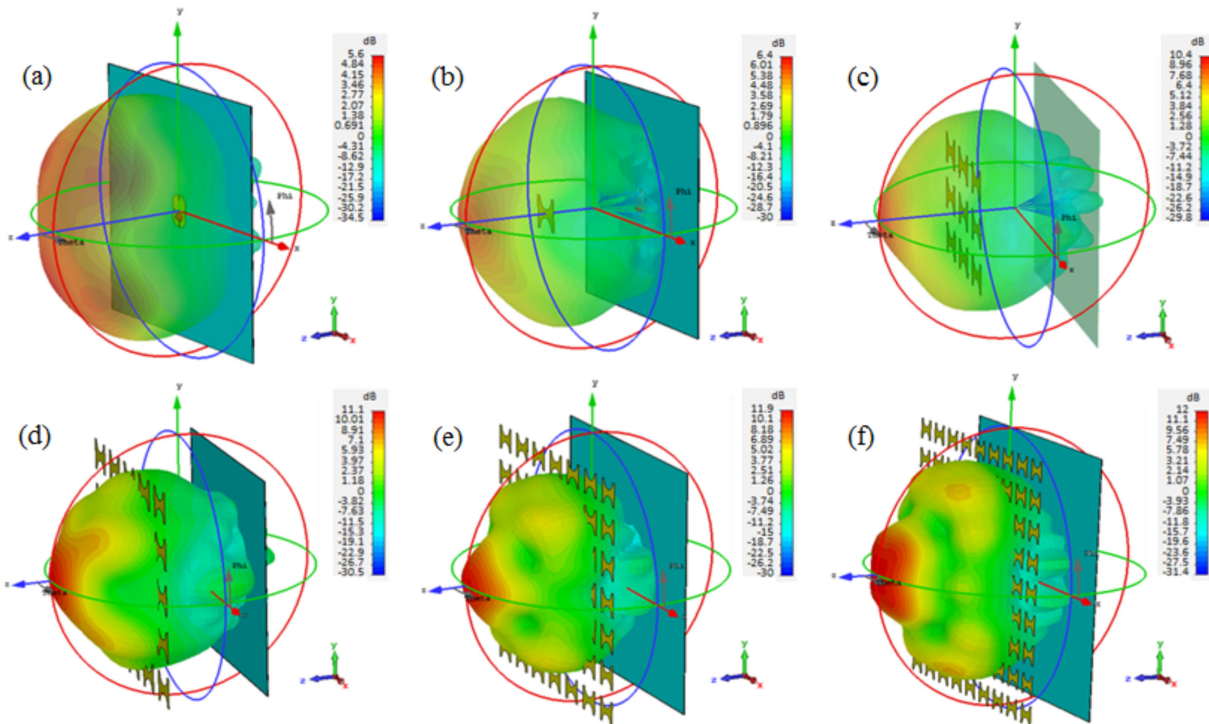
Fig. 12: Comparison of the 3-radiation patterns with and without EBG at 2.45 GHz ;
(a) patch only (b)1x1 (c) 3x3 (d) 5x5 (e) 7x7 (f) 9x9 EBG planer array respectively.

The antenna substrate area dimensions, length and width, are changed from $120{\times}120mm^2$ to $240{\times}240mm^2$ with a step of $40{\times}40mm^2$. The other antenna dimensions are fixed. It is found that the proposed antenna $|S_{11}|$ spectra are affected significantly as seen in Fig. 13(a). However, the antenna gain is significantly affected as presented in Fig. 13(b).
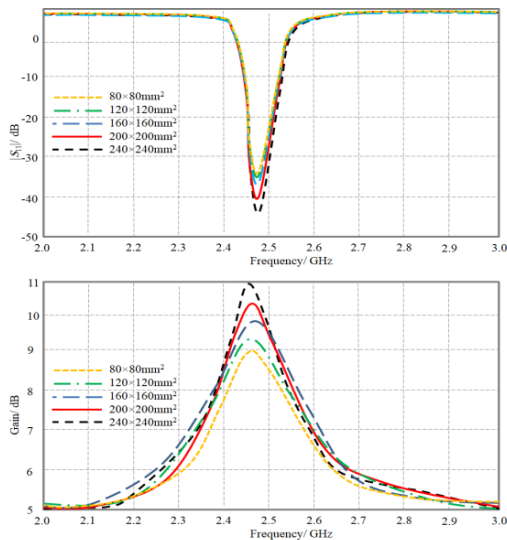
Fig. 13: Parametric study simulation results; (a) $|S_{11}|$ spectra and (b) Antenna boresight gain.

The optimal antennae design performances are evaluated using HFSS software package for further validation [24] based Finite Element Method (FEM). The antenna performances in terms of $|S_{11}|$ and radiation patterns are presented in Fig. 14. The obtained results reveal excellent agreements.
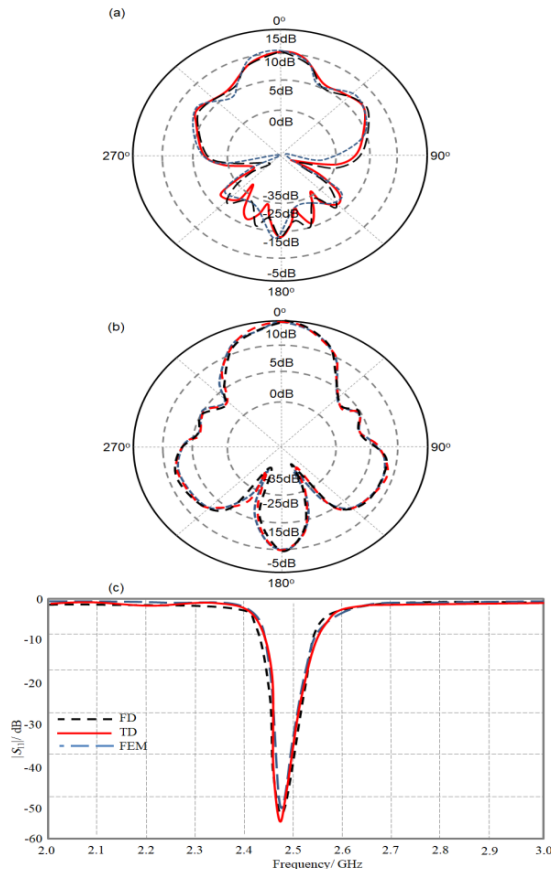
Fig. 14: Antenna performance comparison between three different techniques; (a) radiation patterns at. θ- 0o, (b) radiation patterns at ϕ =0o, and (c) $|S_{11}|$ spectra.

In the proposed simulation processes, the number of conducted mesh cells is N_x=280, N_y=225, and N_z=75 along the x-, y-, and z-axes, respectively. The required time step is 3.7×10^{24}ns. However, the HFSS mesh to reach the convergence is found 4.5×10^5 tetrahedral.

The achieved antenna enhancement is attributed to the fact of the summation of the emerging fields from the EBG unit cells according to the following equation:

$$g_{total}(x,y,z) = \prod_{S=1}^{S_o} h_S F_{SL}(v_x, v_y) \qquad (3)$$

where, gtotal is the total gain, hs is the antenna gain, and FSL is the unit cell geometrical function to be derived as in [8]. S is the central unit cell and So is the maximum number of the unit cells.

The ray tracing is presented in Fig. 15 to describe the antenna beam radiation diffraction from the proposed EBG structure. It shows that the proposed EBG focuses the radiation in the paraxial beam direction.
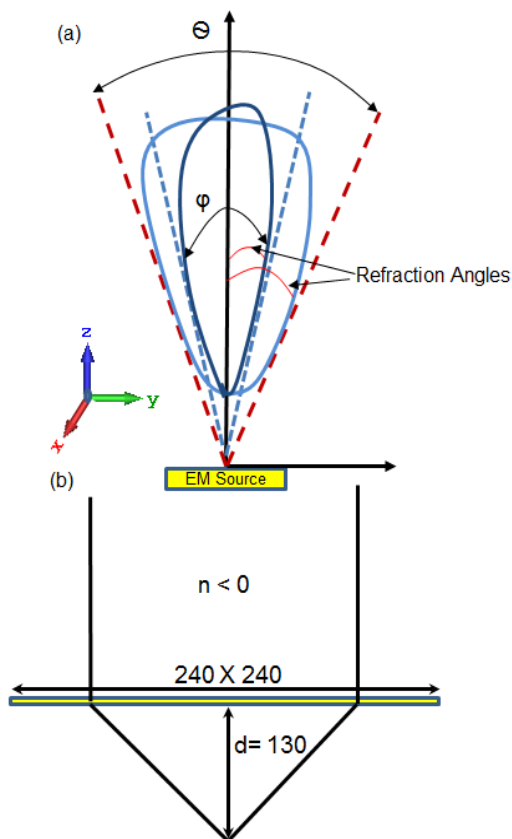
Fig. 15: Ray tracing (a) Angles of the incident and refracted electromagnetic radiation rays and (b) Paraxial electromagnetic beam ray modified by a zero refractive index lens.

IV. CONCLUSON

In this paper, a novel EBG geometry of a single layer positioned over a traditional microstrip antenna of a square patch is investigated for different wireless applications. In this design, the proposed antenna gain is improved from 5.6 dBi up to 11.1 dBi at 2.45 GHz with an F/B exceeds the 22 dB. It is found that the proposed EBG lens shows high improvement selectivity around 2.45 GHz up to 2.55 GHz by providing a bore-sight gain over 11.1 dBi to fit the narrow bandwidth wireless communication systems. Insignificant degradation in the radiation efficiency is taken place after introducing the proposed EBG lens due to the conductor losses. A numerical validation is obtained by using both TD and FD solves of CST MWS formulations to end up with an excellent agreement between the results the two solvers.

REFERENCES

[1] E. Yablonovitch, "Inhibited spontaneous emission in solid-state physics and electronics," Phy. Rev. Lett., vol. 58, pp. 2059-2062, 1987.
[2] S. John, "Strong localization of photons in certain disordered dielectric superlattices," Phy. Rev. Lett., vol. 58, pp. 2486-2489, 1987.
[3] T. A. Elwi, H. M. Al-Rizzo, Y. Al-Naiemy, and H. R. Khaleel, "Miniaturized microstrip antenna array with ultra mutual coupling reduction for wearable MIMO systems," 2011 IEEE International Symposium on Antennas and Propagation, July 2011.
[4] T. A. Elwi, M. M. Hamed, Z. Abbas, and M. A. Elwi, "On the Performance of the 2D Planar Metamaterial Structure", International Journal of Electronics and Communications, volume 68, Issue 9, pp. 846–850, September 2014.
[5] Z. Zhang and S. Satpathy, "Electromagnetic wave propagation in periodic structures: Bloch wave solution of Maxell's equations," Phy. Rev. Lett., vol. 65, pp. 2650-2653, 1990.
[6] K. M. Leung and Y. F. Liu, "Full vector wave calculation of photonic band structures in faced-centered-cubic dielectric media," Phy. Rev. Lett., vol. 65, pp. 2646-2649, 1990.
[7] T. A. Elwi "A further investigation on the performance of the broadside coupled rectangular split ring resonators," Progress In Electromagnetics Research Letters, volume 34, pp.1-8, August 2012.
[8] T. A. Elwi, H. M. Al-Rizzo, N. Bouaynaya, M. M. Hammood, and Y. Al-Naiemy, "Theory of gain enhancement of UC–PBG antenna structures without invoking Maxwell's equations: an array signal processing approach," Progress In Electromagnetics Research B, volume 34, pp. 15-30, August 2011.
[9] T. A. Elwi, H. M. Al-Rizzo, D. G. Rucker, F. Song, "Numerical simulation of a UC–PBG lens for gain enhancement of microstrip antennas," International Journal of RF and Microwave Computer-Aided Engineering, volume 19, issue 6, pp. 676–684, November 2009.
[10] T. A. Elwi, "A Slotted Lotus Shaped Microstrip Antenna based an EBG Structure", Journal of Material Sciences and Engineering, Vol. 7, issue 2, no. 439, pp. 1-15, March 2018.

[11] T. A. Elwi, A. I. Imran, and Y. Alnaiemy, "A Miniaturized Lotus Shaped Microstrip Antenna Loaded with EBG Structures for High Gain-Bandwidth Product Applications", Progress In Electromagnetics Research C, volume 60, pp. 157-167, December 2015.

[12] A. I. Imran and T. A. Elwi, "A Cylindrical Wideband Slotted Patch Antenna Loaded with Frequency Selective Surface for MRI Applications" Engineering Science and Technology, an International Journal, volume 20, issue 3, pp. 990–996, April 2017.

[13] T. A. Elwi, "A Miniaturized Folded Antenna Array for MIMO Applications", Wireless Personal Communications, in press, August 2017.

[14] T. A. Elwi, "Electromagnetic Band Gap Structures based an Ultra Wideband Microstrip Antenna", Microwave and Optical Letters, volume 59, issue 4, pp. 827-834, February 2017.

[15] T. A. Elwi, "Toward Plasmonic UC-PBG Structures based SWCNTs for Optoelectronics Applications", Diyala Journal for Pure Science, January 2018.

[16] T. A. Elwi and B. A. Ahmad, "A fractal metamaterial based printed dipoles on a nickel oxide polymer palm fiber substrate for Wi-Fi applications," AEU-International Journal of Electronics and Communications, vol. 96, pp. 122-129, Sep. 2018.

[17] T. A. Elwi, "Metamaterial based a Printed Monopole Antenna for Sensing Applications," International Journal of RF and Microwave Computer-Aided Engineering, volume 28, issue 7, pp. 1-10, Sep. 2018.

[18] T. A. Elwi, Z Abbas, M Noori, Y Al-Naiemy, EY Salih, MM Hamed, "Conformal antenna array for MIMO applications," Journal of Electromagnetic Analysis and Applications volume 6, issue 04, number 43, May 2014.

[19] T. A. Elwi, M. A. S. Al-Frieh, M. Bawi, "No Frequency Reuse: Wearable Steerable MIMO Microstrip Antenna Array for Mobile Ad Hoc Applications," British Journal of Applied Science & Technology, volume 4, issue 17, pp. 2477-2488, June 2014.

[20] Y. Al-Naiemy, T. A. Elwi, and N. Lajos, " Enhancing the Microstrip Antenna Gain Using a Novel EBG Lens Based on a Single Layer" 11th International Symposium on Communication Systems, Networks & Digital Signal Processing (CSNDSP), page (1-4) 27 September 2018.

[21] A. Bhutani, B. Göttel, D. Müller, and T. Zwick "Novel planar electromagnetic bandgap for mutual coupling reduction between patch antennas" 2015 German Microwave Conference page (1-4), 14 May 2015.

[22] CST Microwave Studio, http://www.cst.com.

[23] C. A. Balanis, "Antenna Theory: Analysis and Design," Wiley, John & Sons, Inc., NA, USA, Sep. 2008.

[24] HFSS, http://www.hfss.com.

Yahiea Alnaiemy was born in Iraq in 1971, in 1990; he was enrolled at the Higher Institution of Telecommunications and Post before transferring to Al-Mustansiriyah University/College of Engineering-Electrical Engineering Department in 1994. In July of 1998 he received a Bachelor's a Degree in Electrical Engineering. He continued his graduate studies by joining the Iraqi Commission for Computers and Informatics where he received a Higher Diploma in Information Systems in 2001. He enrolled at Diyala University as an instructor in communication Engineering, electrical power, computer and physics departments. In 2009 he was granted a scholarship to complete his master degree in electrical engineering at the University of Arkansas at Little Rock, USA. He got his MSc in Wireless Communications from UALR, USA, in 2012. While completing his graduate degree, his research effort has been in the area of antennas and microwave material characterization. In 2017 he was granted a scholarship to complete his Ph.D. in electrical engineering at Budapest University of Technology and Economics (BME), Hungary, His current research areas include UWB antennas, EBG structures, metamaterial, GPS, implantable wireless systems, and nanoscale microwave devices. He is one of the Member of IEEE and reviewer in PIER Journals since 2012.

Taha A. Elwi He received his B.Sc. in Electrical Engineering Department (2003), Postgraduate M.Sc. in Laser and Optoelectronics Engineering Department (2005) from Nahrain University Baghdad, Iraq. On January, 2008, he joined the University of Arkansas at Little Rock and he obtained his Ph.D. in December 2011 from the system engineering and science. His research areas include wearable and implantable antennas for biomedical wireless systems, smart antennas, Wi-Fi deployment, electromagnetic wave scattering by complex objects, design, modeling and testing of metamaterial structures for microwave applications, design and analysis of microstrip antennas for mobile radio systems, precipitation effects on terrestrial and satellite frequency re-use communication systems, effects of the complex media on electromagnetic propagation and GPS. The Nano-scale structures in the entire electromagnetic spectrum are a part of his research interest.

Lajos Nagy He received the Engineer option Communication) and PhD degrees, both from the Budapest University of Technology and economics (BME), Budapest, Hungary, in 1986 and 1995, respectively. He joined the department of Microwave Telecommunications (now Broadband Infocommunications and Electromagnetic Theory) in 1986, where he is currently an associate professor. He has been the head of department of Broadband Infocommunications and Electromagnetic Theory in 2007. He is a lecturer on graduate and postgraduate courses at BME on Antennas and radiowave propagation, Radio system design, Adaptive antenna systems and Computer Programming. His research interests include antenna analysis and computer aided design, electromagnetic theory, radiowave propagation, communication electronics, signal processing and digital antenna array beamforming, topics where he has produced more than 100 different book chapters and peer-reviewed journal and conference papers. Member of Hungarian Telecommunication Association, official Hungarian Member and Hungarian Committee Secretary of URSI, Chair of the IEEE Chapter AP/ComSoc/ED/MTT.

A Systematic Analysis and Design of a High Gain
Microstrip Antenna based on a Single EBG Layer

Thomas Zwick (S'95-M'00-SM'06) received the Dipl.-Ing. (M.S.E.E) and Dr.- Ing. (Ph.D.E.E) degrees from the Karlsruhe Institute of Technology (KIT), Karlsruhe, Germany, in 1994 and 1999, respectively. From 1994 to 2001, he was a Research Assistant with the Institut für Höchstfrequenztechnik und Elektronik (IHE), Universität Karlsruhe (TH), Karlsruhe, Germany. In February 2001, he joined IBM as Research Staff Member with the IBM T. J. Watson Research Center, Yorktown Heights, NY, USA. From October 2004 to September 2007, he was with Siemens AG, Lindau, Germany. During this period, he managed the RF development team for automotive radars. In October 2007, he became a Full Professor with the Karlsruhe Institute of Technology (KIT), Karlsruhe, Germany. He is the Director of the Institute of Radio Frequency Engineering and Electronics (IHE), KIT. He has authored or co-authored over 300 technical papers. He holds 20 patents. His research topics include wave propagation, stochastic channel modeling, channel measurement techniques, material measurements, microwave techniques, millimeter wave antenna design, wireless communication and radar system design. Dr. Zwick was General Chair of the 2013 international Workshop on Antenna Technology (iWAT 2013), Karlsruhe, Germany, and of the 2015 IEEE MTT-S International Conference on Microwaves for Intelligent Mobility (ICMIM), Heidelberg, Germany. He also was the Technical Program Committee (TPC) Chair of the European Microwave Conference (EuMC) in 2013. From 2008 to 2015, he was the President of the Institute for Microwaves and Antennas (IMA). He was an IEEE Distinguished Microwave Lecturer from 2013 to 2015 with his lecture on "QFN Based Packaging Concepts for Millimeter-Wave Transceivers." He served on the TPC of several scientific conferences. His research team was the recipient of over ten Best Paper Awards of international conferences.

Overcoming the Realization Problems
of Wideband Matching Circuits

Balázs Matolcsy and Attila Zólomy

Abstract—**During the analytical design process of wideband impedance matching major problems may arise, that might lead to non-realizable matching networks, preventing the successful impedance matching. In this paper two practical design rules and a simplified equation is presented, supporting the design of physically realizable impedance matching networks. The design rules and calculation technique introduced by this paper is summarized, and validated by microwave circuit simulation examples.**

Index Terms—**physical matching limits, wideband impedance matching, realizable matching networks**

I. Introduction

Analytical wideband impedance matching techniques have been thoroughly discussed in previous many studies [1], but most of these only focus on the theoretical limits of the matching techniques, by issuing an infinite number of passive L-C elements for the matching circuit [2]. Several approaches have been shown to be successful for matching complex impedances [3] [4], but hardly any of them discuss the physical realization problems, and practical limitations of the finite length matching networks [5] [6]. Due to the high calculation complexity, of the wideband matching networks, mostly only third-order matching networks are used due to practical reasons (higher order matching networks have various problems, such as weak parameter tolerance margins, inhibiting manufacturing processes), thus this paper only discusses third-order lossless matching networks.

This paper presents two of the practical realization limits of the analytical wideband complex impedance matching technique, presented by R. M. Fano [1], and H. W. Bode [2]. Utilising the proposed limitation factors, and simplified calculations presented in this paper, matching optimization goals are easier to define, and a wide range of practically unrealizable solutions are excluded before the complex calculation process. The rest of this paper is organized as follows: first the Bode-Fano matching technique is presented in detail followed by the practical parameter restrictions in Section IV. and Section V. Later on in Section VI. the modified matching algorithm and a simplified caluclation for a certain matching parameter is introduced as well. Finally the proposed design rules are validated by two simulation examples in Section VIII.

II. Analytical matching technique (Bode-Fano)

The analytical wideband complex impedance matching methods are based on the Darlington-theorem, which states, that a complex load can be substituted, with a passive reactant network that is terminated in a unity value resistance [7]. This principle allows that the complex wideband impedance matching task can be redefined as a double-terminated filter synthesis problem. In most situations complex impedances are matched (on the largest possible bandwidth) to a purely real valued generator impedance, thus the matching network's purpose is to completely cancel out the imaginary part of the load impedance, and match the remaining real part to the generator at the same time. Well-known examples for analytical matching methods are: Bode-Fano matching [2], and Youla's matching technique based on complex normalization [11]. In this paper an in-depth analysis is presented discussing the Bode-Fano method for complex terminations, matched to purely real 50 Ω source impedance.

Within the design equations lies a problem which partially inhibits the realization of matching networks, at certain initial parameters. Furthermore the upper, and lower matched frequency should be very carefully chosen, otherwise analytical matching can result in matching networks that are physically unrealizable. In the following section the detailed equations and restrictions are presented for realizable matching networks (where matching networks are constructed from shorted quarter wavelength stubs, that can only represent purely real valued impedances). Shortly thereafter, the physical design limitations are taken into consideration during the calculations, highly restricting the range of complex impedances where the Bode-Fano analytical method provides adequate matching. Obeying these design rules during the design process may help designing load impedances (where allowed), at which the Bode-Fano method results in acceptable matching (e.g. where $|S_{11}|$ is less than -10 dB).

III. The analytical matching process

An important aspect of the Bode-Fano matching method is that it can only be used for terminations where the impedance-frequency dependency resembles a single-reactance load's impedance or admittance. Thereby the load shall be substituted with a well chosen single-reactance circuit model, i.e. a series or parallel R-C, R-L impedance. Substitution model validation methods are omitted here. All matching results will be compared to the ideal infinite matching networks limits, discussed

for single-reactance models by Bode and Fano in [1]. The problems that may arise during the matching process is shown through a practical example. The goal is to match a series R-L impedance to a purely real 50 Ω generator impedance. First, the series capacitance (C_{series}) should be calculated through which the series R-L can be turned into a resonant R-L-C structure. (for parallel terminations, parallel resonance may be required, and design equations are slightly different)

$$C_{\text{series}} = \frac{1}{4\pi^2 f_c^2 L}, \tag{1}$$

where f_c represents the center frequency of the desired matched band. The quality factor (Q) for this R-L-C structure is defined as

$$Q = \frac{2\pi f_c L}{R}. \tag{2}$$

The theoretical matching quality limit can be calculated using the decrement factor,

$$\delta = \frac{1}{Q} \frac{\sqrt{4\pi^2 f_h f_l}}{2\pi(f_h - f_l)}, \tag{3}$$

where f_h is the upper, and f_l is the lower frequency limit. Using the decrement factor and the minimum of the maximal reflection coefficient on the desired bandwidth is expressed as

$$\Gamma_{\text{max}} = 20\log_{10}\left(e^{-\pi\delta}\right), \tag{4}$$

where Γ_{max} stands for the best available reflection coefficient in case of an ideal matching network consisting of an infinite number of L-C ladder components. This limit is also known as the Bode matching limit. This parameter is used for the comparison of theoretical and the finite third-order matching quality. In order to point out the critical parameters during the matching process, the detailed process of the single reactance matching example is presented. The following equations will lead to the solution of the low pass filter prototype, for the matching circuit,

$$d = \sinh\frac{\sinh^{-1}\sqrt{\frac{1}{10^{(r/10)-1}}}}{n}, \tag{5}$$

$$D = \frac{d}{\delta\sin\left(\frac{\pi}{2n}\right)} - 1, \tag{6}$$

where n represents the order of the matching circuit, and r stands for the maximal allowed Chebyshev ripple factor in the matched frequency band. Later on in Section VII., a simplified parameter calculation method is presented for d. These parameters are used for evaluating the coupling coefficients for the low pass filter prototype network, provided by Green's equations [10]:

$$k_{1,2} = \sqrt{\frac{3}{8}\left(1 + \left(1 + \frac{D^2}{3}\right)\delta^2\right)}, \tag{7}$$

$$k_{2,3} = \sqrt{\frac{3}{8}\left(1 + \left(\frac{1}{3} + D^2\right)\delta^2\right)}. \tag{8}$$

Based on [8] and [10], the low pass filter prototype component values for the double-terminated filter are

$$g_0 = 1, \tag{9}$$

$$g_1 = \frac{1}{\delta}, \tag{10}$$

$$g_2 = \frac{1}{g_1 \cdot k_{1,2}^2}, \tag{11}$$

$$g_3 = \frac{1}{g_2 \cdot k_{2,3}^2}, \tag{12}$$

$$g_4 = \frac{1}{D \cdot \delta \cdot g_3}. \tag{13}$$

As seen in (9), the generator impedance (R_g) is determined as the synthesis result. This overrides the original generator impedance (50 Ω), which is unacceptable. Furthermore this is a low-pass filter prototype circuit, hence filter transformation steps are required for a passband configuration. For overcoming these synthesis problems, admittance inverters are used. The auxilary parameters used for defining the admittance inverter's parameters are

$$d_p \approx 1, \tag{14}$$

$$\omega_m = \frac{(f_h - f_l)}{f_c}, \tag{15}$$

$$\Theta_1 = \frac{\pi}{2}\left(1 - \frac{\omega_m}{2}\right) \tag{16}$$

and the admittance inverter parameters are calculated using equations in [10] and [9]:

$$C_2 = g_2, \tag{17}$$

$$C_3 = g_0 g_3 g_4 \frac{R_L}{R_g}, \tag{18}$$

$$C_2' = g_2(1 - d_p), \tag{19}$$

$$C_2'' = d_p g_2, \tag{20}$$

$$C_3' = C_2'', \tag{21}$$

$$C_3'' = C_3 - C_3', \tag{22}$$

$$J_{2,3} = \frac{1}{R_L}\sqrt{\frac{C_2 C_3}{g_2 g_3}}, \tag{23}$$

$$N_{2,3} = \sqrt{(J_{2,3} R_L)^2 + \left(\frac{C_2'' \tan(\Theta_1)}{g_0}\right)^2}. \tag{24}$$

The construction of the matching network is based on quarter wavelength (at the center frequency), shorted stubs. The shorted stubs only have a single free parameter in this case: transmission line admittance (or impedance). These admittance values are obtained by the following equations:

$$Y_2 = \frac{1}{g_0 R_L}C_2' \tan(\Theta_1) + \frac{1}{R_L}(N_{2,3} - J_{2,3} R_L), \tag{25}$$

$$Y_3 = \frac{1}{g_0 R_L}C_3'' \tan(\Theta_1) + \frac{1}{R_L}(N_{2,3} - J_{2,3} R_L), \tag{26}$$
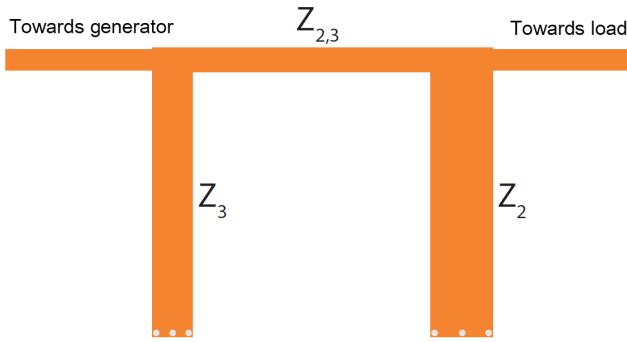
$$Y_{2,3} = J_{2,3}. \tag{27}$$

Fig. 1. Third order matching network with $\lambda/4$ shorted stubs.

The impedance values are the reciprocal, of the given admittances respectively ($Z_2, Z_3, Z_{2,3}$). The third-order matching network structure is shown in Fig. 1. However, this method does not always provide purely real transmission line impedance values. In several cases, if the input parameters are not well chosen the equations may lead to complex transmission line immittances. Complex transmission lines are not realizable with lossless components. For effective impedance matching, only lossless circuit elements are allowed (with purely real impedance values), otherwise the required power would not reach the load, but dissipate in the lossy elements. In the following section mandatory parameter restriction is presented, used for avoiding these unwanted complex transmission line impedances.

IV. AVOIDING COMPLEX TRANSMISSION LINE IMPEDANCES

Matching network transmission line impedances are expressed as the reciprocal of the admittance values. As known from linear network theory, these impedance values can be solely purely real (assuming lossless transmission lines). However there are multiple cases where the results are complex impedance values. Complex impedance value may arise first during the design if

$$\operatorname{Im}\left(J_{2,3}\right) \neq 0. \tag{28}$$

It is also worth mentioning that $J_{2,3}$ can be purely real, or pure imaginary due to the nature of the square root function, in (24). In order to avoid the pure imaginary impedance value it is necessary to point out which parameter values affect this. If

$$\frac{C_2 C_3}{g_2 g_3} < 0, \tag{29}$$

then $J_{2,3}$ is pure imaginary. As the parameters are multiplied together, an odd number of negative coefficients in the expression can result in a value less than zero. Due to the fact that the decrement δ, and Green-coefficients $k_{1,2}$ and $k_{2,3}$ are always greater than or equal to zero, g_0, g_1, and g_2 can only be positive. Thus a negative value in Eq. (29) can solely occur

if $C_3 < 0$, leading to $g_4 < 0$. The g_4 parameter is negative if, $D < 0$, resulting

$$D < 0 \quad \text{iff.} \quad \frac{d}{\delta \sin\left(\frac{\pi}{2n}\right)} < 1, \tag{30}$$

assuming that $n = 3$ (third-order matching network) and $\delta > 0$:

$$\operatorname{Im}\left(J_{2,3}\right) = 0 \quad \text{iff.} \quad 2d > \delta. \tag{31}$$

In order to avoid complex transmission line impedance values, the mandatory rule is to set,

$$d > \frac{\delta}{2}. \tag{32}$$

On one hand the d parameter can be set by modifying r, which stands for the amount of allowed Chebyshev-ripple in the matched frequency band, on the other hand the decrement factor (δ) is pre-determined by the quality factor, and the frequency band. If the matching task allows the modification of either r, or f_l or f_h, this mandatory rule can be satisfied (in some cases), as shown later in Section VIII-B.

V. PHYSICAL TRANSMISSION LINE IMPEDANCE LIMITATIONS

As most of the matching circuit designs are based on microstrip transmission lines, one should always avoid extreme line impedances. As a basic rule e.g. on a printed circuit board, transmission line impedances should be $15\,\Omega \leq Z \leq 150\,\Omega$. This is due to the copper structure manufacturing tolerance limits. The matching network realization fails, if any of these transmission line impedances do not obey this rule. As an example let's assume a purely real $Z_{2,3}$ that satisfies the rule

$$15\,\Omega < R_{\mathrm{L}} \sqrt{\frac{g_2\, g_3}{C_2\, C_3}} < 150\,\Omega. \tag{33}$$

Substituting into this expression,

$$R_{\mathrm{L}} \sqrt{\frac{g_2\, g_3}{C_2\, C_3}} = R_{\mathrm{L}} \sqrt{\frac{D\, R_{\mathrm{g}}\, k_{1,2}^2}{R_{\mathrm{L}}\, k_{2,3}^2}}, \tag{34}$$

where R_{L} is the real part of the load impedance, and R_{g} is the generator impedance. If the condition,

$$15\,\Omega < R_{\mathrm{L}} \sqrt{\frac{D\, R_{\mathrm{g}}\, k_{1,2}^2}{R_{\mathrm{L}}\, k_{2,3}^2}} < 150\,\Omega, \tag{35}$$

does not apply, the matching network is not realizable, due to the aforementioned physical limits. This short expression requires only five parameters, and can be used to exclude non-realizable matching networks at an early phase of the network design. The same limit calculation can be applied to Z_2 and Z_3, however the expression is more complex, and irrelevant, considering the fact, that if at least one of the transmission line impedances is not realizable, the matching network is non-realizable as well.

Algorithm 1 Modified matching algorithm

task → initial parameters(R_L, R_g, L, f_c, b, r)
while $|S_{11}| > -10\,\text{dB}$ **do**
    calculate d and δ parameters
    if $2\,d > \delta$ **then**
        non-complex matching network
        calculate $D, k_{1,2}, k_{2,3}$
        if $15\,\Omega < R_L \sqrt{\dfrac{D\,R_g\,k_{1,2}^2}{R_L\,k_{2,3}^2}} < 150\,\Omega$ **then**
            physically realizable, non-complex network
            calculate network impedances ($Z_2, Z_3, Z_{2,3}$)
            recalculate $|S_{11}|$
        else
            physical realization problem, modify r or b
        end if
    else
        if $2\,d < \delta$ **then**
            complex matching network, modify r or b
        end if
    end if
end while
successful matching is achieved

VI. ALGORITHMIC IMPLEMENTATION OF THE MODIFIED MATCHING METHOD

A modified matching algorithm (Algorithm 1) is defined herein for avoiding the non-realizable matching network solutions, by using the rules given in previous sections. As it can be seen in Algorithm 1, the matching network impedances should only be calculated, if both physical limitations are satisfied. The complexity of these calculations can be further reduced, if the calculation of parameters d and δ is faster. The aim of the upcoming section is to show a possible faster approximate expression to calculate the required parameter d from r, thus speeding up the iteration process.

VII. SIMPLIFIED CALCULATION OF THE d PARAMETER

The exact calculation of the parameters d and D for Green's coupling coefficients were shown in Section III. As the hyperbolic, and the inverse hyperbolic functions may be difficult to evaluate, this paper will introduce a simplified approximate expression for the parameter d. As

$$\sinh x = \frac{e^x - e^{-x}}{2}, \tag{36}$$

$$\sinh^{-1} x = \ln\left(x + \sqrt{x^2 + 1}\right), \tag{37}$$

these expressions can be used to transform hyperbolic equations to their exponential and logarithmic forms. By substituting

$$u = \sqrt{\frac{1}{10^{(r/10)} - 1}},$$

the parameter d can be rewritten in the form:

$$d = \frac{1}{2}\left(e^{\ln\left(u+\sqrt{u^2+1}\right)^{\frac{1}{3}}} - e^{\ln\left(u+\sqrt{u^2+1}\right)^{-\frac{1}{3}}}\right) =$$

$$= \frac{1}{2}\left(\sqrt[3]{u + \sqrt{u^2+1}}\right) - \frac{1}{2}\left(\sqrt[3]{u + \sqrt{u^2+1}}\right)^{-1}.$$
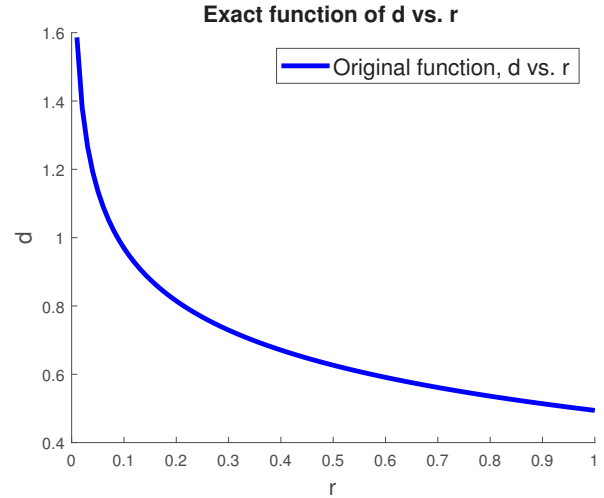
Fig. 2. The original function of d vs. r
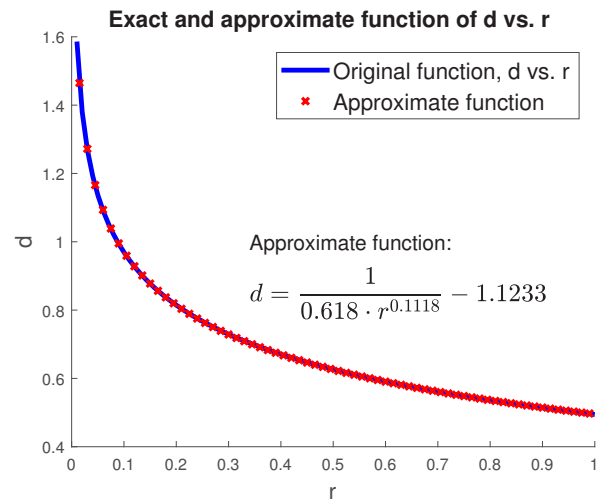
Fig. 3. The original and the approximate function of d vs. r

As can be seen from Fig. 2, if d vs. r is plot in the Cartesian coordinate-system, the function resembles a monotonic decending hyperbolic function. These embedded square, and third-root functions are computationally extensive, thus an acceptable approximate function is proposed. The approximation (i.e the curve fitting task) was carried out in MATLAB 2017b. As mentioned before the proposed initial function is a custom hyperbolic function which has the symbolic form

$$\hat{d}(r) = \frac{1}{a \cdot r^b} + c,$$

where a, b, c are arbitrary constants. Utilizing the Least-Square Method based curve fitting, these constants were determined

$$a = 0.618, \quad b = 0.1118, \quad c = -1.1233.$$

Based on these constants, the approximate function for d is

$$\hat{d}(r) = \frac{1}{0.618 \cdot r^{0.1118}} - 1.1233. \tag{38}$$

This approximate and the original exact function is presented in Fig. 3. The curve-fitting approximation exhibited acceptable results, with an RMSE (Root Mean Squared Error) value of $8.86 \cdot 10^{-4}$, and R-square factor of 1.00. On this basis it can be safely stated that

$$d \approx \frac{1}{0.618 \cdot r^{0.1118}} - 1.1233. \tag{39}$$

During the iterative solution to the best matching network, in Algorithm 1 the parameter d should be reevaluated as soon as r changes. This evaluation occurs everytime the algorithm runs into an unrealizable matching solution. With this new hyperbolic formula introduced here in Eq. (39), the resulting algorithm exhibits a reduced processing time.

VIII. MATCHING EXAMPLES (SIMULATIONS)

In this section two matching examples are introduced. One where the $2\,d > \delta$ condition is initially satisfied, and another where it is not. These simulation setups were created in *AWR Microwave Design Studio 2010*. The simulated impedance matching networks are designed for matching series R-L loads to a $R_g = 50\,\Omega$ generator, on a specific European ISM UHF frequency band, i.e. 868 MHz.

A. Impedance matching example 1.

The impedance matching example parameters are shown in Table I,

TABLE I
IMPEDANCE MATCHING EXAMPLE 1. - INITIAL PARAMETERS

f_c	b	R_g	R_L	L	r	δ	d
868 MHz	25%	50 Ω	30 Ω	20 nH	0.066	**0.5366**	**1.068**

where values in bold, are parameters calculated from the six initial parameters: center frequency, relative matching bandwidth, generator source impedance, load resistance, load inductor value, and maximal Chebyshev-ripple factor respectively. Regarding the values in Table I, the fundamental rule for non-complex transmission line impedances (presented in Section IV.) and the practical impedance realization limit are both satisfied (see Eq. (35)).

The matching network consists of the following transmission line impedances, and series capacitance.

Fig. 4 presents the input reflection coefficient as a function of frequency, for the matching network. As it is highlighted with the markers, an acceptable matching ($|S_{11}| \leq -10\,\text{dB}$) is reached on the $738\ldots1116\,\text{MHz}$ frequency band. The physical line impedance realization limit is satisfied as well,

$$15\,\Omega < 50\,\sqrt{1.153} < 150\,\Omega.$$
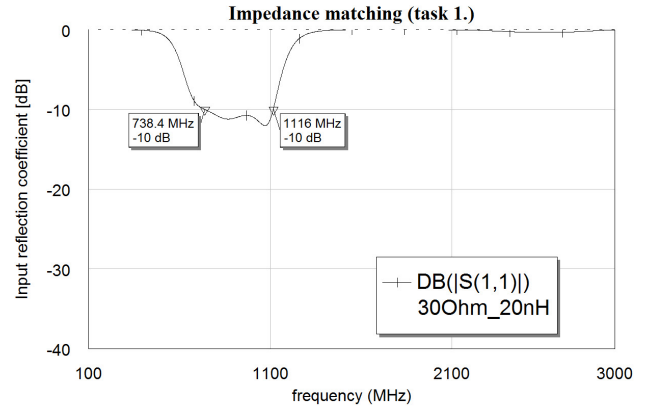
Fig. 4. Wideband matching result, for example 1.

TABLE II
MATCHING NETWORK COMPONENT PARAMETERS (EX. 1.)

$Z_{2,3}$	Z_2	Z_3	C_{series}
51.36 Ω	26.75 Ω	70.9 Ω	1.68 pF

As a conclusion, this example clearly states, that by abiding the rules introduced in Section IV. and Section V. one can avoid matching networks that are practically impossible to implement.

B. Impedance matching example 2.

In this example the initial parameters do **not** satisfy the fundamental realization rule (see Eq. (32)), therefore resulting in a non-realizable matching network. Overcoming this problem is presented hereby.

TABLE III
IMPEDANCE MATCHING TASK 2. - INITIAL PARAMETERS

f_c	b	R_g	R_L	L	r	δ	d
868 MHz	10%	50 Ω	50 Ω	20 nH	0.066	**2.281**	**1.068**

One might presume, that this matching task is easier, due to the smaller bandwidth, and higher real part of the load impedance, however the Bode-Fano method basically does not respect the realization rule shown in Section IV., hence the synthesis results in complex transmission line impedances.

TABLE IV
MATCHING NETWORK COMPONENT PARAMETERS (EX. 2.)

$Z_{2,3}$	Z_2	Z_3	C_{series}
$-18.86\,\text{j}\Omega$	$7.31 + 3.472\,\text{j}\Omega$	$-1.21 + 0.0668\,\text{j}\Omega$	1.68 pF

The solution for this problem is to either modify the matched relative bandwidth, or the Chebyshev-ripple factor, if allowed. This time, by setting $r = 0.0001$ the results have become acceptable (Fig. 5).

TABLE V
MODIFIED NETWORK PARAMETERS (EX. 2.)

$Z_{2,3}$	Z_2	Z_3	C_{series}
$53.17\,\Omega$	$27.18\,\Omega$	$104.1\,\Omega$	$1.68\,pF$

By modifying r, d is also modified ($d = 3.668$) and Eq. (32) is thereby satisfied, thus the matching task is solvable exclusively utilizing lossless components (impedance values are in Table V). The results in Fig. 5 show that the matching quality is better than expected, and the matched bandwidth is almost 50%, contrary to the predefined $b = 10\%$. This result is due to the outstandingly low, maximal Chebyshev-ripple factor, prescribed as the fix for avoiding complex impedances. As seen in this second matching example varying the Chebyshev-ripple factor has beneficiary effects on avoiding transmission line impedances. If the matching task allows, modifying the upper and lower frequency limits may have the same effect on avoiding unrealizable networks.
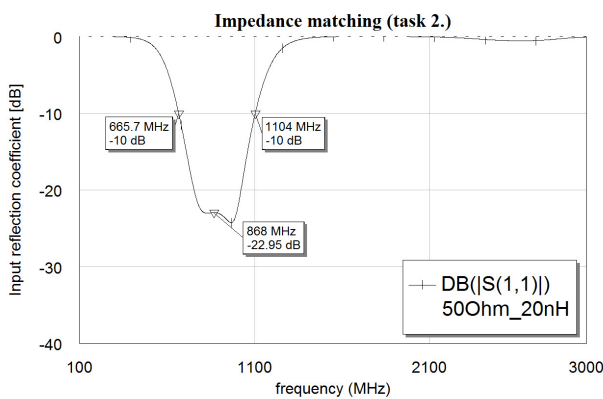
Fig. 5. Modifying r factor results in successful impedance matching and realizable network

CONCLUSION

The presented physical realization problems and solutions introduced in Section IV. and Section V. were successfully validated with simulation examples. The modified wideband matching algorithm was presented, and successfully applied for multiple matching tasks. If the realization limiting equations presented in this paper are satisfied, avoiding non-realizable matching networks becomes possible before complex calculations and optimalization steps were made. Furthermore the approximation for the parameter d reasonably reduces the calculation time at the iterative stage, thus speeding up the complete matching process.

ACKNOWLEDGMENT

REFERENCES

[1] R. M. Fano, "Theoretical limitations on the broadband matching of arbitrary impedances", J. Franklin Inst., Vol. 249, pp. 57-83, 1950.
[2] H. W. Bode, Network Analysis and Feedback Amplifier Design, Van Nostrand Reinhold Publishing Co., 1945.
[3] W. K. Chen, Broadband Matching Theory and Implementations, Third Edition, World Scientific Publishing Co. Ltd., 1993.
[4] W. K. Chen and C. Satyanarayana, "General theory of broadband matching", IEEE Proceedings Electronic Circuits and Systems, Vol. 129, No. 3, p. 96, 1982.
[5] Herbert J. Carlin, Pier Paolo Civalleri, Wideband Circuit Design, CRC Press, 1997.
[6] R. Kopru, C. Aydin, D. C. Atilla, C. Karakus and B. S. Yarman, "Wideband matching network design for a V-shaped square monopole antenna using Real Frequency Technique", 13th Mediterranean Microwave Symposium (MMS), 2013.
[7] Darlington S., "Synthesis of reactance 4-poles", Jour. Math. Phys., Vol. XVIII., pp. 275-353., September 1934.
[8] Cuthbert T. R., Circuit Design Using Personal Computers, NY: John Wiley Publishing Co., 1994.
[9] G. Matthaei, "Synthesis of Chebyshev Impedance-Matching Networks, Filters, and Interstages", IRE Transactions on Circuit Theory, Vol. 3, No. 3, pp. 163-172., 1956.
[10] G. Matthaei, L. Young, and E. M. T. Jones, Microwave Filters, Impedance Matching Networks, and Coupling Structures, NY: McGraw-Hill, 1980.
[11] Youla D. C, "A new theory of broadband matching", Defense Technical Information Center, pp. 30-50., 1964.

Balázs Matolcsy was born in Budapest, Hungary, in 1992. He received his B.Sc. and M.Sc. degree in Electrical Engineering at the Budapest University of Technology and Economics in 2015, and 2017 respectively. He joined the Department of Broadband Infocommunciation and Electromagnetic Theory in 2017 as a Ph.D. student. In 2018, he received a Short Term Research Scholarship from DAAD at the Technical University of Karlsruhe (KIT) in Germany. The main area of his research interests are high-frequency RF simulation, antenna design, visible light communication and mixed signal electronics.

Attila Zólomy received his M.Sc. and Ph.D. degrees in 1994 and 2004, respectively, from the Budapest University of Technology and Economics in Electrical Engineering. He works currently at the university as a part-time researcher. He also works as a senior member at Silicon Laboratories Ltd. in Hungary. His main interest are the microwave and millimeter wave circuits, small antennas, impedance matching, RF Integrated Circuits and module design in the UHF and 2.4 GHz frequency bands. He is author and co-author of more than 60 scientific papers and application notes and mulitple accepted U.S. patents.

Reducing operational costs of ultra-reliable low latency services in 5G

József Varga, Attila Hilt, József Bíró, Csaba Rotter, and Gábor Járó

Abstract— Ultra-reliable low latency (uRLL) communication in 5G dictates the deployment of distributed infrastructure with numerous datacenters for low latency, while hosting ultra-reliable services mandates attended datacenters. This would boost the operational costs of 5G network operators planning country-wide coverage for uRLL services. This paper examines how these operational expenses dominated by administrative costs can be reduced without impacting the quality of the provided uRLL service. Our results indicate that hosting uRLL services in unattended datacenters with increased hardware redundancy schemes can produce significant cost savings.

Index Terms—G, availability, low latency, redundancy, total cost of ownership, cloud, datacenter

I. INTRODUCTION

ULTRA-reliable low latency (uRLL) communication introduces stringent requirements for 5G systems [1], [2], [3]. A recent cost study [4] shows that provisioning uRLL services can represent significant part of complete 5G deployments. This is triggered by the demanding service requirements: (i) for ultra-reliability the standard solution is to deploy Tier-4 attended datacenters [5], [6]; (ii) for low latency these datacenters must be placed either at the edge or close to the edge of the core network.

3GPP has an ongoing study on enhancements for the support of uRLL communication [7]. This study only sets recommendations for the future normative specification work and assumes that the 5G system defined in [8] will be used as a baseline architecture for uRLL communication. Even though the detailed architecture specification for uRLL communication is still ongoing, for the deployments the general 5G system deployment assumptions are valid: it will utilize technologies like software defined networking and network function virtualization. Furthermore, due to the stringent latency requirements we can assume that application functions supporting uRLL services are not only hosted by the same infrastructure as the 5G core system but are co-located or even combined with 5G network functions.

In this paper, we examine how the costs of uRLL service deployments can be reduced. The paper is structured as follows: section 2 discusses how the latency requirements of uRLL services enforce the introduction of costly distributed deployment using coverage for Hungary as an example, and lists potential cost reduction options; section 3 deals with the possible unattended operation of datacenters hosting only low traffic volume of uRLL services [9]; section 4 presents the potential cost saving results compared to the costs of standard operation described in [4]; finally, section 5 concludes the paper.

II. COSTS OF DEPLOYMENT FOR URLL SERVICES

The best-known example for uRLL services is the vehicle-to-everything (V2X) communication, including use cases like cooperative driving maneuvers (e.g. platooning), basic safety message, and see-through-system [10]. In densely populated countries the density of road system mandates nation-wide coverage. We use Hungary as an example to demonstrate how the uRLL service requirements are considered in planning the serving infrastructure.

II. 1 Infrastructure for uRLL Services

The end-to-end (E2E) latency requirements for V2X use cases available in the related literature and publications range from 3.3 millisecond (ms) [10], sub 10 ms [11], to 10-15 ms [2]. Independently of the actual value selected for E2E latency budget, it is further divided to elements like: service request processing at end user application, transmitting and receiving data at air interface, forwarding data in wired core network (fiber-optic), switching in packet data network, and optionally request handling in a server, see Fig.1. The use of these elements depends on what entities the uRLL service requires the network to connect: (i) a user to a server, (ii) two users using the network infrastructure, or (iii) users through a server.

user	air interface	core network edge	aggregation network (fiber optic)	Datacenter
application level processing + transmit/receive data	data forwarding at 300 km / ms	transmit / receive	data forwarding at 200 km / ms	switching request processing

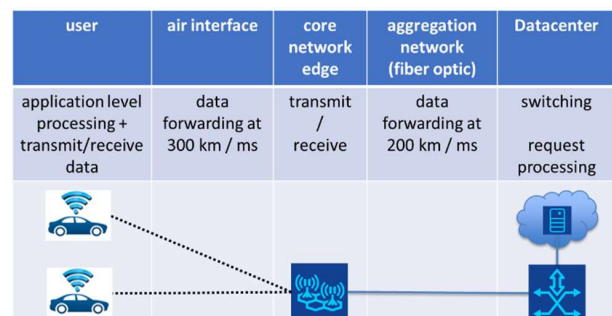Fig. 1. Latency elements in 5G network.

J. Varga is with NOKIA, Budapest, Hungary. E-mail: jozsef.varga@nokia.com.
A. Hilt is with NOKIA, Budapest, Hungary. E-mail: attila.hilt@nokia.com.
J. Bíró is with NOKIA, Budapest, Hungary. E-mail: jozsef.biro@nokia.com.
Cs. Rotter is with NOKIA, Budapest, Hungary. E-mail: csaba.rotter@nokia.com.
G. Járó is with NOKIA, Budapest, Hungary. E-mail: gabor.jaro@nokia.com.

Reducing operational costs of ultra-reliable
low latency services in 5G

The infrastructure serving the uRLL service is determined by the latency budget assigned for data forwarding in fiber-optic: as an example, if no time is assigned, then the uRLL service must be provided by mobile edge computing; while if 1 ms is assigned, then it allows data forwarding as far as 200 km in fiber-optic cable length. This "cable length budget" determines how the datacenters serving uRLL communications (for simplicity we use the term "low latency datacenter", LL DC in short) must be located to provide nation-wide coverage. For the user-server-user scenario the E2E communication includes two "data forwarding in fiber-optic" elements and to avoid further splitting of the "cable length budget", we assume that for a specific uRLL communication session at a specific time all network functions are hosted in one LL DC, and as the server processing time is also strongly limited, we can also assume that all network functions are combined for uRLL communication. Note that the evaluation part of [7] suggests that servers needs to be kept geographically and topologically close to the user equipment, "within a transmission latency of 0.1 ms to 1 ms from the radio base station site".

Also, if the LL DCs are placed to serve the user-server-user scenario, then the resulting setup can appropriately serve the less demanding user-server scenario as well.
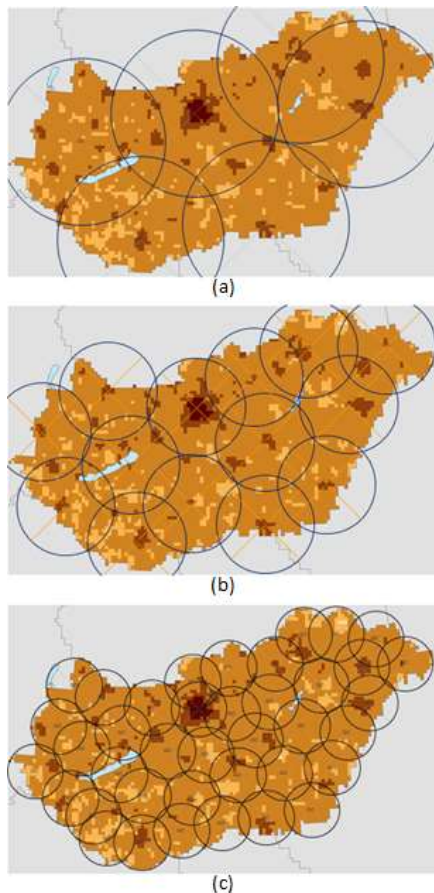
Fig. 2. LL DCs for Hungary with 100 / 60 / 33 km coverage radii.

The "cable length budget" determines the area covered by a LL DC, although for exact calculations the actual topology of the aggregation network is needed. For general calculations we estimate these areas as circles drawn around the potential locations of LL DCs. For this, we assume that the fiber-optic cable length connecting two points is usually 2-3 times longer than the geographical distance of those points.

As an example, Fig. 2 shows three options for LL DC placement in Hungary with different latency and cable length multiplier (mL) assumptions (copyright note: the population density map of Hungary is based on [12]).

Note that this circle-based coverage is only an estimate. In real-life deployments for uRLL services the locations of LL DCs must be designed based on the real cable lengths in the aggregation network.

In our model we did not aim to find coverage with minimal number of LL DCs, or full coverage, we just tried to place data centers to bigger cities wherever it was possible. Table 1 lists the estimated number of LL DCs needed to provide a country-wide coverage with three combinations of the latency and the cable length multiplier parameter values.

Option 2a assigns 2 ms latency from the E2E latency budget for data forwarding in fiber-optic (allowing 400 km cable length E2E) and mL = 2 as a multiplier for geographical distance to fiber-optic cable length. Keeping the user-server-user V2X use cases in mind, this translates to a 100 km coverage radius for LL DCs. Note that the 2 ms latency budget for forwarding data in fiber-optic is most probably too generous.

Option 2b takes 1.5 ms latency and mL = 2.5 length multiplier as parameters, resulting in a 60 km coverage radius. For comparison, cost calculations in [4] use a 72 km coverage radius.

Option 2c takes 1 ms latency for data forwarding in fiber-optic and mL = 3 as a geographical distance to optical cable length multiplier, resulting in a 33 km coverage radius for LL DCs.

Fig. 2 and Table 1 illustrate well that the number of LL DCs required to provide nation-wide coverage increases quickly as the latency requirements become harsher. The relation in our model coverage with circles around LL DCs is quite clear: the covered area is a quadratic function of the coverage radius. Even though with smaller coverage radius the nationwide coverage is achievable with less overlap among the coverage areas of LL DCs, and the coverage areas can follow better the country boundaries, still any decrease in the "cable length budget" will result a quadratic increase in the number of LL DCs for a country-wide coverage.

TABLE I
ESTIMATES FOR NATION-WIDE COVERAGE WITH LL DCS

Figure	2a	2b	2c
Latency budget for fiber-optic	2 ms	1.5 ms	1 ms
Cable length multiplier, m_L	2	2.5	3
Coverage radius for LL DCs	100 km	60 km	33 km
Number of LL DCs for nation-wide coverage	6	14	39

This statement is obviously valid for real deployments as well when the actual topology of the operator's aggregation network with real-life fiber-optic cable length is considered.

II. 2 Cost Considerations

Results in [4] indicate that IT admin costs could be the most significant cost contributor of the planned 5G infrastructure. IT admin costs are dominated by the 24/7 on-site support required for all LL DCs, see Fig. 3 that compares the monthly infrastructure costs of the main 5G use case groups: in addition to the uRLL services, the massive machine type communication – mMTC, evolved mobile broadband – eMBB, and ultra-dense high broadband service – uHBS. Note that those calculations use the standard cost calculations for datacenters [13], the IT admin costs are boosted by the fact that even for LL DCs covering rural areas with low traffic volumes (and thus hosting only tens of servers) the employment of 5 IT administrators is required: 40 working hours (minus vacations and sick leaves) per week to cover 168 hours a week.

In this work we focus on the IT admin cost reduction possibilities and leave other assumptions of [4] unchanged. For the 5G architecture it is assumed that (i) virtualization technologies [14] are used in all datacenters (including LL DCs), (ii) hard switches provide connectivity in the DC and may implement some services, e.g. user plane gateways, if they are SDN enabled [15], (iii) no other specialized hardware are deployed.

The obvious IT admin cost reduction possibility for LL DCs is to host additional services and share the IT admin costs with those services. Note that the intra-operator datacenter sharing possibilities are already considered in [4]. For example, datacenters hosting services like massive machine type communication and evolved mobile broadband on a national level, are also used as LL DC. In our example we can assume that the LL DC for the capital area is colocated with the datacenter hosting national level services, and thus the IT admin costs for uRLL services are already shared in that datacenter.

However, IT admin cost sharing may not be viable option for most LL DCs. As shown in our example, for option 2a it is possible to place most of LL DCs into bigger cities (population of 100,000+ in case of Hungary, obviously this depends on the population density and the level of urbanization of the country considered), but switching to the more realistic datacenter coverage options, for option 2b it is still possible to place all LL DCs into cities (again this statement is country dependent), but for the majority of the LL DCs these are already smaller cities and it is not expected to have significant demand for database capacities (i.e. no sharing). Finally, for option 2c approximately 80% of the LL DCs are placed at rural areas. Note that the ratio of LL DCs in rural areas are even worse for big countries, as the country level road length is significantly higher).

Another IT admin cost reduction option is to host the uRLL services in 3rd party datacenters that meet the ultrareliability requirements. However, this option has the same limitation as sharing. Furthermore, if the 3rd party datacenter is not close enough to the operator's aggregation network, the extra routing further limits the available time in the E2E latency budget.

The third option is the unattended operation of datacenters hosting uRLL services only. To ensure that the reliability requirements are still met, this must be compensated by deploying additional redundant hardware. In section 3 we examine the feasibility of this option.

III. UNATTENDED DATACENTERS FOR URLL SERVICES

We will examine how the lack of on-site IT support affects the service availability in LL DC and how it can be compensated by additional redundant hardware in LL DCs.

Obviously, high service reliability and high service availability are not equivalent terms. However, maintaining the same high service availability with high mean uptime values and keeping the same serviceability at the same time guarantee unchanged high reliability. For serviceability, the software in LL DCs is maintained remotely as virtualization technologies include centralized management and orchestration [14], while regular hardware maintenance can be provided without on-site IT administration as well.
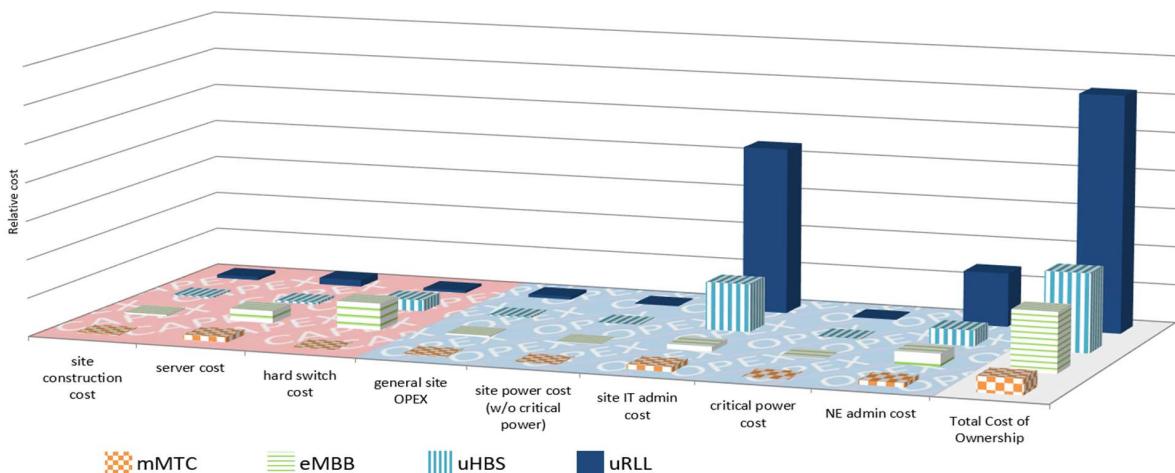

Fig. 3. Monthly total cost of ownership (TCO) of infrastructure for 5G use case groups [4].

III. 1 Assumptions

The assumptions used for LL DCs operated without on-site IT admin support are:

- those LL DC provide coverage for rural areas with low traffic volumes, thus the services are provided with minimal software configurations;
- those LL DC hosts only uRLL services;
- virtualization technologies [14] allow the remote management and configuration (automated and/or centralized) of software in those LL DCs;
- the virtual network functions (VNFs) are deployed on commodity servers;
- for hard switches and critical VNFs the 2N redundancy scheme is deployed;
- for other network functions utilizing load sharing redundancy scheme is the most efficient option [16];
- hard switches in LL DCs provide connectivity of the datacenter and may implement some services, e.g. user plane gateways, if they are SDN enabled [15];
- for best utilization of E2E latency budget the uRLL services are implemented in a single VNF (if any) and SDN based hard switches may implement user plane gateway functions.

III. 2 Considered Availability Parameters

The components of service availability in a datacenter are: software availability, hardware availability, datacenter infrastructure availability, and network availability. The dependency of these components with a high-level description is given in Fig. 4. The existence of on-site IT administration has impact only on the availability of IT hardware units by minimizing the downtime of hardware units (commodity servers and hard switches for the considered LL DCs). Note that regular maintenance impacting DC availability is still provided.

The hardware availability for network functions implementing uRLL services in LL DCs depends on both the availability of single hardware units (commodity server or hard switch, or even network interface cards) hosting the network function and the redundancy scheme applied for these hardware units. To obtain generic results we consider a range of typical values for uptime and downtime of a single hardware unit.

2N means full redundancy. For one single unit (N=1) 2N means duplication, such avoiding single point of failure. In case of several parallel units (N>1), all units are spared. In the system N units are required to support the traffic, but 2N units are deployed to increase the availability of the system. In 2N redundant systems, the system is capable to run as long as N units are available. 3N redundancy adds, for each unit carrying the load, two spare units in parallel. Please note, that the redundant units are not added to increase the system capacity: this way the system availability is improved. In 3N redundant systems, similarly to 2N redundancy, the system is capable to run as long as N units are available. "2 of 3" redundancy means that at least 2 units must operate from the total 3 units. Similarly, "2 of 4" means that minimum 2 units must operate from the total amount of 4 units. In the general case, N working units are spared by K redundant units, usually referred as N+K. The redundant units are either working or they are in standby mode. In active/active mode all the N+K units are working, and they share the total load (load-sharing). When K units are in standby mode, depending on the speed of launching the standby units into operation, we can talk about hot, warm or cold-standby. For the system performing its desired function, from the total number of N+K units at least N must operate, or in other words maximum K units can fail. The different sparing methods are discussed in detail in [17] and it is shown that in distributed systems load sharing efficiently increases the overall system availability.

For the redundancy schemes, we check all variants that match our assumptions (minimal configurations both for full redundancy and for load sharing based solutions). The examined values are:

- for the initial hardware redundancy scheme (i.e. when attended operation of LL DC is assumed) 1+1, 2+2 and 2+1 (also known as 2 of 3) redundancy;
- for uptime values, the mean time between failures (MTBF) parameter is used. The considered values are 200,000, 300,000, and 400,000 hours. Note that commodity server and hard switch vendors do not publish concrete values nowadays. Therefore, we adopted the typical values used by web pages and literature discussing availability, such as [18] and [19];
- for downtime values, the mean time to repair (MTTR) parameter is used. The considered values are 10, 20, 30, 40, 60, and 90 minutes. The widely used MTTR estimate for classical DC environment is 60 minutes, but as for 5G we expect high level of automation [20] including software management and configuration [14], our study focuses mostly on lower values.

III. 3 Availability Calculatiuon Details

For all combinations of the above parameters we first calculate the hardware availabilities with base redundancy schemes, then calculate the hardware availabilities using a more stringent redundancy scheme – obviously, receiving higher hardware availability values. Finally, we start to increase the MTTR value until the hardware availability with the more stringent redundancy scheme and increased Fig. 5. Base and increased hardware availability for MTBF=400,000 hours and MTTR = 10 minutes initial parameters.

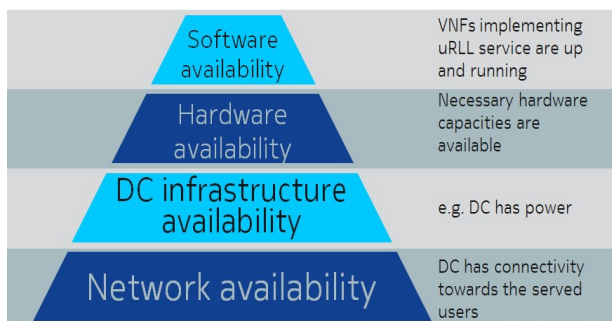MTTR drops back to the same value as with the base redundancy scheme and the initial MTTR value. The increase

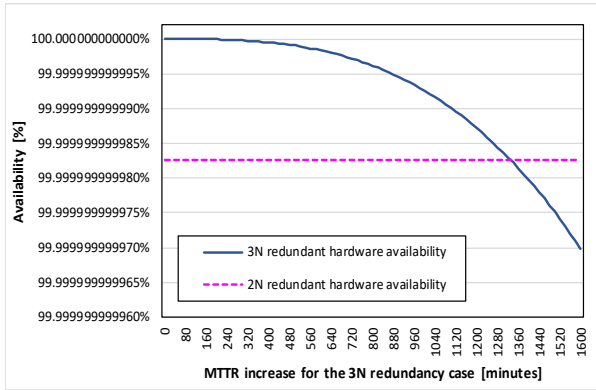Fig. 4. Main components for service availability in a datacenter..

Fig. 5. Base and increased hardware availability for MTBF=400,000 hours and MTTR = 10 minutes initial parameters.

in MTTR provides the additional time for IT administrators to travel to LL DCs.

As an example, this calculation is illustrated in Fig. 5, with MTBF set to 400,000 hours, MTTR set to 10 minutes, and redundancy scheme for the network function implementation of the uRLL service is assumed to be 2N redundancy. The base hardware availability for this case is A2N=99.9999999999826 %. Switching to 3N redundancy the hardware availability increases to an even higher value of A3N=99.9999999999999999927662127444 %.

Note that the above hardware availability numbers represent 12 and 19 9's availability. Obviously, these numbers are just one component in the service availability, which is expected to remain in the typical range of telco services, i.e. 5 or 6 9's availability.

Continuing with the example, the hardware availability for the 3N redundant case drops to the value of the base 2N redundant setup when the MTTR is increased by 1330 minutes to 1340 minutes. That is if a uRLL service is implemented on a 2N redundant hardware in an attended LL DC (assuming 400,000 hours MTBF and 10 minutes MTTR), then implementing the same uRLL service on a 3N redundant hardware guarantees the same hardware availability even if MTTR is increased to 1340 minutes.

The formulas used for basic availability calculation of a single hardware unit and the hardware availability for implementations are listed here for information, the details are available in [4].

The generic availability is defined in (1), MUT and MDT representing the mean uptime and mean downtime of the system, respectively.

$$Availability = MUT/(MUT+MDT) \qquad (1)$$

The availability of a single hardware with the wellknown function based on MTBF and MTTR, as specified in (2). Note that other definitions also exist in the literature [16], [19].

$$A_{single}(MTBF, MTTR) = MTBF/(MTBF+MTTR) \qquad (2)$$

The hardware availability for the 2N redundancy scheme is calculated as in (3), while for the 3N redundancy scheme is calculated according to (4).

$$A_{2N}(x, y) = 1-(1-A_{single}(x, y))^2 \qquad (3)$$
$$A_{3N}(x, y) = 1-(1-A_{single}(x, y))^3 \qquad (4)$$
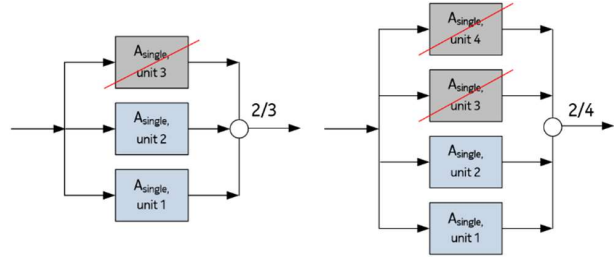
Fig. 6. "2 of 3" and "2 of 4" redundant parallel systems.

Hardware availability for the "2 of 3" redundancy scheme is calculated according to (5), while for the "2 of 4" redundancy scheme it is calculated according to (6).

$$A_{2/3}(x, y) = 3A_{single}(x, y)2-2A_{single}(x, y)^3 \qquad (5)$$
$$A_{2/4}(x, y) = 1-(4(1-A_{single}(x, y))3-3(1-A_{single}(x, y))^4) \qquad (6)$$

The "2 of 3" and "2 of 4" redundancy schemes are depicted in Fig. 6. These schemes are regularly referred as "2+1" and "2+2" as well.

III. 4 Results

Previously we have explained our calculations for a specific parameter set, here the results for all parameter combinations are summarized:

- single hardware availability values for all (MTBF, MTTR) combinations are in Table 2;
- hardware availability values both for 2N and 2+1 (or "2 of 3") redundancy schemes are well above the usual service availability values (more than ten 9's), so for better illustration we include the unavailability values for these cases: the unavailability values in Table 3 are for

TABLE 2
SINGLE HARDWARE UNIT AVAILABILITIES FOR THE EXAMINED
MTBF, MTTR RANGE

$A_{single}(MTBF, MTTR)$ (as %)			
MTTR (minutes)	MTBF (hours)		
	200,000	300,000	400,000
10	99.999917	99.999944	99.999958
20	99.999833	99.999889	99.999917
30	99.999750	99.999833	99.999875
40	99.999667	99.999778	99.999833
60	99.999500	99.999667	99.999750
90	99.999250	99.999500	99.999625

TABLE 3
HARDWARE UNAVAILABILITY WITH 2N REDUNDANCY SCHEME

$1-A_{2N}(MTBF, MTTR)$			
MTTR (minutes)	MTBF (hours)		
	200,000	300,000	400,000
10	6.9444E-13	3.0864E-13	1.7364E-13
20	2.7778E-12	1.2346E-12	6.9444E-13
30	6.2500E-12	2.7778E-12	1.5625E-12
40	1.1111E-11	4.9383E-12	2.7778E-12
60	2.5000E-11	1.1111E-11	6.2500E-12
90	5.6249E-11	2.5000E-11	1.4062E-11

Reducing operational costs of ultra-reliable
low latency services in 5G

TABLE 4
HARDWARE UNAVAILABILITY WITH 2+1 REDUNDANCY SCHEME

$1-A_{2/3}$(MTBF, MTTR)			
MTTR (minutes)	MTBF (hours)		
	200,000	300,000	400,000
10	2.0833E-12	9.2593E-13	5.2081E-13
20	8.3333E-12	3.7037E-12	2.0833E-12
30	1.8750E-11	8.3333E-12	4.6875E-12
40	3.3333E-11	1.4815E-11	8.3333E-12
60	7.4999E-11	3.3333E-11	1.8750E-11
90	1.6875E-10	7.4999E-11	4.2187E-11

2N redundancy scheme, while the unavailability values in Table 4 are for 2+1 (or "2 of 3") redundancy scheme.

- The hardware availability values both for 2N and 2+1 (or "2 of 3") redundancy schemes are illustrated in Fig. 7.

The hardware availability values for the improved redundancy schemes are not illustrated in any tables or figures, as with the base MTTR the hardware availability values are "too close" to 1 (see the example earlier with 19 9's).

- Table 5 lists the potential MTTR increase (for all the considered MTBF/MTTR combinations) for LL DCs where uRLL services are originally provided by a single network function implemented with 2N redundancy, and the network function implementation is switched to 3N redundancy to allow unattended LL DC operation;
- Table 6 is similar, but the original network function redundancy scheme is 2+1, and it is switched to 2+2 scheme;
- Table 7 combines the two cases assuming that the uRLL service are originally provided by two network functions: an SDN based 2N redundant hard switch as a user plane gateway, and 2+1 redundant control plane network function.

Note that all the values for "MTTR increase" are rounded off to 10 minutes. For example, in Table 5 the value 1200 in the cell of MTTR 10 minutes and MTBF 300 k hours means (7). That is assuming 300,000 MTBF, if the MTTR is increased by
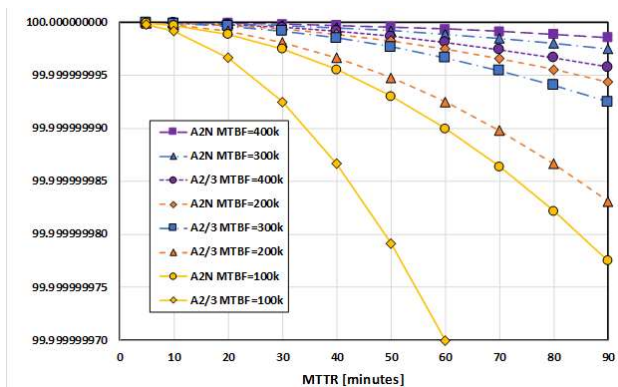
Fig. 7. Availability of 2N and "2 of 3" redundant systems.

TABLE 5
MTTR INCREASE COMPENSATED BY SWITCHING FROM 2N TO 3N REDUNDANCY SCHEME

compensated MTTR increase (minutes)			
MTTR (minutes)	MTBF (hours)		
	200,000	300,000	400,000
10	1050	1200	1330
20	1660	1910	2100
30	2180	2500	2750
40	2630	3020	3330
60	3440	3950	4360
90	4500	5170	5700

TABLE 6
MTTR INCREASE COMPENSATED BY SWITCHING FROM 2+1 TO 2+2 REDUNDANCY SCHEME

compensated MTTR increase (minutes)			
MTTR (minutes)	MTBF (hours)		
	200,000	300,000	400,000
10	950	1090	1200
20	1510	1730	1910
30	1970	2260	2500
40	2390	2740	3020
60	3120	3590	3950
90	4080	4690	5170

TABLE 7
MTTR INCREASE COMPENSATED FOR THE COMBINED CASE

compensated MTTR increase (minutes)			
MTTR (minutes)	MTBF (hours)		
	200,000	300,000	400,000
10	970	1110	1230
20	1540	1770	1950
30	2020	2310	2550
40	2440	2800	3090
60	3190	3660	4040
90	4180	4790	5280

1200 minutes to 1210 minutes, the 3N hardware redundancy scheme still provides the same hardware availability as the 2N hardware redundancy scheme with a 10 minutes MTTR.

$$A_{3N}(300000, 1210) > A_{2N}(300000, 10) > A_{3N}(300000, 1220) \quad (7)$$

The results show that the unattended operation for a LL DC that provides uRLL services by hosting at most a hard switch (for data forwarding) and an additional virtual network function for each uRLL service is possible. Furthermore, as the potential MTTR increase allowed by switching to more stringent redundancy schemes is practically above 16 hours for any practical combination of (MTBF, MTTR) value pairs, the IT administrators responsible for the LL DCs can be employed in a single shift. More details on the cost consequences are given in the next section.

IV. Cost Consequences

From the considered IT admin cost reduction possibilities, the hosting of 3rd party services in LL DC has a straightforward impact on the expenses of the uRLL services: the IT admin costs are reduced. We do not consider changes in other elements of the TCO: even though hosting 3rd party services requires deploying additional hardware capacities in LL DC means increase in both the capital expenses and the power consumption of the LL DC, it is fair to assume that the income of hosting activity compensates these additional costs.

As the dominating cost for uRLL services the IT admin costs are boosted by the fact that operators must employ 5 IT administrators for 24/7 supervision of relatively low number of servers, while normally an IT administrator may supervise hundreds of servers [13]. In [4] 500 servers per IT administrator are used in calculations. Hosting 3rd party services allows better utilization of the IT administrators. Note that even though operators may not share IT admin costs proportionally to the used hardware capacities (as an example if a LL DC requires 50 servers and hard switches to provide uRLL services, and an additional 100 hardware elements to host 3rd party services, the 3rd party tenants may not be ready to pay 2/3 of the IT admin costs, but rather a 20% (100/500) only), sharing still can provide significant IT admin cost save. Obviously to avoid cost increase instead of cost save, operators must find long term reliable tenants.

As shown in section 3, unattended operation of LL DC is also an appealing option. It changes the LL DC TCO as follows:

- due to the increased redundancy scheme applied, the capital expenses are increased by 50%. This includes site construction costs (which is calculated from the power consumption of the servers and hard switches deployed in the datacenter), server costs, and hard switch costs;
- critical power (server and hard switch power consumption) cost increased by 50%;

- site power consumption (excluding critical power) assumed to be unaffected (usually calculated from critical power consumption, but the impact of increased critical power consumption is compensated by the removed on-site IT administrators;
- on-site IT admin cost is replaced by the cost of centralized "IT administrator pool" assigned to the regular maintenance of rural LL DCs and visiting a LL DC whenever a hardware error is detected (software administration is centralized). This allows the reduction of 5 IT administrators per LL DC to 0.5 IT administrator per LL DC. But the IT administrator employment costs are increased by 50% (e.g. regular travels, company cars).

Note that it is also possible to outsource IT administrators, and it may result in further cost reduction for the operation of unattended LL DCs, but it is not in the scope of this study.

Combined application of the two studied concepts is also possible (i.e. hosting 3rd party services in unattended LL DC), but increased hardware capacity in the LL DC may require more frequent IT administrator visits, and our availability calculations assume simple uRLL service deployments only. Availability calculations for more complex service deployments are not considered here.

Fig. 8 illustrates the cost saving potential of shared LL DC and unattended LL DC concepts. The calculations are based on the results of [4] (the standard DC cost model) and the two studied concepts are applied with different weights: the "no sharing – 90% unattended" concepts intends to model a strongly urbanized large country (10% of the LL DCs are located in big cities hosting regional level DCs anyway, the rest of LL DCs practically cover the road system of rural areas). While the other figures intend to model densely populated countries either with smaller number of huge cities, or relatively high number of bigger cities.
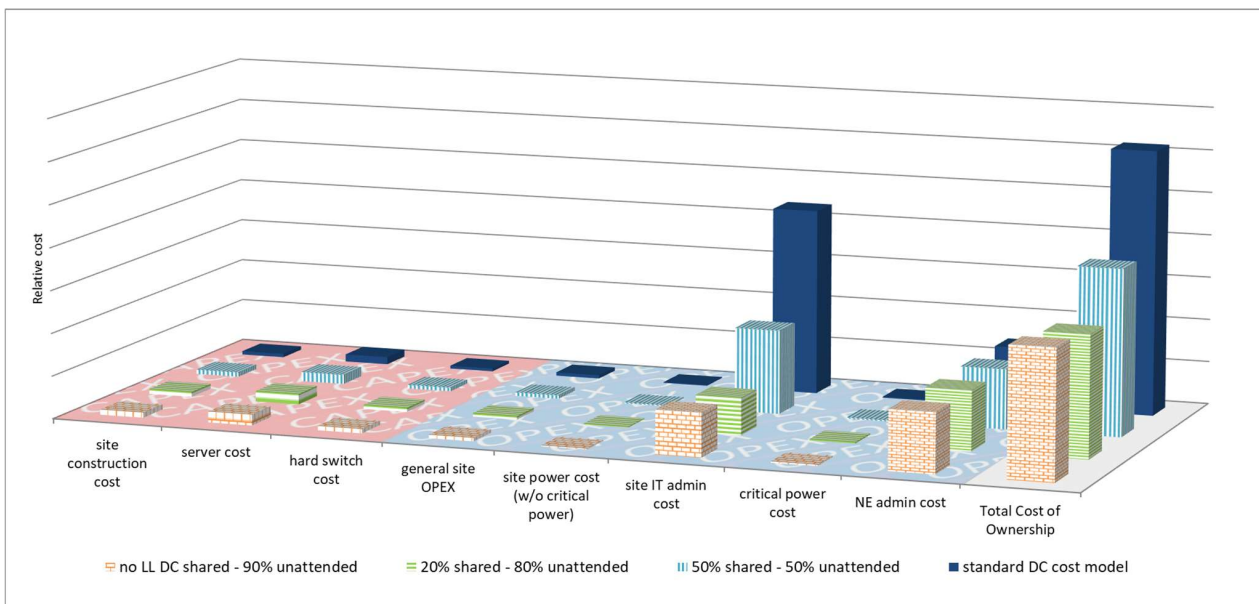

Fig. 8. TCO of uRLL services with different variations of LL DC operation concepts.

As cost calculations show, the cost saving potential is significant for both concepts. The applicability depends on the population density, urbanization, size of covered area, total road length of the operator's country and obviously the actual topology of the operator's aggregation network.

V. CONCLUSION

Initial study in 5G infrastructure TCO [4] made it obvious that for uRLL services standard datacenter operational model is way too expensive.

Both sharing LL DCs and unattended operation of LL DCs provide significant cost saving. The possibilities of sharing for LL DC can be limited geographically (big cities only), but it is nicely complemented by the unattended operation of LL DCs, which is applicable for rural areas with low traffic volumes.

The main drawback for unattended operation of LL DCs is being environmentally "unfriendly": with more servers and switches deployed the power consumption increases and this requires regular travel for visiting IT administrators. The latter can be reduced (potentially resulting further cost reduction) if operators outsource IT admin tasks.

Our current work focuses on maintaining service availability in a single LL DC, service availability for special cases involving multiple LL DCs, e.g. mobility related handover scenarios or services implemented by distributed applications, requires further study.

ACKNOWLEDGMENT

REFERENCES

[1] NGMN alliance, NGMN 5G White Paper, 2015-02.

[2] 3GPP, TR 22.862; Feasibility Study on New Services and Markets Technology Enablers for Critical Communications; V14.1.0, 2016-09.

[3] 3GPP, TR 22.891; Feasibility Study on New Services and Markets Technology Enablers; V14.2.0, 2016-09.

[4] Kiess, W., Sama, M. R., Varga, J., Prade, J., Morper, H. and Hoffmann, K., "5G via Evolved Packet Core Slices: Costs and Technology of Early Deployments", *Proc. IEEE Symp. Personal, Indoor, and Mobile Radio Communications (PIMRC '17)*, pp. 1-7, Oct. 2017, DOI: 10.1109/PIMRC.2017.8292691.

[5] Varga, J., Hilt, A., Rotter, Cs. and Járó, G., "Providing Ultra-Reliable Low Latency Services for 5G with Unattended Datacenters", *Proc. IEEE Symp. Communication Systems, Networks & Digital Signal Processing (CSNDSP '18)*, pp. 1-4, Jul. 2018, DOI: 10.1109/CSNDSP.2018.8471756.

[6] Turner IV, W. P., Seader, J. H., Renaud, V. and Brill, K. G., Tier Classifications Define Site Infrastructure Performance, The Uptime Institute white paper, 2006.

[7] 3GPP, TR 23.725; Study on enhancement of Ultra-Reliable Low-Latency Communication (URLLC) support in the 5G Core network; V16.0.0, 2018-12.

[8] 3GPP, TS 23.501; System Architecture for the 5G System; V15.4.0, 2018-12.

[9] TIA-942-A, Telecommunications Infrastructure Standard for Data Centers, 2012.

[10] Alieiev, R., Kwoczek, A. and Hehn, T., "Automotive Requirements for Future Mobile Networks", *Proc. IEEE MTT-S International Conference on Microwaves for Intelligent Mobility (ICMIM '15)*, pp. 1-4, Apr. 2015, DOI: 10.1109/ICMIM.2015.7117947.

[11] Simsek, M., Aijaz, A., Dohler, M., Sachs, J. and Fettweis, G., " 5G-Enabled Tactile Internet", IEEE Journal on Selected Areas in Communications, vol. 34, pp. 460–473, March 2016.

[12] Gridded Population of the World," Hungary: Populationdensity, 2000", available at http://sedac.ciesin.columbia.edu/gpw.

[13] Barroso, L., Clidaras, J. and Hölzle, U., "The Datacenter as a Computer: An Introduction to the Design of Warehouse-Scale Machines", Morgan & Claypool, 2nd edition, 2013.

[14] ETSI, GS NFV-MAN 001; Network Functions Virtualisation (NFV); Management and Orchestration; V1.1.1, 2014-12.

[15] An, X., Kiess, W., Varga, J., Prade, J., Morper, H. and Hoffmann, K., "SDN-based vs. software-only EPC gateways: A cost analysis", *Proc. IEEE NetSoft Conference and Workshops (NetSoft '16)*, pp. 146-150, June 2016, DOI: 10.1109/NETSOFT.2016.7502461.

[16] Hilt, A., Járó, G. and Bakos, I., "Availability Prediction of Telecommunication Application Servers Deployed on Cloud", *Periodica Polytechnica Electrical Engineering and Computer Science*, 60(1) pp. 72-81, 2016.

[17] Nagy, L., Hilt, A., Járó, G., Oláh, D. and Talyigás, Zs., "Comparison of Availability Figures of Distributed Systems Using Multiple Redundancy Methods", AACS'2016 Workshop, June 2016.

[18] Taylor, Z. and Ranganathan, S., "Designing High Availability Systems: DFSS and Classical Reliability Techniques with Practical Real-Life Examples", Wiley - IEEE Press, November 2013.

[19] Bauer, E., Adams, R., "Service Quality of Cloud-Based Applications", Wiley, IEEE Press, ISBN 978-1-118-76329-2, 2017.

[20] ONAP, Beijing Release Notes, V2.0.0, June 2018.

József Varga, PhD, is a senior research engineer at Nokia, member of the 'Multi Cloud Orchestration' research group in Nokia Bell Labs. He received his MSc in computer science and mathematics from the University of Szeged in 1991, PhD in IT from the University of Veszprém in 2002. He was an assistant professor at the University of Szeged, then at the University of Veszprém. He joined Nokia in 1999, he was involved in IP Multimedia Subsystem development, then represented Nokia as a standardization delegate in 3GPP from 2004 to 2011. In 2011 he joined Nokia Research Center (now Nokia Bell Labs) dealing with topics like SDN, virtualization, and orchestration. Currently he is focusing on resource management in 5G, including the economic aspects. He co-authored more than 10 papers and more than 10 granted patents.

Attila Hilt, PhD, graduated in Electrical Engineering from the Budapest University of Technology and Economics (BME) in 1990. In 1989 he joined the Research Institute for Telecommunications (TKI) Budapest, Hungary. Until 1999, he headed the Telecommunication Test Laboratory of TKI. In May 1999, he received the 'Doctor of INPG' degree from the Institute National Polytechnique de Grenoble, France. He received the PhD degree in 2000 from BME. He joined Nokia Networks in 2000 where he is currently working as senior system specialist. He has been involved in the dimensioning and design of several mobile and cloud networks. He participated in the testing, piloting, deployment and optimization of mobile and backhaul networks, including nationwide modernization projects in Europe. His research interests include measurement techniques, fixed, wireless, mobile and cloud-based communication networks, microwave, millimeter-wave and photonic systems. He authored/co-authored more than 80 papers and more than 120 research and project reports, guidelines and specifications. He is a member of the Scientific Association of Infocommunications (HTE) and the Hungarian Chamber of Engineers (MMK). Since 2016 he is a member of the Telecommunications Public Body of the Hungarian Academy of Sciences and since 2018 a member of the Telecommunications Scientific Committee (MTA TTB).

József Bíró is a senior research engineer at Nokia Bell Labs. He received his MSc in electrical engineering from the Budapest University of Technology and Economics (BME) in 1990, with specialization in Measurement and Industrial Control Technologies. He started his professional career at the Hungarian Research Institute for Particle and Nuclear Physics where he designed embedded software systems for scientific spacecrafts. He joined Nokia Research Center in 1998, where he first specialized in Java technologies (JVM in particular) and helped the adoption of Java for mobile platforms. From 2004 onwards, he worked on high availability technologies for telecommunication platforms. His related activities included industrial specification work in Service Availability Forum. Starting from 2010, he turned towards virtualization and cloud technologies, particularly dealing with the deployment and management of complex applications in the cloud. During this period, he participated in the EU FP7 project 4CaaSt, where he was a task leader within a work package. He is currently the member of Nokia Bell Labs 'Multi Cloud Orchestration' research group and his current focus is on advanced end-to-end orchestration for telco cloud platforms, NFV and beyond, with strong outlook towards 5G systems.

Csaba Rotter is heading 'Multi Cloud Orchestration' research group in Nokia Bell Labs. He is involved in different cloud related research topics targeting cloud native network service operation challenges in highly distributed multivendor environment. His special interest is on how to ensure performance related service level agreements for concurrent applications sharing the resources in the same distributed environment. His passion in automation started years before, when he was responsible for test automation concept development in large telecommunication systems. He received MSc in applied electronics at the Technical University of Oradea in 1995 and MSc in IT management at the Central European University Budapest in 2008. He joined Nokia in 1999, later Nokia Research Center (currently Nokia Bell Labs) in 2008.

Gábor Járó, PhD, is a chief architect at Nokia. He received MSc degree in Electrical Engineering at the Budapest University of Technology and Economics (BME) in 1994. In the same year, he joined the Department of the Micro-wave Telecommunication at BME, where he started working on his PhD degree. His research interest focused on noise in high-speed optical receiver and optical system, millimeter-wave signal generation in optical systems. He received the PhD degree in 2001 from BME. He joined Nokia in 1999, he has been involved in the design of several mobile and cloud network elements and networks. His research interests include measurements in mobile and cloud-based communication networks, design and realization of ultra-reliable low latency network elements. He authored/co-authored more than 50 papers and several granted patents.

Special Issue on Cryptology

Call for Papers

This special issue will focus on the area of cryptology and will include selected papers from the 2019 Central European Conference on Cryptology. It will cover various aspects of cryptology, including but not limited to

- cryptanalysis,
- cryptographic applications in information security,
- design of cryptographic systems,
- encryption schemes,
- general cryptographic protocols,
- post-quantum cryptography,
- pseudorandomness,
- signature schemes,
- cryptocurrencies, blockchain,
- steganography.

Detailed information on submissions to CECC 2019 and other information is provided at https://www.fi.muni.cz/cecc/ , with April 1, 2019 being the deadline for the submission of abstracts that will be reviewed by the program committee and authors will be informed about acceptance or rejection by April 22, 2019. The conference registration deadline will be May 15, 2019, and the conference dates are June 12-14.

Submissions and presentations at the conference will be evaluated by the program committee and authors will be informed about the evaluation results no later than June 21.

No more than 5 papers from the workshop shall be selected for the special issue of the Infocommunications Journal, and authors of these papers will have the opportunity to revise their papers (including typesetting in the IEEE format) after the conference – final versions for the special issue will be due July 22, 2019.

Guest Editors:

Václav (Vashek) Matyáš is a Professor at Masaryk University, Brno, CZ, acting as the Vice-Dean for Industrial and Alumni Relations at the Faculty of Informatics. His research interests are related to applied cryptography and security; he has published well over 150 peer-reviewed papers and articles and has co-authored several books. He worked in the past with Red Hat Czech, CyLab at Carnegie Mellon University, as a Fulbright-Masaryk Visiting Scholar at the Center for Research on Computation and Society of Harvard University, Microsoft Research Cambridge, University College Dublin, Ubilab at UBS AG, and as a Royal Society Postdoctoral Fellow with the Cambridge University Computer Lab. Vashek also worked on the Common Criteria and in ISO/IEC JTC1 SC27. Vashek is a member of the Editorial Board of the Infocommunications Journal and can be contacted at matyas AT fi.muni.cz.

Pavol Zajac is a Professor of Applied Computer Science at Slovak University of Technology in Bratislava, Slovakia. His research interests are related to mathematical cryptography and information security. Nowadays he works mostly with post-quantum cryptography and related algebraic problems. Pavol can be contacted pavol.zajac AT stuba.sk.

Jan Hajný works as an Associate Professor at the Faculty of Electrical Engineering and Communication at Brno University of Technology. He is the head of the Advanced Cybersecurity group, member of the faculty's Scientific Committee and the person responsible for the Information Security study programs. The scientific activities of prof. Hajny include research into modern cryptography and privacy protection. Prof. Hajny is the principal investigator of many projects, including Czech grants (GAČR, TAČR) and international projects (Horizon 2020). He is also active in the contractual research for major Czech companies and in international collaboration with institutions visited as a visiting researcher, i.e., KU Leuven, BE; IBM Research Zurich, CH; and University of Minnesota, USA.

Marek Sýs is an Assistant Professor at Masaryk University, Brno, CZ. His research interests are related to applied cryptography where he published 12 peer-review papers. His collaborative work received Real-World Award at ACM CCS 2017 for discovering ROCA vulnerability. He worked in the past as Postdoctoral Research Associate at Masaryk University and Assistant Professor at Technical University, Bratislava. He received his PhD degree from the Technical University, Bratislava, and can be contacted at syso AT mail.muni.cz.

Mark your calendar for

tsp 2019

2019
42nd International Conference on
Telecommunications and Signal Processing
(TSP)

July 1-3, 2019
Budapest, Hungary

Call for Papers

Stay connected:
Email: tsp@feec.vutbr.cz
Web: http://tsp.vutbr.cz/
Facebook: https://www.facebook.com/TSPconf
Twitter: https://twitter.com/TSPconf

Important dates:
Paper Submission: February 15, 2019
Notification of Acceptance: April 15, 2019
Authors' Registration: May 20, 2019

See you soon in Budapest!

ORGANIZERS

The **2019 42nd International Conference on Telecommunications and Signal Processing (TSP)** will be held during **July 1-3, 2019** in **Budapest, Hungary**. The conference is organized by seventeen universities from Czech Republic, Hungary, Turkey, Taiwan, Japan, Slovak Republic, Spain, Bulgaria, France, Slovenia, Croatia, and Poland, for academics, researchers, and developers and it serves as a premier annual international forum to promote the exchange of the latest advances in telecommunication technology and signal processing. The aim of the conference is to bring together both novice and experienced scientists and developers to meet new colleagues, collect new ideas, and establish new cooperation between research groups from universities, research centers, and private sectors. We look forward to your innovative contributions in any of the following areas:

Telecommunications:

- Information Systems
- Network Services
- Network Technologies
- Telecommunication Systems
- Modelling, Simulation and Measurement

Signal Processing:

- Analog Signal Processing
- Audio, Speech and Language Processing
- Biomedical Signal Processing
- Digital Signal Processing
- Image and Video Signal Processing

Prospective Organizers are invited to submit proposals for Special Sessions and Workshops!

PROCEEDINGS

All accepted papers will be published in the TSP 2019 Conference Proceedings issued online. The Proceedings with presented papers will be submitted for indexing in **IEEE Xplore® Digital Library—IEEE Conference Record #46676** (pending approval), **Conference Proceedings Citation Index (CPCI) of Thomson Reuters**, **SCOPUS**, **DBLP**, and **Google Scholar** databases. *Selected papers will be published in special issues of international journals*.

IMPORTANT DATES	CONTACTS	FOLLOW US
Paper Submission: *February 15, 2019*	**E-mail:** tsp@feec.vutbr.cz	FACEBOOK */tspconf*
Notification of Acceptance: *April 15, 2019*	**Web:** http://tsp.vutbr.cz/	TWITTER */tspconf*
Authors' Registration: *May 20, 2019*		

Guidelines for our Authors

Format of the manuscripts

Original manuscripts and final versions of papers should be submitted in IEEE format according to the formatting instructions available on

http://www.ieee.org/publications_standards/ publications/authors/authors_journals.html#sect2,

"Template and Instructions on How to Create Your Paper".

Length of the manuscripts

The length of papers in the aforementioned format should be 6-8 journal pages.
Wherever appropriate, include 1-2 figures or tables per journal page.

Paper structure

Papers should follow the standard structure, consisting of *Introduction* (the part of paper numbered by "1"), and *Conclusion* (the last numbered part) and several *Sections* in between.
The Introduction should introduce the topic, tell why the subject of the paper is important, summarize the state of the art with references to existing works and underline the main innovative results of the paper. The Introduction should conclude with outlining the structure of the paper.

Accompanying parts

Papers should be accompanied by an *Abstract* and a few *index terms (Keywords)*. For the final version of accepted papers, please send the *short cvs* and *photos* of the authors as well.

Authors

In the title of the paper, authors are listed in the order given in the submitted manuscript. Their full affiliations and e-mail addresses will be given in a footnote on the first page as shown in the template. No degrees or other titles of the authors are given. Memberships of IEEE, HTE and other professional societies will be indicated so please supply this information. When submitting the manuscript, one of the authors should be indicated as corresponding author providing his/her postal address, fax number and telephone number for eventual correspondence and communication with the Editorial Board.

References

References should be listed at the end of the paper in the IEEE format, see below:

a) Last name of author or authors and first name or initials, or name of organization
b) Title of article in quotation marks
c) Title of periodical in full and set in italics
d) Volume, number, and, if available, part
e) First and last pages of article
f) Date of issue

[11] Boggs, S.A. and Fujimoto, N., "Techniques and instrumentation for measurement of transients in gas-insulated switchgear," IEEE Transactions on Electrical Installation, vol. ET-19, no. 2, pp.87–92, April 1984.

Format of a book reference:

[26] Peck, R.B., Hanson, W.E., and Thornburn, T.H., Foundation Engineering, 2nd ed. New York: McGraw-Hill, 1972, pp.230–292.

All references should be referred by the corresponding numbers in the text.

Figures

Figures should be black-and-white, clear, and drawn by the authors. Do not use figures or pictures downloaded from the Internet. Figures and pictures should be submitted also as separate files. Captions are obligatory. Within the text, references should be made by figure numbers, e.g. "see Fig. 2."
When using figures from other printed materials, exact references and note on copyright should be included. Obtaining the copyright is the responsibility of authors.

Contact address

Authors are requested to submit their papers electronically via the EasyChair system. The link for submission can be found on the journal's website:
www.infocommunications.hu/for-our-authors

If you have any question about the journal or the submission process, please do not hesitate to contact us via e-mail:

Rolland Vida – Editor-in-Chief:
vida@tmit.bme.hu

Pál Varga – Associate Editor-in-Chief:
pvarga@hit.bme.hu

EuCNC 2019
June 18-21

European Conference on Networks and Communications | Valencia, Spain

Enabling Smart Connectivity

18 - 21 June 2019

www.eucnc.eu

EURASIP · IEEE ComSoc · IEEE Communications Society

CALL FOR PAPERS

EuCNC 2019 is the 28th edition of a successful series of a conference in the field of telecommunications, sponsored by the European Commission. The conference focuses on various aspects of 5G communications systems and networks, including cloud and virtualisation solutions, management technologies, and vertical application areas. It targets to bring together researchers from all over the world to present the latest research results, and it is one of the main venues for demonstrating the results of research projects, especially from successive European R&D programmes co-financed by the European Commission. This year's event also encourages insights from industrial deployments and experiences in the OPE track.

EuCNC 2019 will be co-located with the Global 5G Event, which brings together the world 5G industrial associations: 5G-IA, IMT-2020, 5G-Forum, 5G-MF, 5G-Brasil and 5G-Americas.

We invite submissions in 6 tracks on a wide range of topics including but not limited to:

PHY - Physical Layer and Fundamentals
New air interfaces (5G, MTC, mmWave, etc.)
Beyond 5G, Terahertz communication
New modulation and coding techniques
New antenna arrays and antenna types
Reconfigurable radios and new radio heads
Advanced and massive MIMO
Hardware/Software co-design and implementation

RAS – Radio Access and Softwarisation
New spectrum management and sharing methods
Reconfigurable and energy efficient RRM
Modular and reconfigurable MAC
Soft-RAN and fronthauling
Cognitive and green radio
New access architectures and technologies in 5G (UNB, UWB, DSA, etc.)
Radio slicing

NET – Network Softwarisation
New network protocols and architectures
Cognitive network management in 5G and beyond
Software defined networking
Network slicing management
Network function virtualization
Network programming for reconfigurability, mobility management, etc.
Fog and edge computing
Data aware networks and overlays (P2P, CDN, ICN, etc.)
Network operating system
Quality (QoE and QoS) aware networking
Security, trust and privacy

WOS – Wireless, Optical and Satellite Networks
5G access and core networks
Advances in M2M, WSN, IoT networks
Integrated and hybrid satellite/terrestrial networks
Next generation passive optical networks
Optical/Wireless convergence
Communications for unmanned platforms
Communications for navigation and observation

VAP – Vertical Applications and Internet of Things
Factory automation solutions
Autonomous driving solutions
Digital health and wellbeing
Critical communications and public safety
Agriculture and environmental monitoring
Smart cities and smart grids
Localization and location-based services
Emerging business models and monetization strategies

OPE – Operational & Experimental Insights
5G trials and experiments
Deployment insights from verticals (smart city, energy, digital health, public safety, automotive etc.)
Plug-and-play deployments and experiments
Advanced wireless platforms and testbeds
Network applications for test and production deployments
Network forensics, network instrumentation
Data driven network design and optimization
Next Generation Internet

Key dates: 2019 Feb. 08 – Papers submission deadline
2019 Apr. 15 – Notification of acceptance
2019 Apr. 26 – Final paper submission

General Co-Chairs
Pearse O'Donohue, E.C., BE
(To be defined), ES
Steering Committee Chairs
Luis M. Correia, IST-U. Lisbon, PT
Bernard Barani, E.C., BE
Technical Program Chairs
Narcis Cardona, iTEAM - U.P. València, ES
Track Co-Chairs
PHY - Physical Layer and Fundamentals
   David Lopez-Perez, Nokia Bell Labs, IE
   Laurent Clavier, U. Lille, FR
   Takahiro Aoyagi, Tokyo I.T., JP
RAS – Radio Access and Softwarisation
   Konstantinos Katzis, E.C.U., CY
   Luzango Mfupe, C.S.I.R., ZA
   Muhammad Z. Shakir, U. West Scotland, UK
WOS – Wireless, Optical and Satellite Netw.
   Salvador Sales, U.P. València, ES
   António Grilo, IST - U. Lisbon, PT
   Nader S. Alagha, ESTEC, NL
NET – Network Softwarisation
   Hamed Ahmadi, U.C.D., UK
   Zaheer Khan, CWC Oulu, FI
   Jeongchang Kim, KMOU, KR
VAP – Vertical App. and Internet of Things
   Carlos Palau, U.P. València, ES
   Kamran Sayrafian, N.I.S.T., USA
   Gordana Gardasevic, U. Banja Luka, BIH
OPE – Operational & Experimental Insights
   Benoit Derat, Rohde & Schwarz, DE
   Andrés Navarro, ICESI, CO
   Mansoor Hanif, OFCOM, UK
Panels Co-Chairs
   Pavlos Fournogerakis, E.C., BE
   Jose Monserrat, iTEAM – U.P. València, ES
   Javier Gozalvez, U.M.H., ES
Special Sessions Co-Chairs
   David Gómez-Barquero, U.P. València, ES
   Chiara Buratti, U. Bologna, IT
Workshops Co-Chairs
   Ramón Agüero, U. Cantabria, ES
   Bosco Fernandes, COMCON, DE
Exhibitions Co-Chairs
   Jorge Pereira, E.C., BE
   Uwe Herzog, EURESCOM, DE
   Conchi García, U.P. València, ES
Tutorials Co-Chairs
   Claude Oestges, U.C.L., BE
   Thomas Kuerner, U. Braunschweig, DE
IEEE/ComSoc Liaison
   Hikmet Sari, Sequans, FR
EURASIP Liaison
   Fernando Pereira, IST-U. Lisbon, PT
URSI Liaison
   Sana Salous, U. Durham, UK
COST Liaison
   Ralph Stübner, COST, BE

SCIENTIFIC ASSOCIATION FOR INFOCOMMUNICATIONS

Who we are

Founded in 1949, the Scientific Association for Info-communications (formerly known as Scientific Society for Telecommunications) is a voluntary and autonomous professional society of engineers and economists, researchers and businessmen, managers and educational, regulatory and other professionals working in the fields of telecommunications, broadcasting, electronics, information and media technologies in Hungary.

Besides its 1000 individual members, the Scientific Association for Infocommunications (in Hungarian: HÍRKÖZLÉSI ÉS INFORMATIKAI TUDOMÁNYOS EGYESÜLET, HTE) has more than 60 corporate members as well. Among them there are large companies and small-and-medium enterprises with industrial, trade, service-providing, research and development activities, as well as educational institutions and research centers.

HTE is a Sister Society of the Institute of Electrical and Electronics Engineers, Inc. (IEEE) and the IEEE Communications Society.

What we do

HTE has a broad range of activities that aim to promote the convergence of information and communication technologies and the deployment of synergic applications and services, to broaden the knowledge and skills of our members, to facilitate the exchange of ideas and experiences, as well as to integrate and harmonize the professional opinions and standpoints derived from various group interests and market dynamics.

To achieve these goals, we…

- contribute to the analysis of technical, economic, and social questions related to our field of competence, and forward the synthesized opinion of our experts to scientific, legislative, industrial and educational organizations and institutions;
- follow the national and international trends and results related to our field of competence, foster the professional and business relations between foreign and Hungarian companies and institutes;
- organize an extensive range of lectures, seminars, debates, conferences, exhibitions, company presentations, and club events in order to transfer and deploy scientific, technical and economic knowledge and skills;
- promote professional secondary and higher education and take active part in the development of professional education, teaching and training;
- establish and maintain relations with other domestic and foreign fellow associations, IEEE sister societies;
- award prizes for outstanding scientific, educational, managerial, commercial and/or societal activities and achievements in the fields of infocommunication.

Contact information

President: **GÁBOR MAGYAR, PhD** • *elnok@hte.hu*
Secretary-General: **ERZSÉBET BÁNKUTI** • *bankutie@ahrt.hu*
Operations Director: **PÉTER NAGY** • *nagy.peter@hte.hu*
International Affairs: **ROLLAND VIDA, PhD** • *vida@tmit.bme.hu*

Address: H-1051 Budapest, Bajcsy-Zsilinszky str. 12, HUNGARY, Room: 502
Phone: +36 1 353 1027
E-mail: *info@hte.hu*, Web: *www.hte.hu*